Published in final edited form as:
Analyst. 2008 October ; 133(10): 1308–1346. doi:10.1039/b802918k.

Plasmon-controlled fluorescence: a new paradigm in fluorescence spectroscopy

Joseph R. Lakowicz, **Krishanu Ray**, **Mustafa Chowdhury**, **Henryk Szmacinski**, **Yi Fu**, **Jian Zhang**, and **Kazimierz Nowaczyk**
University of Maryland School of Medicine, Center for Fluorescence Spectroscopy, Department of Biochemistry and Molecular Biology, 725 W. Lombard St., Baltimore, MD 21201, USA

Abstract

Fluorescence spectroscopy is widely used in biological research. Until recently, essentially all fluorescence experiments were performed using optical energy which has radiated to the far-field. By far-field we mean at least several wavelengths from the fluorophore, but propagating far-field radiation is usually detected at larger macroscopic distances from the sample. In recent years there has been a growing interest in the interactions of fluorophores with metallic surfaces or particles. Near-field interactions are those occurring within a wavelength distance of an excited fluorophore. The spectral properties of fluorophores can be dramatically altered by near-field interactions with the electron clouds present in metals. These interactions modify the emission in ways not seen in classical fluorescence experiments. In this review we provide an intuitive description of the complex physics of plasmons and near-field interactions. Additionally, we summarize the recent work on metal–fluorophore interactions and suggest how these effects will result in new classes of experimental procedures, novel probes, bioassays and devices.

Introduction

During the past several years we have studied the effects of metallic particles and surfaces with fluorophores. These studies have revealed a number of valuable effects, such as increases in photostability and fluorescence resonance energy transfer (FRET) near metal particles and directional emission near planar metallic surfaces. We believe these effects will result in a new generation of methods, probes and devices for the use of fluorescence in the biosciences. Because of the importance of these phenomena we have attempted to provide a summary of these effects to stimulate further research on this topic. A second reason for writing this review is the complexity of fluorophore–metal interactions. These effects can be described using classical electrodynamic theory, but theory reformulated for sub-wavelength dimensions and near-field interactions. In classical fluorescence, all emission is detected as radiation propagating to the far-field. In contrast to far-field optics, the near-field effects are the results less known and less intuitive than the far-field effects. Coming from the standpoint of classical fluorescence it can be difficult to understand the terminology and complex physics of surface plasmons and near-field optics. To provide an overview of fluorophore–metal interactions we have summarized the essential features of the theory and experimental results. This article is intended to provide an overview of fluorophore–metal interactions, rather than an exhaustive review, and we apologize to authors for not citing all their publications.

Jablonski diagram for fluorophore–metal interactions

At present, almost all uses of fluorescence depend on the spontaneous emission of photons occurring nearly isotropically in all directions (Fig. 1). Since the emission is mostly isotropic the spectral observables are usually not dependent on the observation direction and collection optics for the measurements. Information about the sample is obtained mostly from changes

in the non-radiative decay rates k_{nr}, such as collisions of fluorophores with quenchers k_q and fluorescence resonance energy transfer k_T (FRET). Changes in k_q or k_T result in changes in intensity and lifetime, both changing in the same direction. The brightness and lifetime of a fluorophore also depends on the radiative decay rate Γ of the fluorophore. However, the rates of spontaneous emission of fluorophores are determined by their extinction coefficients[1] and are not significantly changed in most experiments.

The novel properties of fluorophore–metal interactions can be understood from Fig. 2. Metal colloids can interact strongly with incident light. The optical cross-sections or extinction coefficients of metal colloids can be 10^5 larger than a fluorophore,[2,3] which is illustrated by the incident electric field lines bending into the colloid. While the high optical cross-sections make the metal colloids valuable as scattering probes, the scattered light from both the colloid and the sample occur at the same wavelength as the incident light. Because of their large optical cross-sections, metal colloids can be seen using wide-field optics in samples where the observation volume is defined by the optics and near the diffraction limit.[4–6] These large optical cross-sections make metallic colloids valuable probes for biological imaging and sensing.[6,7] The statements that metal colloids are orders of magnitude brighter than a typical fluorophore is true but their observation requires spatially-limited observation volumes. When the comparison of colloids and fluorophores is made on the basis of optical density, the fluorescence and scattering intensities are approximately equal.[8] Thus, advantages of high optical cross-sections for light scattering by colloids is partially offset by the absence of a wavelength shift as occurs with fluorescence.

The use of fluorophores near metal particles offers the opportunity to utilize the larger effective extinction coefficient of metal particles and the Stokes' shift of fluorescence. When exposed to incident light the electric fields are concentrated around the colloid. These local fields can result in increased excitation of fluorophores near the metals (Fig. 2), which takes advantage of the large extinction coefficients of the colloids. However, there is another potentially more important effect. An excited-state fluorophore can interact with a nearby metal colloid to create plasmons. The fluorophore-induced plasmons can radiate to the far-field and create observable emission.[9] This emission occurs rapidly which is the origin of the decreased lifetimes. The emission retains the same spectrum of the fluorophore, so it is perhaps best to think of the fluorophore–metal complex as the emitting species.

Because the emission spectra remain the same it is often unclear which species is emitting. Since the lifetimes are decreased, and plasmon decay rates are rapid, typically near 50 fs,[10,11] it seems that the metal is emitting. However, the emission spectrum is the same as that of the fluorophore, suggesting that the fluorophore is the emitting species. In our opinion it is best to think of the fluorophore–metal complex as the emitting species. This emission has properties of both the fluorophore and the metal. For this reason we refer to the emitting species as a plasmophore or a fluoron. Both names indicate the combined nature of the emitting species.

While we believe that the emission is due to the plasmophore, the effect of metals can be described from the perspective of the fluorophore. The usefulness of an increase in the radiative decay rate can be understood by considering the definitions of the quantum yield (Q_0) and lifetimes (τ_0). The lifetime and quantum yield of a fluorophore are given by

$$Q_0=\frac{\Gamma}{\Gamma+k_{nr}} \quad (1)$$

$$\tau_0=(\Gamma+k_{nr})^{-1} \tag{2}$$

In classical fluorescence experiments the changes in quantum yields and lifetimes are due to changes in the non-radiative decay rates k_{nr} which result from changes in a fluorophore's environment, quenching or FRET (Fig. 1). The values of Q_0 and τ_0 either both increase or both decrease, but do not change in opposite directions. Unique spectral changes are possible for fluorophores near metal particles or surfaces.[12,13] Suppose this radiative decay rate near the metal is increased and is given by $\Gamma + \Gamma_m$, when Γ_m is the additional rate due to the metal (Fig. 3). The quantum yield Q_m and lifetime τ_m near the metal become:

$$Q_m=\frac{\Gamma+\Gamma_m}{\Gamma+\Gamma_m+k_{nr}} \tag{3}$$

$$\tau_m=(\Gamma+\Gamma_m+k_{nr})^{-1} \tag{4}$$

The physics of fluorophores interacting with metals is a complex topic and it is not possible to present the complete electromagnetic theory. There are several classic reviews which provide summaries of the theory and early experimental results.[14–18] These theories will only consider electromagnetic interactions of the fluorophore. We are not considering chemical or other effects occurring upon direct fluorophore–metal contact. Fortunately, many of the effects of metals on fluorescence are due to through-space interactions. Consider an oscillating dipole near a metallic surface (Fig. 4). The ratio of the decay rates in the absence ($b_0 = 1/\tau_0$) and presence ($b = 1/\tau$) of a metal is given by

$$\frac{b}{b_0}=\frac{\tau}{\tau_0}=1+\frac{3qn_1^2}{2\mu_0 k_1^3}\mathrm{Im}\left(\tilde{E}_R\right) \tag{5}$$

where q is the quantum yield, n_1 is the refractive index surrounding the dipole, k_1 is the wavevector for frequency ω in medium 1 surrounding the fluorophore and $\mathrm{Im}(\tilde{E}_R)$ is the reflective field at the dipole. Eqn (5) can be used to calculate the relative decay rate for dipoles parallel (||) or perpendicular (⊥) to the metal surface. These expressions are

$$\frac{b_\parallel}{b_0}=1+\tfrac{3}{4}q\mathrm{Im}\int_0^\infty\left[\left(1-\mu^2\right)R^{\parallel}+R^{\perp}\right]\times\exp\left[-2l_1k_1d\right]\frac{\mu}{l_1}\mathrm{d}\mu \tag{6}$$

and

$$\frac{b_\perp}{b_0}=1+\frac{3}{2}q\mathrm{Im}\int_0^\infty R^{\parallel}\exp\left[-2l_1k_1d\right]\frac{\mu^3}{l_1}\mathrm{d}\mu \tag{7}$$

where $R^{\|}$ and $R^{\perp}$ are the reflection coefficients of the parallel and perpendicular components of the fields, respectively. The values of l_j are given by $l_j = -i(\varepsilon_j/\varepsilon_l - \mu^2)^{\frac{1}{2}}$ where ε_i and ε_j are the dielectric constants surrounding the fluorophore or the second medium, respectively. For a fluorophore in front of the metal the total decay rate is given by $b = b_{\perp} + 2b_{\|}$ Please see refs [16–18] for a complete definition of these equations. Our purpose in describing these equations is to gain some intuition about enhanced fluorescence or quenching due to metals.

From eqns (5)–(7) it is difficult to understand what factors determine whether the system radiates or is quenched. Some intuitive understanding is gained if we consider the far-field. The integral is real when $\sin\theta < 1$. This real part describes the energy radiating away from the system. When $\sin\theta > 1$ this portion of the integral is imaginary and describes the decaying evanescent field in medium 1, just as a totally internally reflective beam creates an evanescent field in the distal medium. These plasmons are trapped and dissipate rapidly. We believe the radiating and evanescent parts of the fields are related to enhanced fluorescence and quenching, respectively.[19]

The physics literature often uses the term ‘wavevector matching’ to describe when optical energy can and cannot pass across an interface and propagate to the far-field. Wavevector matching is described in more detail below, but the basic concept is continuity of the electric fields across an interface. If the fields are continuous the wavevectors are matched in both media and the light can pass through the interface. If the fields are not continuous the wavevectors are not matched and light cannot pass into the medium with a lower dielectric constant. The beam is reflected but there is an evanescent field in the distal medium. In eqns (6) and (7) wavevector matching is possible when $\sin\theta < 1$, and is not possible when $\sin\theta > 1$.

Classical electrodynamic theory has been used to calculate the radiative decay rates of oscillating dipoles near metallic spheres and ellipsoids.[20–22] Fig. 5 shows the radiative decay rates calculated for a point dipole near a silver ellipsoid. Depending on the distance from the surface and dipole orientation the decay rates can be increased or decreased. Overall, the decay rates are increased and the effect can be dramatic, up to 100 000-fold. Such an increase in the radiative decay rate should result in quantum yields near unity and very short lifetimes [eqns (3) and (4)]. Additionally, the shorter lifetimes can improve photostability because the molecules spend less time in the excited state per excitation cycle. Additionally, the fluorophores will be less prone to optical saturation and can emit more photons per second than an equivalent fluorophore with a longer lifetime. Large increases in the radiative decay rates have been observed experimentally,[23–25] which supports the validity of the theoretical calculations. While we have electrodynamic theory describing fluorophore–metal interactions there are still many questions. For instance, plasmons on metal particles are known to have short decay times near 50 fs.[26,27] The plasmon decay times can be changed by changing the geometry of the particles. However, we do not know if shorter or longer plasmon decay times are preferred for metal-enhanced fluorescence. Shorter plasmon decay times may allow more radiation prior to the loss of energy as heat. Alternatively, a plasmophore may have a longer decay time and the emission enhanced by allowing more time to radiate.

Classes of metal-enhanced fluorescence

While all metal–fluorophore interactions are based on the same physics, the effects can be different based on the geometry of the metal structure. Three possibilities are shown in Fig. 6, which shows a fluorophore interacting with silver particles, a smooth metal surface and a metal surface with a regular pattern. Metal particles can be typically used to increase the fluorescence intensities. This increase occurs by a combination of enhanced fields around the metal and rapid and efficient plasmophore emission. These effects are usually called metal-enhanced fluorescence (MEF, top), and typically result in increased intensities and decreased lifetimes.

The lower left panel shows a fluorophore interacting with a smooth metal film, typically about 40 nm thick silver or gold. In this case the fluorophore creates plasmons which radiate at a defined angle into the substrate. Typically the intensities and lifetimes are not dramatically changed. We refer to this phenomenon as surface plasmon-coupled emission (SPCE). We use the term SPCE because the emission spectrum is the same as the fluorophore but the polarization properties indicate that the plasmon is radiating.

And finally, the lower right panel of Fig. 6 shows a fluorophore above concentric nano-rings. In this case the emission at certain wavelengths is expected to show well-defined beaming into the substrate, while other wavelengths are deflected from the normal. These effects are due to a combination of interactions with a smooth surface (middle) and with the sub-wavelength features (left). We refer to this more general effect as plasmon-controlled fluorescence (PCF). At first one may ask why use three terms to describe the same phenomenon. We find that it is easier to understand the diverse experiments and the goals of the experiments by using the terms MEF, SPCE and PCF.

Simulations of metals and fluorophore–metal interactions

At present we do not have readily available theory and programs to describe fluorophore–metal interactions. These theories and programs will be developed within the framework of methods currently being used to describe the optical and electrodynamic properties of metallic particles and surfaces. At present these calculations are limited to three approaches: Mie theory, the discrete-dipole approximation (DDA) and the finite-difference time-domain (FDTD) method. Mie theory is based on the solution of Maxwell's equations. The DDA and FDTD methods are numerical methods which describe the interactions of light with the particles.

Mie theory and metallic particles

Mie theory does not describe fluorophore–metal interactions but can be used to calculate the optical properties of metal particles. Mie theory provides an analytical solution for the extinction, absorption and scattering properties for spheres of any kind.[28–31] However, Mie theory is limited to spheres, and the extensions to shells for a few other structures are less frequently used.[32,33] If the metal particles are spherical then Mie theory provides an exact solution of their optical properties. The extinction (ext), scattering (sca) and absorption (abs) cross-sections (σ) of metal nanoparticles when excited by electromagnetic radiation can be calculated by series expansions of the involved fields into partial waves of different spherical symmetries. Following the notation of Bohren and Huffman,[31] the optical cross-sections are given by:

$$\sigma_{\text{ext}}=\frac{2\pi}{|k|^2}\sum_{L=1}^{\infty}(2L+1)\text{Re}\{a_L+b_L\} \tag{8}$$

$$\sigma_{\text{ext}}=\frac{2\pi}{|k|^2}\sum_{L=1}^{\infty}(2L+1)\left(|a_L|^2+|b_L|^2\right) \tag{9}$$

$$\sigma_{\text{abs}}=\sigma_{\text{ext}}-\sigma_{\text{sca}} \tag{10}$$

where a_L and b_L are the 'Mie coefficients' following from the appropriate boundary conditions and can be described as:

$$a_L = \frac{m\psi_L(mx)\psi'_L(x) - \psi'_L(mx)\psi_L(x)}{m\psi_L(mx)\eta'_L(x) - \psi'_L(mx)\eta_L(x)} \tag{11}$$

$$b_L = \frac{\psi_L(mx)\psi'_L(x) - m\psi'_L(mx)\psi_L(x)}{\psi_L(mx)\eta'_L(x) - m\psi'_L(mx)\eta_L(x)} \tag{12}$$

with $m = n/n_m$, where n denotes the complex index of refraction of the particle and n_m the real index of refraction of the surrounding medium; $\boldsymbol{k}$ is the wavevector and $x = |\boldsymbol{k}|R$ the size parameter, and $\Psi_L(x)$ and $\eta_L(x)$ are Riccati–Bessel cylindrical functions. The prime indicates differentiation with respect to the argument in parentheses. The summation index L gives the order of the partial wave, where $L = 1$ for a dipole and $L = 2$ for a quadrapole and $L = 3$ for an octapole.

The coefficients a_L and b_L can be used to calculate the optical cross-sections of the particles. The cross-sections for absorption and extinction are given by:

$$C_{sca} = \frac{2\pi}{k^2}\sum_{k^2}^{\infty}(2n+1)\left(|a_n|^2 + |b_n|^2\right) \tag{13}$$

$$C_{ext} = \frac{2\pi}{k^2}\sum_{L=1}^{\infty}(2n+1)\mathrm{Re}\,(|a_n| + |b_n|) \tag{14}$$

The cross-section for absorption (C_{abs}) can be calculated from $C_{ext} = C_{abs} + C_{sca}$.

The expressions for calculation of the cross-sections are rather complex. For this reason we use a commercially available program, MieCalc.[34] Fig. 7 shows calculations of the cross-sections for two silver particles. For the smaller particle at least half of the total extinction is mostly due to absorption. We interpret the absorption as oscillations for which wavevector matching is not possible and the energy is lost as heat. For the larger particle the extinction is mostly due to scatter. In this case, wavevector matching can occur at the metal interface and the energy radiates to the far-field. We believe that the difference between the extinction and scattering of the different size particles is the reason that small metal particles often have no effect or quench fluorescence and larger metal particles can enhance fluorescence.[19]

Discrete-dipole approximation (DDA)

As the metal shapes become more complex it is not practical to solve Maxwell's equations to obtain analytical solutions for the optical properties. Fortunately, it is now possible to study the electrodynamics of complex systems using numerical simulations. One widely used numerical method is the discrete-dipole approximation (DDA). The DDA method is an iterative calculation starting with some initial charge distribution. Then the charge at each point is allowed to interact with all the surrounding charges. The distribution of charges is calculated interactively until the system converges to the final distribution. The DDA algorithm works by replacing the solid particle (target) of interest of volume V by an array of N point dipoles of polarizability α_i located at positions $\mathbf{r}_i$. The lattice spacing d of a target of volume V described by N dipoles is represented as:

$$d=(V/N)^{1/3} \tag{15}$$

Each dipole has an oscillating polarization in response to both the incident wave $\mathbf{E}_{\mathrm{loc},i}$ and the electric field due to all of the other $N-1$ dipoles in the array. The solution to the dipole polarizations can be obtained as the solution to a set of N coupled complex vector equations of the form:[35–37]

$$\mathbf{P}_i=\alpha_i\left(\mathbf{E}_{\mathrm{loc},i}-\sum_{j\neq i}\mathbf{A}_{ij}\mathbf{P}_j\right) \tag{16}$$

where $\mathbf{E}_{\mathrm{loc},i}$ is the electric field at position $\mathbf{r}_i$ due to the incident plane-wave with amplitude $\mathbf{E}_0$ and wavevector $\mathbf{k}$ and is represented as:

$$\mathbf{E}_{\mathrm{loc},i}=E_0\exp[\,i(\mathbf{k}\cdot\mathbf{r}_i-\omega t)] \tag{17}$$

and the polarizability α is related to the dielectric constant of the target (ε_i) and that of the embedding medium (ε_0) through a factor $\varepsilon_r = (\varepsilon_i/\varepsilon_0)$ according to the following expression:[37]

$$\alpha=\left(\frac{3d^3}{4\pi}\right)\left(\frac{\varepsilon_r-1}{\varepsilon_r+2}\right) \tag{18}$$

In eqn (16), the term $-\mathbf{A}_{ij}\,\mathbf{P}_j$ represents the contribution to the electric field at position $\mathbf{r}_i$ that is due to the dipole $\mathbf{P}_j$ at location $\mathbf{r}_j$. Each element $\mathbf{A}_{ij}$ is a 3 × 3 matrix defined by:

$$\mathbf{A}_{ij}\mathbf{P}_j=\frac{\exp\left(ikr_{ij}\right)}{r_{ij}^3}\left\{\begin{array}{l} k^2\mathbf{r}_{ij}\times\left(\mathbf{r}_{ij}\times\mathbf{P}_j\right)+\frac{\left(1-ikr_{ij}\right)}{r_{ij}^2} \\ \left[r_{ij}^2\mathbf{P}_j-3\mathbf{r}_{ij}\left(\mathbf{r}_{ij}\cdot\mathbf{P}_j\right)\right] \end{array}\right\} \tag{19}$$

where $\mathbf{r}_{ij} = \mathbf{r}_i - \mathbf{r}_j$ and $k = \|\mathbf{k}\|$. Defining $\mathbf{A}_{ij}=\alpha_i^{-1}$ helps to reduce the extinction problem to finding the polarizations $\mathbf{P}_j$ that satisfy a system of N inhomogeneous linear complex vector equations:

$$\sum_{j=1}^{N}\mathbf{A}_{ij}\mathbf{P}_j=\mathbf{E}_{\mathrm{loc},i} \tag{20}$$

Once the above equation is solved for the unknown polarizations $\mathbf{P}_j$, the extinction C_{ext}, absorption C_{abs}, and scattering cross-sections C_{sca} are evaluated from the optical theorem to give:

$$C_{\mathrm{ext}}=\frac{4\pi k}{|\mathbf{E}_0|^2}\sum_{i=1}^{N}\mathrm{Im}\left(\mathbf{E}_{\mathrm{loc},i}^{*}\cdot\mathbf{P}_i\right) \tag{21}$$

$$C_{\text{abs}} = \frac{4\pi k}{|\mathbf{E}_0|^2} \sum_{i=1}^{N} \left\{ \text{Im}\left[\mathbf{P}_i \cdot \left(\alpha_i^{-1} \right)^* \mathbf{P}_i^* \right] - \frac{2}{3} k^3 |\mathbf{P}_i|^2 \right\} \quad (22)$$

The scattering cross-section $C_{\text{sca}} = C_{\text{ext}} - C_{\text{abs}}$ can be directly evaluated once the polarizations $\mathbf{P}_i$ are computed. Examples of DDA calculations are shown in Fig. 8. These calculations are for a sphere or an ellipse which have the same cross-sectional areas. In the sphere the extinction is due mostly to scattering, which is reasonable for a 100 nm diameter metal particle. In the ellipsoid the extinction coefficient shifts to nearly 700 nm. As for Mie theory, the DDA calculations provide the values of the cross-sections, here listed as Q_{E}, Q_{A}, and Q_{S}. The absorption component is dominant for the spherical colloid, and the scattering component is larger and at longer wavelengths for the elongated particle. This suggests to us that the elongated particle should be more effective for MEF. This result agrees with our data showing that larger particles, non-spherical or aggregated particles are more effective in MEF.[38] Similarly, aggregates of particles or non-spherical particles are known to be more effective for SERS.[39,40]

In Fig. 7 and Fig. 8 we showed the use of Mie theory or the DDA method to calculate the cross-section of metal particles. The cross-sections are far-field optical properties of the particles. However, fluorophores undergo near-field interactions with the particles. The near-fields can be created by the incident light or induced by an excited fluorophore. Mie theory can also be used to calculate the near-fields around metal particles induced by far-field illumination.[41–43] The expressions to calculate the near-fields appear to be more complex and less widely used than eqns (8)–(14), which are used to calculate the far-field optical cross-sections. Fig. 9 shows such calculations for a silver colloid with a radius of 100 nm. The values of Q can be thought of as the efficiency with which the incident field is converted to the various fields. The near-fields can be larger because these have distance (r) dependence of r^{-3}, while the far-fields decay as r^{-1}. The optical cross-sections in Fig. 9 show the complexity of fluorophore–metal interactions. Which of these fields should we consider for fluorophore–metal interactions? It seems likely that metal-enhanced excitation is dependent on the near-fields and the far-field emission will depend on some combination of the scattering and absorption cross-sections.

The near-fields induced around colloids by far-field illumination can also be calculated using the DDA method. Fig. 10 shows DDA calculations for colloids with far-field plane-wave illumination.[35] For the smaller 60 nm colloid (left) the electric field is concentrated near the top and bottom of the colloid. This result is to be expected because the light wavelength is larger than the colloid and the system is in the electrostatic limit. For the small colloid one can imagine it acting as a small radiating dipole, analogous to a fluorophore, with the light being scattered uniformly around the vertical z-axis. For the larger 120 nm colloid the field is not uniform along the z-axis, but is strongest towards the incident light. In some sense this result is consistent with Mie theory which predicts a non-symmetrical distribution of scattered light by larger particles. However, Mie theory predicts the light to be scattered more strongly in the forward direction, away from the incident source. This difference between the location of the near- and far-field energy reveals one of the complexities of near-field effects. It is difficult to understand the linkage between the near-fields around a particle and the far-field spatial distribution of the energy. This linkage may be clarified as a result of the growing interest in near-field optics and nanophotonics.[44–50]

Finite-difference time-domain (FDTD) method

An alternative to Mie theory or the DDA method is the finite-difference time-domain (FDTD) method. The FDTD method can provide the near-field and far-field properties for objects of

any size or shape, and can even provide the time-response of the system. In our opinion the finite-difference time-domain (TDTD) method is well suited for calculations on metallic nanostructures. The FDTD method is basically a numerical solution of Maxwell's equations.[51,52] For the case of plane-wave illumination the program calculates the progression of the electric field moving towards and interacting with the particle. To provide the system response the program uses time steps which are short compared to the light frequency and a grid size which is small compared to the wavelength. The FDTD method is not an approximation but provides an exact solution of Maxwell's equations limited only by the time step intervals and grid size used in the calculations. For visible light these parameters are typically 0.005 fs and 4 nm.

There are several advantages in using FDTD for the simulation of optical properties of plasmonic nanostructures in biomedical applications. They are:

1. FDTD avoids the difficulties associated with large matrix manipulation and inversion and can be adapted easily for larger structures.
2. Since FDTD is a time-domain technique, it directly calculates the impulse response of an electromagnetic system. Hence a single FDTD simulation can provide the temporal response, steady-state equilibrium response, frequency response, as well as any non-linear response of a system.
3. With FDTD, generating structures of various sizes is reduced to a problem of mesh generation, thus overcoming the complex problems of reformulating integral equations for different structures such as Green's functions.
4. Both far-field and near-field simulations can be performed in the chosen grid area for the target providing that appropriate boundary conditions are established for the far-field.
5. FDTD can handle dispersive materials including noble metals which are critical for plasmonic applications.
6. The basic algorithm of the computational domain can be broken down into smaller sub-spaces to allow for parallel computations.
7. FDTD can support finite or infinitely-periodic structures. This makes it important for the simulation of plasmonic structures made up of metal nano-hole arrays and gratings.
8. FDTD can handle input of pulsed, CW or impulse waveforms.
9. FDTD can be used to calculate the field, intensity or Pointing vectors at or near targets arranged in arbitrary spatial arrangements.
10. FDTD can handle point-source, plane-wave or mode-profile wavefronts.
11. The FDTD method is well suited for computation of objects with sub-wavelength features.

FDTD, however, has several disadvantages. Among them are that the simulations are only as accurate as the grid-spacing. High frequency responses require many time steps which again increase the need for computing power. A final disadvantage is that at every time step, the entire grid must be updated and this requires a good deal of computing power. The combined effect of these factors is that for many 3-D structures of interest in plasmonics/nanophotonics applications, a complete 3-D simulation of high accuracy and precision is computationally intensive. Fortunately, there are several commercially available software packages for these calculations.[53–56]

The flexibility of the FDTD method can be used to illustrate the complexity of fluorophore–metal interactions. Fig. 11 (top) shows our FDTD calculations of the electric field distribution induced by 580 nm plane-wave illumination of an 80 nm diameter silver colloid.[57] The induced fields are mostly along the *z*-axis, similar to that shown in Fig. 10 using the DDA method. A dramatically different result is obtained for the fields induced by a dipole in the near-field. When a 620 nm point dipole is positioned near the colloid there is a complex field pattern (bottom). The different fields induced from the far-field and the near-field illustrate the complexities of metal–fluorophore interactions.

Metallic particles can also affect the spatial distribution of far-field radiation. This effect can be seen from our FDTD calculations of the distribution of light scattered from silver colloids or radiated from a fluorophore near silver colloids (Fig. 12). The left panel shows the *x–y* plane distribution of light when silver colloids are exposed to plane-wave illumination at 420 nm.[57] For the small 20 and 80 nm colloids the scattered light is distributed equally in the *x–y* plane, which is consistent with fields calculated above (Fig. 10) for the smaller colloid. For the larger 320 nm colloid the light is scattered mostly in the forward direction, which is consistent with the results of Mie theory.

Dramatically different results are found when the colloid is placed near a point dipole (Fig. 12, right). The point dipole alone, when oriented along the *z*-axis, radiates equally in all directions in the *x–y* plane. A similar result is found for the fluorophore near a 20 nm diameter colloid. However, if the fluorophore is near the 80 nm colloid the energy is radiated predominantly in the back-direction to the dipole, which is opposite to Mie theory. This effect does not appear to be a simple reflection because the 80 nm colloid is smaller than the free-space wavelength. Additionally, a complex spatial distribution, different from the Mie theory result, was seen for the fluorophore near a 320 nm silver colloid. The results shown in Fig. 11 and Fig. 12 show that there are a number of complex interactions between fluorophores and metals that will affect the observed spectral parameters.

Experimental studies of fluorophore–metal interactions

Prior to 2000 there were a limited number of publications on the effects of metals on fluorescence, designed mostly from the standpoint of optical physics.[58–63] Since that time there has been rapid growth in the number of such publications. In the following paragraphs we describe primarily experimental results from this laboratory which were designed to determine the usefulness of fluorophore–metal interactions in the biological applications of fluorescence. We acknowledge the large number of interesting results from other laboratories on this topic.

Metal-enhanced fluorescence with silver, gold and aluminium

The general usefulness of MEF sensing can be expanded if MEF occurs with metals other than silver. Gold is an attractive MEF substrate because of the high chemical stability of gold and its well-developed and facile surface chemistry. However, it is widely recognized that gold is an effective quencher of fluorescence,[64–69] so MEF with gold particles may not be expected. Nonetheless, we have shown that gold particles can cause substantial MEF with longer wavelength fluorophores.[70] Slides coated with gold particles were prepared by vapor deposition. The absorption spectra showed that there were gold particles on the surface, and not a continuous gold film (not shown). Fig. 13 shows over sixfold increased intensities for Alexa Fluor 555® -labeled IgG. We believe that we observed MEF rather than quenching for two reasons. The gold particles on the surface were probably larger than used in the reports on quenching,[64–69] so that our particles have more scattering than absorption in the optical extinction. Additionally, we separated the labeled IgG from the gold surfaces by a 5 nm coating of silica. It appears that quenching by gold may occur at shorter distances and enhancement at

larger distances above several nm. It is important to note that 5 nm silica is similar to the thickness of a monolayer of albumin or IgG, and that gold MEF occurs at distances that are useful in surface-bound assays.

Aluminium is also thought to quench fluorescence, but there are few reports on this effect.[71] Aluminium surfaces are highly reactive and bare aluminium surfaces are quickly coated with an oxide. However, this process is self-limiting and does not continue after the oxide coating is formed. We tested aluminium particles to see if they could provide MEF. Slides were coated with aluminium by vapor deposition. The particle size depended on the amount of aluminium on these surfaces. When the average thickness of Al was 2 nm the particles were about 100 nm in size. For 10 nm of Al the particles were about 800 nm, and the Al surface started to become continuous for an average thickness of 80 nm (Fig. 14). An important optical property of Al is that it does not have an intrinsic absorption until about 280 nm, which suggested to us that it may provide MEF for UV fluorophores. We found substantial MEF using aluminium[72] for 2-aminopurine (2-AP) and 7-hydroxycoumarin (7-HC) (Fig. 15). These results with aluminium, and the previous results with gold, show that MEF can be used with a wide range of fluorophores from the UV to the NIR regions of the spectrum.

MEF occurs with quantum dots, phycobiliproteins and lanthanidesz

Organic fluorophores are the mainstay of fluorescence sensing and imaging. However, MEF will become more useful if it occurs with fluorophores other than small organic molecules. Among these alternative probes the lanthanides are useful because their long lifetimes allow off-gating of the interfering autofluorescence. We have observed increased intensities and decreased lifetimes for lanthanides near silver particles (not shown).[73,74] Quantum dots (Qdots) and phycobiliproteins (PBPs) are of interest because they can be 10–100-fold brighter than organic fluorophores. Remarkably, they can be made still brighter by proximity to silver particles. Fig. 16 shows the emission spectra of CdTe Qdots on glass and silver island films (SIFs), showing an approximate five-fold increase in intensity and a decrease in lifetime.[75] These spectral changes suggest an increase in the radiative rate of the Qdots, which has been observed in other laboratories.[76,77] MEF has also been observed for phycobiliproteins.[78] Fig. 17 (top) shows emission spectra of phycoerythrin (PE) on glass and silver particles (middle). The increase in PE brightness is apparent from the real-color photographs on glass and silver particles. As is typical for MEF the lifetimes are decreased. These results show that MEF occurs with all types of fluorophores, making MEF applicable to many types of assays. The fact that MEF occurs with all types of fluorophores is because MEF is due to a through-space interaction between the excited-state dipole moment of the fluorophore and the metal surface. This is similar to FRET which is also due to a through-space near-field interaction, and FRET also occurs with all types of fluorophores.

Biomolecule association measured using proximity to metal particles

Since the early days of biochemical fluorescence there has been continued use of fluorophores which display spectral changes in response to a change in the local environment. Perhaps the most well-known probe of this type is 1-anilino-8-naphthalenesulfonic acid (ANS) and its derivatives.[79–81] These probes are weakly fluorescent in water but become highly fluorescent when bound to proteins or membranes. Similar probes exist for DNA, such as ethidium bromide, its dimers, and probes of the TOTO-YOYO series. These probes are weakly- or non-fluorescent in water and become highly fluorescent when bound to double helical DNA.[81–84] In many applications it is desirable to have the brightest possible probes which are covalently linked to the molecule of interest. Typical probes of this type are the rhodamines, cyanines and Alexa probes. While these probes are bright they usually do not display significant changes in intensity in response to changes in their local environment. For instance, an Alexa-labeled protein may not change intensity upon binding to another protein, or a Cy5-labeled single strain

of DNA may not change intensity upon hybridization with its complementary strand. Hence such probes are useful for tracking the biomolecules, but are less useful for studies of functions.

Metal-enhanced fluorescence provides an opportunity to obtain changes in intensity upon a binding interaction for almost any fluorophore. The basic idea is to couple the binding reaction to proximity to a metal particle. One example is binding of a fluorescein-labeled DNA oligomer binding to a complementary strand.[85] This strand is bound to silver particles *via* an SH group (Fig. 18). When the fluorescein-labeled DNA binds near the metal its intensity is increased, not by hybridization, but by proximity to the silver particles. As described above, all types of fluorophores display MEF. Hence, MEF-based binding assays can be used to measure a large range of surface-bound assays.

Single molecule detection (SMD)

Single molecule detection (SMD) is a powerful tool to study the properties of individual fluorophores and the dynamics of biomolecules. SMD is valuable because the measurements bypass the ensemble averaging that occurs in traditional fluorescence measurements. Single molecule detection becomes even more valuable for studies of fluorophore–metal interactions. In contrast to homogeneous solutions the samples used for PCF are inherently heterogeneous. This heterogeneity arises from a variety of sources. For planar metallic structures the fluorophores can be at various distances and orientations relative to the surface. Distance and orientation also play a role when fluorophores are near particles. For silver island films there is a range of particles sizes and shapes, and the fluorophore may be localized on the metal or on the glass. Metal colloids in suspension can have a distribution of sizes, which can also contribute to sample heterogeneity. All of these effects are hidden in ensemble measurements when the observed spectral parameters represent a weighted average of all the fluorophores in the sample. When using SMD each observed molecule represents one of the possible environments. The distribution of environments can be determined by observing a number of individual molecules. It is not trivial to synthesize metal–fluorophore structures with precisely defined spatial parameters, and a large number of such structures would need to be synthesized to identify the preferred structure for brightness, photostability, or other desired properties. Single molecule experiments can show what is possible in the best structures by finding several of these fluorophores among the observed population.

In order to observe single fluorophores the incident intensities must be high to obtain high rates of excitation and emission. As a result, single fluorophores can be observed for only a short period of time, typically seconds, prior to photobleaching. Additionally, observation of single fluorophores is usually accomplished using diffraction-limited volumes. Otherwise the single molecule emission is overwhelmed from background due to autofluorescence or Raman scatter.[86] MEF can thus be useful in SMD by increasing the photo-stability and brightness of fluorophores. These effects are shown in Fig. 19 and Fig. 20.[87,88]

Fig. 19 shows images of single Cy5-labeled DNA molecules on a glass surface or on a SIF. When examined under the same conditions the Cy5-DNA molecules cannot be seen on glass but are easily observed on the SIF. We examined a large number of Cy5-DNA molecules on both surfaces (Fig. 20). The representative time traces show the higher intensity and increased photostability of Cy5-DNA near the silver particles. In this sample the Cy5-DNA molecules were bound uniformly over the glass and silver regions of the sample, so that there is a range of environments. The intensity histograms show a large shift to higher intensities on the SIF as opposed to glass. In ensemble measurements we typically observed ten-fold enhancements on SIFs. The SMD experiments show that this increase is probably due to a fraction of the molecules which display enhancements of over 100-fold. In fact over 35% of the molecules displayed this large enhancement. This result suggests that it will be possible to synthesize fluorophore–metal complexes in which all the fluorophores are enhanced more than 100-fold.

The fact that a large fraction of the molecules is enhanced over 100-fold also suggest that the geometric features do not need to be precise to obtain structures which display large enhancements.

For some types of experiments silver colloids are superior to silver island films. Suspension of silver colloids can be made with well-defined sizes and low heterogeneity. This allows experiments which show the effects of particle size upon fluorescence. One such experiment is shown in Fig. 21. The Cy5-DNA molecules were bound to silver colloids *via* a sulfhydryl group. The single molecule traces show that the intensity and photostability are strongly dependent on colloid size. Such data can be interpreted with analytical solutions of Maxwell's equations for such symmetrical systems.[19,21] However, it is useful to have an intuitive explanation of the effects. It seems logical that the 5 nm particle has no effect because smaller colloids may not display plasmons and/or the plasmon resonance wavelength is much shorter than the spectra of Cy5 (Fig. 22). As the particle size increases the resonance shifts to longer wavelengths. However, it seems that the overlap is stronger with the 100 nm particle, not the 50 or 70 nm particle size, which results in the brightest Cy5 emission. This lack of correspondence is probably due to the differences in the near- and far-fields. The extinction spectra reflect the interaction of far-field light with the particle. The Cy5 intensities reflect the near-field interactions of the fluorophore with particles. These interactions may be optimal with the smaller particles because of the larger wavevector (shorter effective wavelengths) in the near-field of the fluorophore.

Another approach to obtaining locally high fields is to use clusters of particles. It is well known that the local fields induced by incident light can become very large for closely spaced particles, in some cases up to a factor of 10[13.90,91] Hence it is of interest to determine the effects of localizing a fluorophore between two colloids.[92] This was accomplished using Cy5-labeled DNA (Fig. 23). We found that the intensity for Cy5 between two silver particles was increased above the intensity when bound to a single silver particle (Fig. 24). This result suggests that biomolecule binding assays can be based upon clustering of metal particles near fluorophores.

Single molecule FRET

Another opportunity using metal–fluorophore interactions is to increase the distances for energy transfer. The distances for FRET are rarely more than 6 nm, which is smaller than the dimensions of an IgG antibody. Since immunoassays are often performed in a sandwich format (Fig. 25) the distances between donors and acceptors are too large for useful amounts of FRET. As a result, FRET is infrequently used for sandwich immunoassays.[93] We have observed nearly two-fold increases in the Förster distance (R_0), in both ensemble measurements and in single molecule measurements.[94,95] The single molecule experiments were performed using spherical particles, but much larger increases in FRET are expected for elongated particles.[96–98] The importance of a larger effective R_0 for immunoassays can be seen from a specific example. Suppose the assay is a sandwich assay with two IgG molecules and a relatively small antigen like the cardiac marker myoglobin with a molecular weight of 25 000.[99–101] If the donor D and acceptor A are located near the center of the IgG molecules they will be about 12 nm apart (Fig. 25). Typical Förster distances R_0 are rarely larger than 6 nm. As a result the transfer efficiency will be about 0.015, which is essentially undetectable. Now suppose a metal particle increases the Förster distance by two-fold to 12 nm. Now the transfer efficiency increases to 50% and is readily detectable. These considerations show that metal-enhanced FRET can be used to develop FRET immunoassays of large molecular weight antigens.

Single molecule FRET experiments can be used to determine the transfer efficiency of donor–acceptor pairs and the amount of FRET near metal particles.[95,98–102] We prepared a donor- and acceptor-labeled oligomer which contained a central amino group for binding to the colloid. The length of the oligomers was chosen so that there was less than 10% transfer in the absence

of the particle (Fig. 26). The transfer efficiency increased dramatically upon binding to the 15 nm colloid, and increased more with increasing particle size. The increase in transfer efficiency is consistent with a 1.7-fold increase in the Förster distance. Assuming the R_0 value in the absence of metal is 60 Å, the effective R_0 on the 80 nm particle is 102 Å, which is possibly one of the highest R_0 values that has been observed. In future studies these effects will be analyzed using the available analytical theory[96–98] or by numerical FDTD simulations.

To date we have only examined the effects of spherical particles on FRET. The theory predicts much higher rates of energy transfer when the donor–acceptor pairs are close to elongated particles.[96–98] Such long-range energy transfer may find uses in cell biology. It is known that cellular function can be affected by protein association in the external cell membrane, such as the receptors of the epidermal growth factor (EGF). Suppose the EGF receptors are labeled with donors and acceptors, by using either labeled EGF or labeled antibodies to the receptor. Upon receptor association there will be minimal FRET because of the large size of the proteins. Now suppose one of the labeled proteins is bound to an ellipsoidal silver colloid about 100 nm long. Then it is possible that the colloid will facilitate FRET over this distance and detect receptor association. It may not be possible to measure the exact donor-to-acceptor distance using metal particles, but it may be possible to detect proximity over distances ranging from 10 to 100 nm. At present it is difficult to measure distances in this range. Electron microscopy requires fixed samples and the resolution of optical microscopy is limited to about 300 nm. Enhanced FRET by metal particles may allow measurement over this range of distances.

While we have experimentally shown increases in FRET near metal particles the detailed mechanisms are not yet understood. For example, the transfer efficiency E is known to depend on the rate of energy transfer.

$$E=\frac{k_{\mathrm{T}}}{\tau_0^{-1}+k_{\mathrm{T}}} \tag{23}$$

At first glance an increase in the transfer rate may be expected to increase the transfer efficiency. However, if the decay rate of the donor τ_0^{-1} increases by the same amount then the transfer efficiency will remain the same. In fact, the equations to calculate the transfer rate in the absence of metals contain the ratio of the quantum yield of the donor Q_{D} to the donor lifetime τ_{D}. This ratio is equal to this radiative decay rate of the donor. Hence for classical Förster transfer the transfer rates are always proportional to the radiative decay rate of the donor. This is the reason the FRET efficiencies and Förster distances are the same for organic fluorophores, metal–ligand complexes and the lanthanides, which have decay times of nano-, micro- and milli-seconds, respectively. Our studies of metal–ligand complexes and lanthanides near metals supports the notion that the increases in the rates of radiative decay are proportional to the spontaneous decay rates. From this perspective the FRET efficiencies are not expected to change near metal particles, but we do not know if the radiative rates and transfer rates are always increased by the same relative amounts. Additional experimentation and theory are needed to clarify this apparent conflict.

Plasmon-coupled fluorescent probes (PCFP)

Plasmon-controlled fluorescence provides an opportunity to create ultra-bright probes based on complexes of metal particles with fluorophores. The basic idea is to create metal–fluorophore complexes in which the metal particle increases the brightness of the bound fluorophores. This can be accomplished by trapping the fluorophores in metal shells or by coating metal particles with fluorophores. Theory has predicted that fluorophores in metal

shells can be 100-fold brighter than the isolated fluorophore, even after consideration of the transfer efficiency of incident light into the shell and radiation out of the shell.[103,104] We have found increased intensities for fluorophores in metal shells and for metal colloids coated with fluorophores.[105] Such probes may have the advantage over quantum dots because of the low toxicity of silver particles, even if the silver surface is completely exposed. In contrast, quantum dots require a surface coating to avoid exposure of the toxic metal cadmium. One example of a PCFP is shown in Fig. 27. In this case we trapped $Ru(bpy)_3^{2+}$ in silica nanoparticles.[105] These particles were then coated with silver shells of increasing thickness. The silver-coated particles display increasing intensity with increasing shell thickness. Additionally, the emission spectra became narrower, as predicted by theory. Our results agree with theoretical predictions that a single fluorophore in a metal shell can be 100-fold brighter and the emission spectra of the particle will become narrower.[103,104]

We have also observed increased brightness when silver colloids are coated with fluorophores.[106,107] In this case the fluorophores were bound to the silver particles by a surface coating of silica. Increased intensities were observed for both a europium chelate and rhodamine 800 (Fig. 28). The development of plasmon-coupled fluorescent probes is in its infancy, and the present stage of development is comparable to the first observations of emission from colloidal semiconductor particles, when the particles displayed low quantum yields and a large diversity of sizes. At first these particles did not appear to be promising probes. However, these particles evolved into quantum dots which now have narrow emission spectra, high quantum yields and low toxicity.[108–110] We anticipate similar advances in the development of plasmon-coupled fluorescent probes.

Surface plasmon-coupled emission (SPCE)

In the previous sections we discussed the effects of metallic particles on fluorophores. We now consider the interactions of fluorophores with continuous metal films. The underlying electrodynamics mechanisms must be the same for the interactions of fluorophores with metal particles or surfaces. However, the effects on fluorescence are very different. These differences arise from the defined geometry of a metal film and from the different nature of surface plasmons on sub-wavelength size particles and on planar surfaces. Before describing the complex physics of surface plasmons it is informative to describe the final result. Suppose an excited fluorophore is located above a thin metal film. The substrates used for SPCE are typically 40 nm-thick silver or gold films on a glass substrate (Fig. 29). A typical configuration for an SPCE experiment is shown in Fig. 30. The fluorophores are excited from the air side of the sample and the emission is observed on the distal glass side of the substrate. The result is rather remarkable. For typical three-dimensional samples, not on a metal film, the emission is mostly the same in all directions. In contrast, the fluorophores above the metal film yield a cone of emission into the substrate (Fig. 31). This means that almost all the emission into the substrate occurs at a defined angle θ_F relative to the normal axis. This result is even more remarkable when considering the optical properties of the metal films (Fig. 32). These films are highly reflective and are visually almost opaque. SPCE is also observed with gold (Fig. 31) which is surprising because gold is known to strongly quench fluorescence. We now know the origin of the angular emission. Excited fluorophores in the near-field create plasmons in the metal film, and these plasmons in turn radiate into the substrate.[111,112] Analytical theories have now been published for SPCE.[113,114] However, an intuitive understanding of SPCE can be obtained from the principles of surface plasmon resonance (SPR).

Principles of surface plasmon resonance (SPR)

Surface plasmon resonance is widely used to study bioaffinity reactions on surfaces.[115–120] In SPR a thin metal film is illuminated through a prism, which is called the Kretschman (KR) configuration (Fig. 33). The films are highly reflective except at a specific angle called

the surface plasmon angle θ_{SP} (Fig. 34). At this angle of incidence θ_I the film adsorbs essentially all the incident light. This absorption is due to the creation of surface plasmons on the air side of the metal film. Because the plasmons are on the air or sample side of the metal they are affected by the refractive index above the film, which is the basis of SPR instruments. Binding of biomolecules to the metal surface causes a small change in the refractive index, which in turn causes a change in the surface plasmon resonance angle.

Surface plasmon resonance can be understood from the unique optical properties of the metals and by the need for the continuity of electric fields across an interface. If an electrical field E_0 is incident on a dielectric material the field within the material is $E = \varepsilon E_0$ where ε is the dielectric constant. In a dielectric all the electrons are bound to the nuclei and are not freely mobile. In a metal some of the electrons are free and can respond to an incident field. At low frequencies the metal is a conductor and the dielectric constant is large and negative. At higher frequencies in the visible region the electrons cannot completely follow the incident field and ε becomes dependent on wavelength (Fig. 35). While the electrons in a metal are highly mobile, they are not infinitely fast.[2,121–124] The electrons respond to the incident field but cannot keep up completely at the higher frequencies. As a result the optical and reflective properties of silver and gold depend on the interplay of incident frequency, electron mobility, and bound electrons, as well as underlying absorption bands not related to electron oscillations. This interplay of electron mobility and incident frequency results in complex and imaginary optical constants.

The refractive index and dielectric constants of a metal (m) are given by

$$n_m = n_r + i n_{im} = \sqrt{\varepsilon_{im}} \tag{24}$$

$$\varepsilon_m = \varepsilon_r + i\varepsilon_{im} \tag{25}$$

where $i = \sqrt{-1}$, and subscripts indicate the real (r) and imaginary (im) components. Both of these constants are wavelength (frequency) dependent. Some intuition about the physical meaning of these terms can be obtained from examining specific examples for gold and silver (Fig. 35). The real part of the dielectric constant becomes negative at longer wavelengths due to the conductive properties of the metal. As the incident frequency decreases, ε_r becomes more negative, which indicates the mobile electrons are closely following the incident field with a 180° phase shift. The optical constants for metals reveal the relaxation properties of the electron oscillations. Because relaxation is rapid, direct measurements have only recently become possible. These experiments are showing that the plasmon relaxation rates depend on the size and shape of the metal structure.[26,125–127] The imaginary part of the dielectric constant represents the absorption of light by the metal.

Wavevector matching in surface plasmon resonance

In optics the concept of continuity of an electric field across an interface is called wavevector matching. The wavevector describes the rate at which the electric field of a propagating wave changes with distance. Shorter wavelengths have more rapidly changing electric fields and thus larger wavevectors. An electromagnetic wave propagating in space can be described by

$$\overline{E}(\overline{r},t) = \overline{E}\exp(i\omega t - i\overline{k}\cdot\overline{r}) \tag{26}$$

where the bars indicate vector quantities, $\bar{r}$ is a unit vector in the direction of propagation, ω is the frequency in rad s^{-1}, $i = \sqrt{-1}$, and $\cdot$ indicates the dot product. The term k is the wavevector and is given by

$$k = \frac{2\pi}{\lambda} = \frac{n\omega}{c} = nk_0 \tag{27}$$

where $\lambda = \lambda_0/n$ is the wavelength, λ_0 is the wavelength in a vacuum, n is the refractive index of the medium and k_0 is the propagation constant of the wave in a vacuum. It is understood that the physical values are given by the real part of eqn (25). Hence the electric field is described by

$$\overline{E}(\bar{r},t) = \overline{E}_0 \exp(\cos\omega t - \bar{k} \cdot \bar{r}) \tag{28}$$

For SPR we need to consider the electric field along the x-axis, the metal–water interface. This component is given by

$$E(x,t) = E_{0x} \exp(\cos\omega t - k_x x) \tag{29}$$

To satisfy Maxwell's equations the electric fields have to be continuous across the interface, which requires k_x to be equal at the surface in both media.

The phenomenon of SPR can be understood by considering the propagation constant of the electromagnetic wave in the metal along the x-axis. In the metal film the field is described by eqn (28) and eqn (29) with $k_x = k_r + ik_{im}$ being the complex wavevector along the x-axis. For a metal the wavevector for the surface plasmon is given by

$$k_{SP} = \frac{\omega}{c}\left(\frac{\varepsilon_m \varepsilon_s}{\varepsilon_m + \varepsilon_s}\right)^{1/2} = k_0\left(\frac{\varepsilon_m \varepsilon_s}{\varepsilon_m + \varepsilon_s}\right)^{1/2} \tag{30}$$

where ε_m and ε_s are the dielectric constant of the metal (m) and sample (s), respectively. The parameter ε_s refers to the effective dielectric constant in the region of the evanescent field. Because the real part of ε_m is larger than the imaginary part the propagation constant can be approximated by

$$k_{sp} = k_0\left(\frac{\varepsilon_r \varepsilon_s}{\varepsilon_r + \varepsilon_s}\right)^{1/2} \tag{31}$$

The incident light can excite a surface plasmon when its x-axis component equals the propagation constant for the surface plasmon (Fig. 36). The propagation constant for the incident light in the prism (p) is given by

$$k_p = k_0 n_p \tag{32}$$

and the component along the *x*-axis is equal to

$$k_x = k_0 n_p \sin\theta_p \tag{33}$$

where θ_p is the incidence angle θ_I in the prism. Hence the conditions for SPR absorption are satisfied when

$$k_{SP} = k_x = k_0 n_p \sin\theta_{SP} \tag{34}$$

where θ_{SP} is the angle of incidence in the metal for surface plasmon resonance to occur. These considerations show that surface plasmon resonance occurs whenever the *x*-axis component of the incident wavevector equals that obtained from eqn (31).

Detailed consideration of eqn (31) yields some interesting insights. Suppose light is incident on the metal from a vacuum or air (n = 1.0). The maximum value of k_x is given when the incident light is parallel to the interface, yielding $k_x = k_0$. Examination of Fig. 35 shows that the real parts of ε_m are negative and much greater than unity. These real parts dominate the ratio in eqn (29) so that k_{SP} is always larger than the free-space wavevector k_0. For this reason, surface plasmons cannot be excited with light incident from the air or a medium with a lower dielectric constant. In order to obtain SPR the magnitude of k_x must be increased to equal or exceed k_{SP}. This can be accomplished using the configuration shown in Fig. 33. This approach uses a prism to increase the wavevector to $k_p = n_p k_0$. The *x*-component is then matched by 'attenuation' of the *x*-component by a factor $\sin\theta_I$ by changing the incident angle to θ_{SP} (Fig. 36). When measuring or discussing SPR one can assume that the incident beam is p-polarized. Only p-polarized incident light gives the reflectivity curves seen in Fig. 34. P-polarization is when the electric field of the incident light is perpendicular to the surface and s-polarization is when the electric field is parallel to the surface. An s-polarized beam will not excite surface plasmons and will not show decreased reflectivity at some angle of incidence.

SPR compared with surface plasmon-coupled emission

The background information on SPR provided above facilitates a description of SPCE. If an incident beam couples with the surface plasmons to create an evanescent field, it seems reasonable to expect that an excited fluorophore at near-field distances will couple with plasmons that radiate into the substrate (Fig. 29). Suppose the sample is excited from the side opposite the prism, which is the reverse Kretschmann (RK) configuration (Fig. 30). An excited fluorophore near the metal film would not know how it was excited, that is, the emission should be the same whether the fluorophore is excited by an evanescent SPR field or from a light source not coupled to the surface plasmons. Excited fluorophores, which are close to the metal surface (less than 100 nm), are expected to couple with the metal film resulting in radiation into the substrate. The occurrence of SPCE is not obvious because the SPCE plasmons must be created from the sample side of the metal, and plasmons cannot be created by light incident on this side of the metal. In fact, free-space emission from fluorophores which impinges on the metal surface will not excite plasmons, but will be reflected. Plasmons are created by near-field interactions between the fluorophores and the metal. The near-fields around fluorophores have larger *k*-vectors, and are thus able to create plasmons which have a similarly large k-

vector. This process must be strongly dependent on distance and orientation. This reasoning also suggests that the emission will be directional with a sharply defined angle (θ_F). These angles would be different from θ_{SP} because the wavelengths are different. The dependence of θ_F on the wavelength suggests that different fluorophores will display directional emission at different angles determined by the emission maxima. If SPCE displays the same characteristics as SPR, then fluorophores near the metal film will emit into the prism at angles defined by the emission wavelength and by the optical properties of the metal at the emission wavelength. Based on the wavelength dependence seen in Fig. 34 we expect the longer wavelength Stokes' shifted emission to occur at smaller angles from the *z*-axis. This separation of wavelength has been observed for fluorophores on silver films (Fig. 37). This result shows that a simple metal film can be used to create directional emission and to separate different wavelengths (Fig. 38, top). There has been some confusion about this wavelength dependence on angle. The wavelength dependence of SPR and SPCE results from the wavelength dependence of the optical constants of the metals (see below).

Plasmon-coupled emission displays interesting polarization properties. Recall that SPR only occurs for the p-polarized component of the incident light because the projected wavevector of this component on the metal plane depends on the incident angle. Hence, SPCE is expected to be p-polarized at all angles around the cone, independently of the mode of excitation (Fig. 38). The p-polarization of SPR and SPCE leads to the impression that only dipole measurements perpendicular to the metal surface will couple with the metal and cause SPCE. From the far-field, the dipoles oriented perpendicular will result in p-polarized fields on the metal. However, the situation may be different for near-field interactions of the fluorophore with the metal surface, and we can expect to see coupling of fluorophores, parallel to the metal surface.

There are a number of publications on the theoretical aspects of fluorophores interacting with smooth metallic surfaces or mirrors.[14,60,128–131] This theory mostly describes fluorophores on or near thick metal films or mirrors. According to these papers there appears to be three possible processes for fluorophores near a smooth metal surface. The fluorophore can be quenched, can couple to surface plasmons or can emit into free-space. If the fluorophore is close to the surface ($d < 10$ nm) there is a high rate for radiationless deactivation and the emission appears to be quenched. At longer distances the reflected field interferes constructively or destructively, resulting in the oscillatory behavior reported for fluorophores in front of mirrors.[14] At distances from 20–100 nm the dominant decay rate is expected to be into the surface plasmons. The coupling of fluorophores over these longer distances explains why gold films can also be used to couple emission into the prism. Förster transfer to the gold surface is likely to be minimal at distances above 10 nm where SPCE is still efficient. This is important for the applications of SPCE because coupling will occur over a significant volume in the sample allowing detection of lower overall analyte concentrations. In addition, larger depths for SPCE allows for construction of bioassays with multiple layers of proteins or the use of a separation layer to protect the metallic layer against corrosion and adverse chemical reactions.

It is of interest to reconsider the observations that fluorophores are quenched within 10 nm of metal films. These observations can be traced to the early work showing decreased intensities of fluorophores close to mirrors or metal films near 100 nm thick.[14] This decrease in intensity is often described as due to lossy surface waves. However, we believe that the decreased intensities can be interpreted in a different way. At short distances, fluorophores induce plasmons on the metal surface. If the metal is thick the plasmons are trapped. Wavevector matching prevents them from radiating out of the metal into free-space. Since the metal is thick the plasmons cannot radiate into the glass substrate, and hence the optical energy is lost as heat. However, if the metal film is thin then plasmons can radiate into the substrate and be observed

as SPCE. Hence at least part of the quenching seen on mirrors is due to an indirect mechanism whereby the fluorophore crates the plasmon, which may (SPCE) or may not (quenching) radiate into the substrate.

Optical properties of surface plasmons

From the standpoint of fluorescence spectroscopy the absorption properties of surface plasmons can be confusing. The absorption spectral properties of fluorophores and small metal colloids are similar, but plasmons on surfaces display some unique features. Consider light incident on a fluorophore or a silver colloid (Fig. 39). These species display the familiar absorption spectra which are determined by the size and structure of the fluorophore or colloid. For a spherical colloid the amount of absorption is completely independent of the angle of incidence on the sample. Except for oriented systems the absorption of fluorophores is also independent of the angle of incidence. Now consider the reflectance spectra for the thin gold film shown in Fig. 34. The absorption is the same at 633, 700, 750 and 850 nm. The absorption of a thin metal film is mostly independent of wavelength and does not show a wavelength-dependent resonance comparable to fluorophores and colloids (Fig. 39). In contrast to a fluorophore, the absorption of a thin film depends on the angle of incidence. The reason for these different optical properties is that the wavelength of a surface plasmon is not completely determined by the film, but rather by the wavelength of the incident light. At long wavelength where the optical constants are relatively constant the wavelength of the induced plasmon is directly related to the incident wavelength [eqn (30)].

The different characteristics of fluorophore and surface plasmon absorption are further illustrated in Fig. 40. Suppose two wavelengths are incident on the fluorophore, and λ_1 is absorbed and λ_2 is not absorbed. A different result is obtained if these same two wavelengths are incident on a metal film. If the incidence angle is the surface plasmon angle then both wavelengths are absorbed. The wavelength of the surface plasmon is changed to match the incident wavelength. In the case of the fluorophore this shift is analogous to a shift in the absorption spectrum to match the incident wavelength.

The relationship between the surface plasmon wavelength λ_{SP} and the incident wavelength λ_0 is shown in Fig. 41. If the optical properties of the metal are independent of wavelength then for silver λ_{SP} is equal to about 75% of λ_0, $\lambda_{SP} = 0.75\lambda_0$. In this case the surface plasmon angle is independent of wavelength (Fig. 42). This result shows that the surface plasmon wavelength depends directly on the incident wavelength. However, the optical constants are dependent on wavelength, especially at shorter wavelengths. This dependence results in the dependence of λ_{SP} and θ_{SP} on the incident wavelength (Fig. 41 and Fig. 42). This is the reason for the angle-dependent wavelengths seen in Fig. 34 and Fig. 37.

Experimental studies of surface plasmon-coupled emission

During the past several years there have been an increased number of publications on SPCE to develop both a basic understanding of the phenomenon and to use SPCE for sensing applications.[132–135] In the following paragraphs we have selected examples which illustrate the general features of SPCE and its applications. An important feature of SPCE is the distances over which the fluorophores can couple to surface plasmons. This dependence can be studied by localizing fluorophores above the metal using methods such as layer-by-layer assembly or Langmuir–Blodgett films.[136,137] Fig. 43 shows the SPCE and free-space emission from the cyanine dye DiI at various distances over a silver film. By free-space emission we mean the emission into the air above the metal film. As the fluorophores become more distant from the metal these couple with lower efficiency and there is an increase in the free-space intensity. The free-space emission decreases rapidly as the fluorophores move closer to the metal. Almost all the free-space emission is eliminated below a distance of 20 nm, which is the distance for

the largest SPCE intensity. The angular SPCE distribution agrees well with the theoretical predictions (Fig. 44), which has been true for most of the published SPCE data. However there was some uncertainty in the efficiency of fluorophore coupling to the metal film. In all our experiments for fluorophores within about 20 nm from the metal surface, we observed most of the emission to occur at the SPCE angle with only a small fraction appearing as free-space emission (Fig. 44, left). Subsequently, a theory paper suggested that such high coupling efficiencies were not possible.[138] However, the calculations have been revised using the exact conditions of our experiment and there is now agreement that most of the energy is coupled into the plasmons.[137] At present the reason for the discrepancies is not known, but it appears that surface roughness and multiple dielectric layers may contribute to higher coupling efficiencies.

The high efficiency of coupling to metal films can be seen from the ability to image single molecules (Fig. 45). The single molecule intensities were found to be similar to those on glass alone, even though both the excitation and emission must pass across the silver film.[139] In fact, other laboratories have reported increased single molecule intensities for probes above metal films.[140,141] In single molecule detection (SMD) there is a direct comparison between the single molecule photon count rates. Hence, the SMD measurements prove the high sensitivity of SPCE measurements.

The high efficiency of SPCE and the localized coupling efficiency suggests its use for bioassays. Because the coupling is optimal at a distance near 20 nm from the surface it is practical to design surface-bound assays. Fig. 46 shows the emission spectra of an Alexa-labeled antibody bound to a capture antibody on a silver surface.[142] The Alexa emission can be detected even in whole blood with only a three-fold decrease in intensity compared to the buffer control. The sensitivity of SPCE can increase by the use of metal particles above the surface. Fig. 47 shows various smooth metal surfaces with silver particles above the substrate. Silver particles above silver and gold films provide the highest intensities.[143] A unique feature of this result is that the emission intensities were measured from the sample side, not through the glass substrate. Normally we would refer to the sample side emission as free-space emission. However, the metal particles act as high k-vector sources which increases the coupling efficiency of light both into and out of the metal. As we will describe shortly the control of k-vectors near metal surfaces provides numerous opportunities for new types of devices for fluorescence sensing.

As an introduction to the use of metallic nanostructures to control fluorescence we describe waveguide effects in SPCE. These effects occur when the dielectric sample thickens on the metal becomes comparable to the incident wavelength.[144,145] When this occurs there are multiple rings of SPCE, and the rings display alternating tangential and radial polarization (Fig. 48). The origin of these effects is that the thick dielectric film allows additional plasmon modes to exist on the metal and these modes can radiate into the substrate. This result shows that the single rings of SPCE represent only the simplest example of coupling fluorophores to metal surfaces. By controlling the dielectric thickness the SPCE angle and polarization can be controlled.

Plasmon-controlled fluorescence and metallic nanostructures

In the previous sections we described two types of metallic structures: metal particles for MEF and continuous thin metal films for SPCE. Metal particles and surfaces represent only a small fraction of the types of metallic structures which can be used to modify fluorescence. Many additional possibilities are available using metallic nanostructures with defined features. The underlying concept is to design the structure to provide wavevectors matching for the desired excitation and emission wavelengths. The structures can be designed to provide specific geometric and wavelength conditions for wavevector matching. Perhaps the simplest example

of such a structure is a metallic grating (Fig. 49), The presence of a periodic structure changes the conditions for wavevector matching. Suppose the sample is on an opaque silver grating with a pitch of λ_G = 600 nm. The condition for plasmon resonance is now given by

$$k_0 \sin\theta_{SP} = \pm k_{SP} \pm nG \tag{35}$$

where n is an integer and G is the propagation constant of the grating, $G = 2\pi/\lambda$.[146–149] The presence of the additional term $\pm nG$ has a dramatic effect on the surface plasmon coupling angles. Assume that the grating is silver and θ_{SP} for a similar planar surface is 50°. One can readily calculate that θ_{SP} for 500 nm is near 3.8° for the grating (Fig. 36). Emission at 600 and 700 nm will appear at 13.5 and 23.6° from the normal, respectively. The angular dispersion could be increased or decreased by changes in the pitch of the grating. Hence one could readily collect an emission spectrum with an array detector. The angular wavelength dispersion is somewhat different than diffraction. Diffraction is a far-field effect which depends on interference of propagating waves. The phenomenon described by eqn (35) depends both on grating pitch and the complex dielectric constant of the metal. The metal can be either thin (near 40 nm) or thick (near 200 nm). If the metal is thick the grating allows the radiation to couple out into the air or sample side of the structure. If the metal is thin the emission can couple out in either direction. In Fig. 37 we showed wavelength separation using SPCE. In this case the separation depended upon the intrinsic optical properties of the metal and there was little opportunity to modify the effect. By using a grating structure we can obtain the desired separation by controlling the dimensions of the grating.

The use of gratings for plasmon-controlled fluorescence (PCF) can go beyond wavelength resolution. Metal gratings are being used to increase the light output of LEDs.[149–151] If the grating is two-dimensional then the emission tends to beam away normal to the surface, with some angular separation of wavelengths. Additionally, gratings have been shown to be effective substrates for metal-enhanced fluorescence (MEF).[151,152] The enhancements depend on the wavelength of the fluorophore and the period of the grating. It seems likely that one- and two-dimensional gratings will soon find use in surface-bound fluorescence assays. The sensitivities can be increased by a combination of MEF due to the patterned structure and by directing more of the emission towards the detector.

Novel devices for fluorescence can be designed using the unique transmission properties of nano-hole arrays. Thick metal films with regular arrays of sub-wavelength holes are known to display optical transmission higher than expected for a similar non-metallic film.[153] This effect is shown in Fig. 50. The silver film was 300 nm thick, which is opaque in the absence of nano-holes. If the films contained nano-holes of sub-wavelength size there was efficient transmission through the films. The transmitted wavelength depended on the size and spacing of the holes which can be seen from the real color photographs of the films when back-illuminated with white light. The importance of this observation is that a metallic nanostructure displays unique optical properties distinct from those of a geometrically similar non-metallic structure. The unique optical properties of nano-hole arrays can potentially be used to make inexpensive devices for fluorescence sensing. One example is shown in Fig. 51 which consists of two nano-hole arrays with different spacing between the nano-holes. One array can be designed to transmit shorter wavelength green light for excitation, and the second array can be designed to transmit the longer wavelength red emission. At present, such a device may seem too expensive given the high cost of nanofabrication. However, there is rapid progress in high-throughput methods for nanofabrication. One example is microcontact printing (MCP). This method depends on nanofabrication of a master structure.[154,155] This structure can then be used to fabricate elastomer replicas, typically in PDMS but other harder polymers can also be

used. These replicate structures are then soaked in an ink such as a decanethiol and then used to print an image on a smooth metal film. The organic layer can protect the underlying metal from subsequent erosion steps, or to activate the printed regions by using a conjugatable thiol such as a decanethiol with a carboxy group on the opposite end. By the use of MCP or some other high-throughput method, metallic nanostructures can be made at very low cost, probably pennies per structure.

The schematic shown in Fig. 51 uses a nano-hole array as an optical filter. An important property of optical filters is their ability to selectively transmit or block selected wavelengths. The present nano-hole arrays have broad overlapping spectra and are not able to provide the needed wavelengths selectively. However, it is important to notice the remarkable progress in thin-film technology and interference filters. Twenty five years ago these filters were only available with a single transmission wavelength and typically inefficient transmission up to 20%. At present it is possible to purchase interference filters with almost any desired profile. Short and long wavelength pass filters can have very sharp cutoffs. Bandpass filters can have narrow or wide transmission bands. It is even possible to obtain a single filter with three transmission bands. It seems reasonable to expect similar progress in metal film filters and there is already ongoing work to control the optical properties of these structures. Nano-hole arrays have already been developed which have complete blockage of some wavelengths and high transmission of light shifted by 100 nm from the blocked wavelength.[156–158] The transmission spectra can be controlled using the spacing, shape of the holes, and the dielectric constant of the material filling the holes. The many variables which govern nano-hole transmission makes it complex to design nano-hole optical filters, but also provides the opportunity to use these parameters to obtain the desired optical characteristics.

In addition to serving as optical filters, nano-hole arrays can display transmission spectra which depend on the polarization.[159–161] Fig. 52 shows a nano-hole array with elongated nano-holes.[159] Also shown are photographs of the white light back-illuminated arrays through two polarizer orientations. The structure transmits green light when viewed through a polarizer illuminated along the short axis of the holes. Red light is observed when the polarizer is oriented along the long axis of the holes. These polarization properties of a nano-hole array may allow fabrication of a fluorometer (Fig. 53). Assume that the assay is based on DNA molecules binding on the surface of the array or in the nano-holes, which has already been proposed.[162] The array can be illuminated with green light and the transverse component will selectively couple to the structure. The emission will be mostly depolarized due to motion of the fluorophore or to a complex field polarization distribution in the nano-holes. The longer wavelength depolarized emission will selectively couple out of the distal side of the array. It should also be noted that the metal and glass have very different surface chemistries, so that molecules can be selectively bound to each surface. Hence a simple nano-hole array can provide the optical properties and chemical surfaces for a disposable sensing device.

It seems likely that elongated nano-hole arrays will be used for fluorescence polarization immunoassays (FPIs). These assays are widely used for monitoring of drugs and small molecule analytes.[163] A typical assay uses a labeled analyte analogue as a competitive ligand for the unlabeled analyte (Fig. 54). Suppose a capture antibody is bound to the metal surface and that a thin layer of sample is on top of the array. This sample will contain both bound and unbound labeled analyte. The polarization of this probe depends on whether it is free in solution or bound to the antibody. Suppose that the sample is illuminated with light polarized along an axis of the nano-holes. The emission from the bound probe will be polarized and have a larger parallel component $I_{\|}$ along the excitation polarization. The emission from the unbound probe will be unpolarized with a larger component perpendicular to ($I_{\perp}$) the incident polarization. Since the transmission of the array depends on polarization, the intensities transmitted along each axis will reflect the relative contributions of the free and bound probes and the FPI

instrument can consist of an elongated nano-hole array. Careful design of the nanostructure geometry will be needed to obtain the requisite selectivity to each polarized component of the emission.[160,161]

Plasmon transport

Another useful property of surface plasmons is their ability to propagate moderate distances across the metal surface. This effect is shown by finite-difference time-domain (FDTD) calculations for plasmons at an air–metal interface (Fig. 55). Using a metal film on a simple glass substrate the plasmons are seen to migrate over 12 microns.[164] One of the limiting factors in plasmon migration is the radiative loss of energy into the substrate. If the substrate has regions with two different dielectric constants then the plasmons can migrate well over 20 microns. The plasmon migration length is increased in the lower panel because the additional dielectric ε_3 causes total internal reflection and subsequent creation of additional plasmons. Additionally, it is possible to design the metal structures to obtain highly directional plasmons. One example consists of a 300 nm-thick gold film which contains a nanodot and several nanogrooves.[165] When this structure is illuminated from the back side the plasmons propagate almost exclusively in one direction (Fig. 56). Structural features of the structure can also be used to change the direction of plasmon migration (Fig. 57). The structure consists of grooves in a smooth metal film.[166] The FDTD calculations show the plasmons at different points in time (Fig. 57). The important feature to notice is that the plasmons are confined to the groove and follow the groove through sharp bends, similar to what is done using electrical circuits.

There is an ongoing effort to create optical elements for plasmons such as mirrors and beamsplitters.[167–169] When such devices become available it will be possible to treat the optical energy from fluorescence like an electrical current. Fig. 58 shows an example of a surface plasmon wavelength demultiplexer.[169] The device consists of a nano-hole array in a 50 nm-thick gold film. The plasmons are launched at a ridge in the structure. The plasmons created with two different wavelengths are deflected in different directions by the nano-hole array. These results show that optical energy in the form of plasmons can be manipulated in ways analogous to macroscopic optical components.

While it will be useful to trap and transport plasmons on surfaces, it will be necessary to transform the plasmons into free-space radiation for detection. Transformation of plasmons into free-space radiation can be accomplished using periodic nanostructures. In addition to converting the plasmons into free-space radiation the periodic structures can be designed to radiate the energy in a well-defined direction.[170–175] One example of a beaming structure is shown in Fig. 59.[170] In this case the structure consists of a nano-hole surrounded by concentric rings of Al and Ag. When illuminated from the far-field the structure transforms the energy into a well-defined beam which extends out to 100 μm (panel b). The spatial distribution of the light is very sensitive to the thickness of the dielectric above the metal. The most strongly beaming structure had a dielectric thickness of 100 nm. If the thickness is changed to 80 or 120 nm the radiation pattern is dramatically altered (panels a and c, respectively). Transmission of energy through a nano-hole in a metal film is very different from a nano-hole in an opaque dielectric. In the latter case there would be no beaming and the transmitted energy would be fully diffracted into the distal half-space. It is interesting to notice the high sensitivity of the radiation pattern in Fig. 59 to the dielectric thickness on the metal. A typical layer of proteins such as albumin and/or IgG is about 10 nm thick. This suggests a new configuration for surface plasmon resonance where protein binding changes the dielectric constant over the structure. Binding could be detected by changes in the radiation pattern due to protein binding.

In the previous paragraph we showed that the optical energy from the far-field can create radiating plasmons. However, we are interested in the radiating plasmons created by excited fluorophores.[176] We tested this possibility using FDTD calculations for a fluorophore near

concentric nano-rings (Fig. 60). We selected a metal-to-fluorophore distance that is comparable to the distance for a surface-bound immunoassay. We found that the near-field interactions of an oscillating dipole with the structure can create plasmons on the distal side, and these plasmons radiate to the far-field. An important feature of these plasmons is that the direction of the light depends on the dimensions of the structure and the frequency of the dipole. The energy from a 520 nm dipole radiates normal to the surface. The energy from shorter or longer wavelengths radiates at an angle away from the normal axis. Hence a nano-ring structure has the combined properties of providing directional radiation grating to direct the wavelength in the desired directions.

It is interesting to consider how these unique optical properties of metallic structures can be used in new format devices. Two examples are shown in Fig. 61. In one schematic (top) the excited fluorophores create plasmons which radiate towards the grating. The features near the excited fluorophores can be designed so that plasmons migrate in one direction. The trapped plasmon can be forced to emit into the substrate when it encounters lines in the metal film. This periodic structure can also separate the emission wavelengths. A second example is shown in the lower panel. In this case the incident light impinges on the entire sample. The dimensions of the nano-hole array can be chosen to transport specific wavelengths. The device can also contain concentric nano-ring structures. In this case the emission will radiate as a beam into the substrate. It is important to note that these devices consist only of structured metal films and that the entire device can be less than 10 microns long.

In all the devices shown so far we have considered the optical energy to be detected in the far-field using photodetectors, which transform the optical energy into electrical current. In a sense, plasmons are electrical current and it would be useful to detect the plasmons as current or potential. However, the plasmons are oscillating currents with no charge separation in the metal except for the oscillating electrons. To the best of our knowledge plasmons have not been detected directly as an electrical signal. However, there are now efforts to develop plasmon detectors.[177] One such device consists of a metal film with a slit to allow the creation of plasmons with illumination from the air side of the device (Fig. 62, top). The other part of the device is a p/n heterojunction organic diode consisting of p-type and n-type conductors. A charge separation is created when a plasmon is absorbed which generates an electrical current. This device can be used as a plasmon detector. The lower left panel of Fig. 62, (bottom) shows a reflectance image of the silver part of the device. Parts A and B are slits in the metal which generate the plasmons. The rectangle BS is cut into the metal to block the plasmons. Area B in the lower right image is a map of the electrical current as a diffraction-limited spot is scanned across the metal surface. When the incident beam encounters the slits A, a current is generated. Illumination of B generates fewer plasmons, and plasmons launched by B are blocked by the rectangle. The efficiency of this device is very low, 10^{-3}%. However, the important point is that there are many proof-of-principle experiments which demonstrate the possibility of a two-dimensional nano-scale device that performs all the functions now performed using lenses, filters, gratings and photodetectors. The two-dimensional nature of plasmon optics is similar to that found in modern computer circuits. In our opinion the basic technology exists for two-dimensional fluorescence circuits based on plasmon optics.

Observation of sub-wavelength volumes using plasmonic structures

In classical far-field optics the resolution is limited to about 400 nm across a diffraction-limited spot and about 2000 nm along the optical axis, for a volume of about 1 fl. In order to observe single molecules their emission must be detectable above the Raman scatter and background emission from this volume. As a result, single fluorophores can be observed only if these have high quantum yields and are contained in samples with low background emission. Conversely, if smaller volumes can be observed then it may become practical to detect single fluorophores

with lower quantum yield fluorophores or detection of single molecules in samples like serum or blood with high background emission. Metallic structures provide several ways to reduce the observed volumes. One approach is to use the increased fields between pairs of particles. There are many published calculations of the fields between particle dimers.[178,179] However, these calculations do not directly reveal how these fields can be used to obtain sub-wavelength observation volumes. While the fields may be localized it is still necessary to illuminate the structure and the size of the incident beam is still limited by diffraction.

We simulated the local fields induced between particle dimers included by the incident light (Fig. 63). The particles were assumed to be silver cylinders on a glass surface.[180] The FDTD calculations show that for suitably spaced nanodots the field is almost completely localized in the gap between the particles (left, linear scale). The degree of localization is even stronger for a pair of triangles (right). These latter intensities are shown on a log scale. Remarkably, we calculated that even if the entire nanotriangle area were coated with fluorophores, about 25% of the emission would come from the 16 × 16 nm gap region occupying less than 1% of the area. The field calculation suggests that if the triangle pair is uniformly coated with fluorophores a large fraction of the total emission will come from those fluorophores between the tips of the triangles. These calculations suggest that particle clusters can be used to obtain reduced volumes with typical macroscopic optics used to illuminate particle clusters.

Another approach to obtaining small volumes is to use the enhanced transmission through nano-holes. When nano-holes in metal films are illuminated there is typically an enhanced field in the nano-hole or above the nano-hole. This geometry may be preferred because the metal film is expected to block all the light so that the excitation field only exists in or above the nano-hole. However, it is known that light incident on a single nano-hole can induce plasmons on the distal side of the film,[181] so that completely localized excitation may not always occur. Nonetheless, nano-holes are promising structures for obtaining small volumes. Remarkably, the intensities from single molecules are enhanced several-fold compared to free solution.[182–186] One example of enhanced single molecule intensities and reduced volumes is shown in Fig. 64. The 300 nm-thick Au Flim is opaque and any observed light must be transmitted through the nano-hole. Even with this severe geometric constraint the single molecule brightness of Rh6G is six-fold larger than in solution. The fluorescence correlation spectroscopy (FCS) data show a dramatic reduction in observed volume. In FCS the time delay $\tau = 0$ intercept reflects the inverse of number of observed molecules. The concentrations of Rh6G in solution and in the nano-hole were 20 and 600 nM, respectively. Based on these concentrations the intercept for the nano-hole is expected to be 30-fold lower than for the solution, yet it is three-fold higher. This result reflects a 90-fold reduction in the observed volume for the nano-hole as compared to the solution.

It should be noted that other methods are being developed to obtain reduced volumes. One approach not based on plasmonics is to use sub-wavelength holes in an opaque film.[187,188] In this case only an evanescent wave can partially enter the nano-hole, and this evanescent wave serves as the excitation source. Reduced volumes can also be obtained using smooth metal films and SPCE.[189,190] In this case the primary advantage is localization of the volume close to the metal surface rather than restraining the volume in three dimensions. A promising approach to obtain an extremely small volume is to use tapered metallic waveguides.[191] Such structures can be used to obtain an optical field localized to about 5 nm (Fig. 65). Small optical apertures are used in near-field scanning optical microscopy (NSOM) but the spatial resolution is typically limited to about 75 nm because of low transmission through the aperture. It seems likely that NSOM instruments will soon be developed using tapered metal waveguides.

Sub-wavelength optical microscopy using plasmonic nanostructure

As described above, the wavelengths of surface plasmons are shorter than wavelengths in air or glass, and electric fields can be localized near and between metal particles. These sub-wavelength sizes of plasmons are being used in an attempt to develop optical microscopy with spatial resolution much greater than with present diffraction-limited optics.[192–195] The basic concept is shown in Fig. 66. In this case a nano-hole array is illuminated to excite sub-wavelength intensity spots on the distal side of the array. The nano-holes can be over a wavelength apart so that they do not interact and can be individually observed with a wide-field microscope. The array would scanned in-plane and the total image reconstructed from the individual images. Theoretical and experimental studies have demonstrated the existence of such small spots above plasmonic structures.[195–200] Fig. 67 shows an experimental demonstration using photolithography. The nano-holes were illuminated from the bottom with a photoresist on the top distal side. The resist was developed revealing the spatial distribution of the electric fields. Depending on the hole size the spots can be as small as 100 nm in diameter. The metal structure can be designed to obtain even smaller spots.[199] Fig. 68 shows simulations of the fields above a multi-layer structure. The electric field is confined to dimensions as small as $\lambda/20$.

The previous structures use the fields near nano-holes for sub-wavelength resolution. Another approach is to use the short wavelength of surface plasmons more directly.[200] In Fig. 41 we showed that the surface plasmon wavelength can be about two-fold shorter than the free-space wavelengths. Surface plasmons can be much shorter than $\lambda/2$. Remarkably, the plasmon wavelength can be as short as 10 nm and the predicted spatial resolution is near 20 nm (Fig. 69). In this example the spatial resolution is a result of changing the incident wavelength. Another approach is to use interference between surface plasmons.[201] This is shown by simulations of the fields on a grating structure (Fig. 70). The fields are seen to have dimensions near 50 nm.[201]

While these approaches to plasmonic microscopy seem promising there is a large technological barrier. The approaches shown in Fig. 66–70 depend on using the near-fields just above the metal surface. This means that the object needs to be in physical contact with the metal. This problem also occurs for the so-called perfect lens based on negative materials.[202–204] Recently we discovered an approach to obtain sub-wavelength size intensity distributions at micron distances above a nano-hole array.[205] At the same time similar reports appeared from other laboratories,[206–208] and on a related effect in two dimensions.[209] We observed these sub-wavelength size fields using near-field scanning optical microscopy (NSOM). We imaged the fields above a 4 × 4 nano-hole array in a 200 nm-thick silver film (Fig. 71). To our surprise we observed images of the 4 × 4 array at large distances of 20 microns or more above the array (Fig. 72). At other distances we observed more complex images and/or low intensity. We recognized that these images were related to the Talbot effect.[210,211] There are two important aspects of this observation. First, the fields can be confined to sub-wavelength dimensions as can be seen for the image appearing 11 microns above the surface. Secondly, the location of the field spots at these large distances shows that these fields can be used for cellular imaging. Cells on cover slips are typically several microns thick. One can readily imagine the nano-hole array being scanned below the cell (Fig. 66). Since the spots can be microns apart the spots can be imaged with classical optics and reconstruction of the complete image from the partial images. Additionally, it seems likely that methods will be developed to move the spots in the cell by changing the optical conditions for the nano-hole array, rather than physical movement of the array. Hence it seems likely that plasmonic structures will be used for a new class of microscope, in some cases with sub-wavelength resolution.

Perspective

Fluorescence has been studied for centuries, with the first publications by Herschel and Stokes near 1850 AD. Fluorescence has been used widely in the biosciences since the 1950s starting with the pioneering work of G. Weber. During these 150 years almost all fluorescence experiments utilized far-field illumination and observation. The use of plasmonic nanostructures represents a fundamental change in fluorescence. Instead of considering only the propagating radiation we are using the near-fields created by metals and excited fluorophores. Hence it is necessary to consider near-field interactions and nano-side optics. We need to understand which types of structures cause fluorescence enhancements and which structures cause quenching. These effects are somehow governed by the near- and far-field optical properties of metal structures, but at present a detailed understanding is lacking.

While there are many complexities to fluorophore–metal interactions there are also many opportunities. In addition to control of the chemical structure of the fluorophore we can now control, to some extent, the processes of excitation and emission. Additionally, we will be able to control the spatial distribution of fluorescence, not with macroscopic optics, but with nearby metallic nanostructures.

Acknowledgments

The author acknowledges support from the NIH, HG002655, EB000682 and EB0065211.

References

1. Strickler SJ, Berg RA. Relationship between absorption intensity and fluorescence lifetimes of molecules. J Chem Phys 1962;37:814–822.
2. Yguerabide J, Yguerabide EE. Light-scattering submicroscopic particles as highly fluorescent analogs and their use as tracer labels in clinical and biological applications: I. theory. Anal Biochem 1998;262:137–156. [PubMed: 9750128]
3. Yguerabide J, Yguerabide EE. Light-scattering submicroscopic particles as highly fluorescent analogs and their use as tracer labels in clinical and biological applications: II. experimental characterization. Anal Biochem 1998;262:157–176. [PubMed: 9750129]
4. Schultz DA. Plasmon resonant particles for biological detection. Curr Opin Biotechnol 2003;14:13–22. [PubMed: 12565997]
5. Cao YW, Jin R, Mirkin CA. DNA-modified core-shell Ag/Au nanoparticles. J Am Chem Soc 2001;123:7961–7962. [PubMed: 11493092]
6. Sokolov K, Follen M, Aaron J, Pavlova I, Malpica A, Lotan R, Richards-Kortum R. Real-time vital optical imaging of precancer using anti-epidermal growth factor receptor antibodies conjugated to gold nanoparticles. Cancer Res 2003;63:1999–2004. [PubMed: 12727808]
7. Schultz S, Smith SR, Mock JJ, Schulz DA. Single target molecule detection with nonbleaching multicolor optical immunolabels. Proc Natl Acad Sci U S A 2000;97:996–1001. [PubMed: 10655473]
8. Roll D, Malicka J, Gryczynski I, Gryczynski Z, Lakowicz JR. Metallic colloid wavelength-ratiometric scattering sensors. Anal Chem 2003;75:3440–3445. [PubMed: 14570195]
9. Chowdhury MH, Gray SK, Pond J, Geddes CD, Aslan K, Lakowicz JR. Computational study of fluorescence scattering by silver nanoparticles. J Opt Soc Am B 2007;24:2259–2267.
10. Mayergoyz ID, Zhang Z, Miano G. Analysis of dynamics of excitation and dephasing of plasmon resonance modes in nanoparticles. Phys Rev Lett 2007;98:147401. [PubMed: 17501311]
11. Pelton M, Liu M, Park S, Scherer NF, Guyor-Sionnest P. Ultrafast resonant optical sensing from single gold nanorods: Large nonlinearities and plasmon saturation. Phys Rev B 2006;73:155419.
12. Lakowicz JR. Radiative decay engineering: Biophysical and biomedical applications. Anal Biochem 2001;298:1–24. [PubMed: 11673890]

13. Lakowicz JR, Shen Y, D'Auria S, Malicka J, Fang J, Gryczynski Z, Gryczynski I. Radiative decay engineering. 2. Effects of silver island films on fluorescence intensity, lifetimes, and resonance energy transfer. Anal Biochem 2002;301:261–277. [PubMed: 11814297]
14. Drexhage KH. Influence of a dielectric interface on fluorescence decay time. J Lumin 1970;1–2:693–701.
15. Drexhage, KH. Progress in Optics XII. Wolf, E., editor. North-Holland, Amsterdam: 1974. p. 165
16. Ford GW, Weber WH. Electromagnetic effects on a molecule at a metal surface. Surf Sci 1981;109:451–481.
17. Chance RR, Prock A, Silbey R. Molecular fluorescence and energy transfer near interfaces. Adv Chem Phys 1973;37:1–65.
18. Ford GW, Weber WH. Electromagnetic interactions of molecules with metal surfaces. Phys Rep 1984;113(4):195–287.
19. Lakowicz JR. Radiative decay engineering 5: metal-enhanced fluorescence and plasmon emission. Anal Biochem 2005;337:171–194. [PubMed: 15691498]
20. Gersten J, Nitzan A. Spectroscopic properties of molecules interacting with small dielectric particles. J Chem Phys 1981;75(3):1139–1152.
21. Gersten, JI. Theory of fluorophore–metallic surface interactions. In: Geddes, CD.; Lakowicz, JR., editors. Topics in Fluorescence Spectroscopy, Vol. 8: Radiative Decay Engineering. Springer Science + Business Media, Inc.; New York: 2005. p. 197-221.
22. Guzatov DV, Klimov VV. Radiative decay engineering by triaxial nanoellipsoids. Chem Phys Lett 2005;412:341–346.
23. Gerber S, Reil F, Hohenester U, Schlagenhaufen T, Krenn JR, Leitner A. Tailoring light emission properties of fluorophores by coupling to resonance tuned metallic nanostructures. Phys Rev B 2007;75:073404.
24. Anger P, Bharadwaj P, Novotny L. Enhancement and quenching of single-molecule fluorescence. Phys Rev Lett 2006;96:113002. [PubMed: 16605818]
25. Bharadwaj P, Anger P, Novotny L. Nanoplasmonic enhancement of single-molecule fluorescence. Nanotechnology 2007;18:1–5.
26. Scharte M, Porath R, Ohms T, Aeschlimann M, Krenn JR, Ditlbacher H, Aussenegg FR, Liebsch A. Do Mie plasmons have a longer lifetime on resonance than off resonace? Appl Phys B 2001;73:305–310.
27. Teperik TV, Popov VV, Garcia de Abajo FJ. Radiative decay of plasmons in a metallic nanoshell. Phys Rev B 2004;69:155402.
28. Kelly, KL.; Jensen, TR.; Lazarides, AA.; Schatz, GC. Modeling metal nanoparticle optical properties. In: Feldheim, DL.; Foss, CA., editors. Metal Nanoparticles. Synthesis, Characterization, and Applications. Marcel Dekker, Inc.; New York: 2002. p. 89-118.
29. Kerker M, Blatchford CG. Elastic scattering, absorption, and surface-enhanced Raman scattering by concentric spheres comprised of a metallic and a dielectric region. Phys Rev B 1982;26(8):4052–4063.
30. Kreibig U, Gartz M, Hilger A. Mie resonances: sensors for hysical and chemical cluster interface properties'. Ber Bunsen-Ges Phys Chem 1997;101:1596–1604.
31. Bohren, CF.; Huffman, DR. Absorption and Scattering of Light by SmallParticles. John Wiley & Sons, Inc.; New York: 1983. p. 530
32. van de Hulst, HC. Light Scattering by Small Particles. Dover Publications, Inc; New York: 1957. p. 470
33. Kreibig, U.; Vollmer, M. Optical Properties of Metal Clusters. Springer-Verlag; New York: 1995.
34. Bohren, CF.; Huffman, D. MieCalc – freely configurable program for light scattering calculations (Mie theory). John Wiley; New York: 1983 [(accessed 17 June 2008)]. http://www.light-scattering.de/MieCalc/eindex.html
35. Kelly KL, Coronado E, Zhao LL, Schatz GC. The optical properties of metal nanoparticles: The influence of size, shape, and dielectric environment'. J Phys Chem B 2003;107:668–677.
36. Sosa IO, Noguez C, Barrera RG. Optical properties of metal nanoparticles with arbitrary shapes. J Phys Chem B 2003;107:6269–6275.

37. Draine, BT. The Discrete Dipole Approximation for Light Scattering by Irregular Targets. In: Mishchenko, MIJW.; Hovenier; Travis, LD., editors. Light Scattering by Nonspherical Particles: Theory, Measurements, and Geophysical Applications. Academic Press; New York, NY: 2000. p. 131-145.
38. Aslan K, Lakowicz JR, Geddes CD. Rapid deposition of triangular silver nanoplates on planar surfaces: application to metal-enhanced fluorescence. J Phys Chem B 2005;109:6247–6251. [PubMed: 16851692]
39. Michaels AM, Jiang J, Brus L. Ag nanocrystal junctions as the site for surface-enhanced Raman scattering of single rhodamine 6G molecules. J Phys Chem B 2000;104:11965–11971.
40. Nikoobakht B, El-Sayed MA. Surface-enhanced Raman scattering studies on aggregated gold nanorods. J Phys Chem A 2003;107:3372–3378.see also ref. 41
41. Messinger BJ, Ulrich von Raben K, Chang RK, Barber PW. Local fields at the surface of noble-metal microspheres. Phys Rev B 1981;24(2):649–657.
42. Bruzzone S, Malvaldi M, Arrighini GP, Guidotti C. Near-field and far-field scattering by bimetallic nanoshell systems. J Phys Chem B 2006;110:11050–11054. [PubMed: 16771364]
43. Bruzzone S, Malvaldi M, Arrighini GP, Guidotti C. Light scattering by gold nanoparticles: Role of simple dielectric models. J Phys Chem B 2004;108:10853–10858.
44. Prasad, PN. Nanophotonics. Wiley-Interscience; New Jersey: 2004. p. 415
45. Markel, VA.; George, TF., editors. Optics of Nanostructured Materials. John Wiley and Sons, Inc.; New York: 2001. p. 553
46. Novotny, L.; Hecht, B. Principles of Nano-Optics. Cambridge University Press; Cambridge, UK: 2006. p. 539
47. Shalaev, VM., editor. Optical Properties of Nanostructured Random Media. Springer; New York: p. 450
48. Ohtsu, M.; Kobayashi, K. Introduction to Classical and Quantum Theories of Electromagnetic Phenomena at the Nanoscale. Springer; Berlin, Heidelberg: 2004. Optical Near Fields; p. 205
49. Brongersma, ML.; Kik, PG., editors. Surface Plasmon Nanophotonics. Springer; Dordrecht, The Netherlands: p. 268
50. Shalaev, VM.; Kawata, S., editors. Nanophotonics with Surface Plasmons. Elsevier; Amsterdam: 2007. p. 321
51. Taflove, A.; Hagness, SC. Computational electrodynamics; The finite-difference time-domain. Artech House; Boston: 2000.
52. Yee KS. Numerical solution of initial boundary value problems involving Maxwell's equations in isotropic media. IEEE Trans Antennas Propagat 1966;14:302–307.
53. OptiFDTD software. Optiwave, Inc.; Ottawa, Canada:
54. FDTD Solutions software. Lumerical, Inc.; Vancouver, Canada:
55. FDTD Solutions™. Breault Research Organization; Tucson, AZ, USA: 2005.
56. EZ-FDTD+ software. Electromagnetic Simulation Company; Four Oaks, NC, USA:
57. Chowhury MH, Gray SK, Pond J, Geddes CG, Aslan K, Lakowicz JR. Computational study of fluorescence scattering by silver nanoparticles. J Opt Soc Am B 2007;24:2259–2267.
58. Sokolov K, Chumanov G, Cotton TM. Enhancement of molecular fluorescence near the surface of colloidal metal films. Anal Chem 1998;70:3898–3905. [PubMed: 9751028]
59. Amos RM, Barnes WL. Modification of the spontaneous emission rate of Eu^{3+} ions close to a thin metal mirror. Phys Rev B 1997;55(11):7249–7254.
60. Barnes WL. Fluorescence near interfaces: the role of photonic mode density. J Modern Opt 1998;45 (4):661–699.
61. Weitz DA, Garoff S, Hanson CD, Gramila TJ. Fluorescent lifetimes of molecules on silver-island films. Opt Lett 1982;7(2):89–91.
62. Aussenegg FR, Leitner A, Lippitsch ME, Reinisch H, Reigler M. Novel aspects of fluorescence lifetime for molecules positioned close to metal surfaces. Surf Sci 1987;139:935–945.
63. Leitner A, Lippitsch ME, Draxler S, Riegler M, Aussenegg FR. Fluorescence properties of dyes absorbed to silver islands, investigated by picosecond techniques. Appl Phys B 1985;36:105–109.

64. Gu T, Whitesell JK, Fox MA. Energy transfer from a surface bound arene to the gold core in fluorenyl-alkane-1-thiolate monolayer-protected gold clusters. Chem Mater 2003;15:1358–1366.

65. Gueroui Z, Liebchaber A. Single-molecule measurements of gold quenched quantum dots. Phys Rev Lett 2004;93:166108–166114. [PubMed: 15525013]

66. Ipe BI, Thomas KG. Photoinduced charge separation in a fluorophore-gold assembly. J Phys Chem B 2002;106:18–21.

67. Aguila A, Murray RW. Monolayer-protected clusters with fluorescent dansyl ligands. Langmuir 2000;16:5949–5954.

68. Yun CS, Javier A, Jennings T, Fisher M, Hira S, Peterson S, Hopkins B, Reich NO, Strouse GF. Nanometal surface energy transfer in optical rulers, breaking the FRET barrier. J Am Chem Soc 2002;127:3115–3119. [PubMed: 15740151]

69. Fan C, Wang S, Hong JW, Bazan GC, Plaxco KW, Heeger AJ. Beyond superquenching: Hyper-efficient energy transfer from conjugated polymers to gold-nanoparticles. Proc Natl Acad Sci U S A 2003;100:6297–6301. [PubMed: 12750470]

70. Zhang J, Lakowicz JR. Metal-enhanced fluorescence of an organic fluorophore using gold particles. Opt Express 2007;15(5):2598–2606. [PubMed: 19532498]

71. Garoff S, Weitz DA, Alvarez MS, Gersten JI. Electrodynamics at rough metal surfaces: Photochemistry and luminescence of adsorbance near metal-island films. J Chem Phys 1984;81(11): 5189–5200.

72. Ray K, Chowdhury M, Lakowicz JR. Aluminium nano-structured film as a substrate for enhanced fluorescence in the ultraviolet-blue spectral region. Anal Chem 2007;79(17):6480–6487. [PubMed: 17685553]

73. Lakowicz JR, Maliwal BP, Malicka J, Gryczynski Z, Gryzynski I. Effects of silver island films on the luminescent intensity and decay times of lanthanide chelates. J Fluoresc 2002;12(34):431–437.

74. Wu M, Lakowicz JR, Geddes CD. Enhanced lanthanide luminescence using silver nanostructures: Opportunities for a new class of probes with exceptional spectra characteristics. J Fluoresc 2005;15:53–59. [PubMed: 15711877]

75. Ray K, Badugu R, Lakowicz JR. Metal-enhanced fluorescence from CdTe nanocrystals: a single-molecule fluorescence study. J Am Chem Soc 2006;128:8998–8999. [PubMed: 16834349]

76. Okamoto K, Vyawahare S, Scherer A. Surface-plasmon enhanced bright emission from CdSe quantum-dot nanocrystals. J Opt Soc Am B 2006;23(8):1674–1678.

77. Shimizu KT, Woo WK, Fisher BR, Eisler HJ, Bawendi MG. Surface-enhanced emission from single semiconductor nanocrystals. Phys Rev Lett 2002;89(11):117401. [PubMed: 12225166]

78. Chowdhury MH, Ray K, Aslan K, Lakowicz JR, Geddes CD. Enhanced fluorescence of phycobiliproteins from plasmonic nanostructures. J Phys Chem C 2007;111:18856–18863.

79. Daniel E, Weber G. Cooperative effects in binding by bovine serum albumin, I: the binding of 1-anilino-8-naphthalenesulfonate. Fluorimetric titrations. Biochemistry 1966;5:1893–1900. [PubMed: 5963431]

80. Slavik J. Anilinonaphthalene sulfonate as a probe of membrane composition and function. Biochim Biophys Acta 1982;694:1–25. [PubMed: 6751394]

81. Benson SC, Zeng Z, Glazer AN. Fluorescence energy-transfer cyanine heterodimers with high affinity for double-stranded DNA. Anal Biochem 1995;231:247–255. [PubMed: 8678308]

82. Haq I, Ladbury JE, Chowdhry BZ, Jenkins TC, Chaires JB. Specific binding of Hoechst 33258 to the $D(CGCAAATTTGCG)_2$ duplex: calorimetric and spectroscopic studies. J Mol Biol 1997;271:244–257. [PubMed: 9268656]

83. Glazer AN, Peck K, Matheis RA. A stable double-stranded DNA ethidium homodimer complex: application to picogram fluorescence detection of DNA in agarose gels. Proc Natl Acad Sci U S A 1990;87:3851–3855. [PubMed: 2339125]

84. Rye HS, Yue S, Wemmer DE, Quesada MA, Haugland RP, Mathies RA, Glazer AN. Stable fluorescent complexes of double-stranded DNA with bis-intercalating asymmetric cyanine dyes: properties and applications. Nucleic Acids Res 1992;20(11):2803–2812. [PubMed: 1614866]

85. Malicka J, Gryczynski I, Lakowicz JR. DNA hybridization assays using metal-enhanced fluorescence. Biochem Biophys Res Commun 2003;306:213–218. [PubMed: 12788090]

86. Enderlein, J.; Zander, C. Theoretical foundations of single molecule detection in solution. In: Zander, Ch; Enderlein, J.; Keller, RA., editors. Single molecule detection in solution: methods and applications. Wiley-VCH; Darmstadt, Germany: 2002. p. 288-324.

87. Fu Y, Lakowicz JR. Enhanced fluorescence of Cy5-labeled DNA tethered to silver island films: Fluorescence images and time-resolved studies using single-molecule spectroscopy. Anal Chem 2006;78:6238–6245. [PubMed: 16944907]

88. Fu Y, Lakowicz JR. Enhanced fluorescence of Cy5-labeled oligonucleotides near silver island films: A distance effect study using single molecule spectroscopy. J Phys Chem B 2006;110:22557–22562. [PubMed: 17092001]

89. Zhang J, Fu Y, Chowdhury MH, Lakowicz JR. Single molecule studies on fluorescently labeled particles: Effects of particle size. J Phys Chem C 2009;112(1):18–26.

90. Kneipp K, Kneipp H, Deinum G, Itzkan I, Dasari RR, Feld MS. Single-molecule detection of a cyanine dye in silver colloidal solution using near-infrared surface-enhanced Raman scattering. Appl Spectrosc 1998;52(2):175–178.

91. Kneipp K, Wang Y, Kneipp H, Perelman L, Itzkan I, Dasari RR, Feld MS. Single molecule detection using surface-enhanced Raman scattering (SERS). Phys Rev Lett 1997;78(9):1667–1670.

92. Zhang J, Fu Y, Chowdhury MH, Lakowicz JR. Metal-enhanced single-molecule fluorescence on silver particle monomer and dimer: coupling effect between metal particles. Nano Lett 2007;7:2101–2107. [PubMed: 17580926]

93. Ullman EF, Schwarzberg M, Rubenstein KE. Fluorescent excitation transfer immunoassay: A general method for determination of antigens. J Biol Chem 1976;251(14):4172–4178. [PubMed: 945272]

94. Malicka J, Gryczynski I, Kusba J, Lakowicz JR. Effects of metallic silver island films on resonance energy transfer between *N*,*N*′-(dipropyl)-tetra-methyl-indocarbocyanine (Cy3)-and *N*,*N*′-(dipropyl)-tetramethyl-indodicarbo-cyanine (cy5) labeled DNA. Biopolymers 2003;70:595–603. [PubMed: 14648769]

95. Zhang J, Fu Y, Lakowicz JR. Enhanced Förster resonance energy transfer (FRET) on a single metal particle. J Phys Chem C 2007;111:50–56.

96. Gersten JI, Nitzan A. Accelerated energy transfer between molecules near a solid particle. Chem Phys Lett 1983;104:31–37.

97. Hua XM, Gersten JI, Nitzan A. Theory of energy transfer between molecules near solid state particles. J Chem Phys 1985;83:3650–3654.

98. Gersten, JI. Topics in Fluorescence Spectroscopy, Volume 8: Radiative Decay Engineering. Springer; New York: 2005. Theory of fluorophore–metallic surface interactions; p. 197-221.

99. Christenson RH, Azzazy HME. Evidence based approach to practice guides and decision thresholds for cardiac markers. Scand J Clin Lab Invest 1999;59(suppl 230):90–102.

100. Newby LK, Storrow AB, Gibler WB, Garvey JL, Tucker JF, Kaplan AL, Schreiber DH, Tuttle RH, Mc-Nulty SE, Ohman EM. Bedside multimarker testing for risk stratification in chest pain units: The chest pain evaluation by creatine kinase-MB, myoglobin, and troponin I(CHECKMATE) study. Circulation 2001;103:1832–1837. [PubMed: 11294799]

101. Christenson RH, Azzazy HME. Biochemical markers of the acute coronary syndromes. Clin Chem (Washington, D C) 1998;44:1855–1864.

102. Zhang Z, Fu Y, Lakowicz JR. Enhanced Förster resonance energy transfer (FRET) on single metal particle 2: Dependence on donor–acceptor separation distance, particle size, and distance from metal surface. J Phys Chem C 2007;111:11784–11792.

103. Enderlein J. Spectral properties of a fluorescing molecule within a spherical metallic cavity. Phys Chem Chem Phys 2002;4:2780–2786.

104. Enderlien J. Theoretical study of single molecule fluorescence in a metallic nanocavity. Appl Phys Lett 2002;80:315–317.

105. Zhang J, Gryczynski I, Gryczynski Z, Lakowicz JR. Dye-labeled silver nanoshell–bright particle. J Phys Chem B 2006;110:8986–8991. [PubMed: 16671705]

106. Aslan K, Lakowicz JR, Geddes CG. Metal enhanced fluorescence solution-based sensing platform 2: fluorescent core-shell Ag@SiO_2 nanoballs. J Fluoresc 2007;17:127–131. [PubMed: 17279332]

107. Aslan K, Wu M, Lakowicz JR, Geddes CG. Fluorescent core–shell Ag@SiO_2 nanocomposites for meta-enhanced fluorescence and single nanoparticle sensing platforms. J Am Chem Soc 2007;129:1524–1425. [PubMed: 17283994]
108. Kuczynski JP, Milosavljevic BH, Thomas JK. Effect of the synthetic preparation on the photochemical behavior of colloidal CdS. J Phys Chem 1983;87:3368–3370.
109. Ramsden JJ, Gratzel M. Photo-luminescence of small cadmium sulfide particles. J Chem Soc, Faraday Trans 1984;80:919–933.
110. Bruchez M, Moronne M, Gin P, Weiss S, Alivisatos AP. Semi-conductor nanocrystals as fluorescent biological labels. Science 1998;281:2013–2016. [PubMed: 9748157]
111. Lakowicz JR. Radiative Decay Engineering 3. Surface plasmon coupled directional emission. Anal Biochem 2004;324:153–169. [PubMed: 14690679]
112. Gryczynski I, Malicka J, Gryczynski Z, Lakowicz JR. Radiative Decay Engineering 4. Experimental studies of surface plasmon-coupled directional emission. Anal Biochem 2004;324:170–182. [PubMed: 14690680]
113. Calander N. Surface plasmon-coupled emission and Fabry–Perot resonance in the sample layer: A theoretical approach. J Phys Chem B 2005;109:13957–13956. [PubMed: 16852751]
114. Calander N. Theory and simulation of surface plasmon-coupled directional emission from fluorophores at planar stuctures. Anal Chem 2004;76:2168–2173. [PubMed: 15080724]
115. Salamon Z, Macleod HA, Tollin G. Surface plasmon resonance spectroscopy as a tool for investigating the biochemical and biophysical properties of membrane protein systems. I: Theoretical principles. Biochim Biophys Acta 1997;1331:117–129. [PubMed: 9325438]
116. Melendez J, Carr R, Bartholomew DU, Kukanskis K, Elkind J, Yee S, Furlong C, Woodbury R. A commercial solution for surface plasmon sensing. Sens Actuators, B 1996;35–36:212–216.
117. Liedberg B, Lundstrom I. Principles of biosensing with an extended coupling matrix and surface plasmon resonance. Sens Actuators, B 1993;11:63–72.
118. Cooper MA. Optical biosensors in drug discovery. Nat Rev 2002;1:515–528.
119. Wegner GJ, Lee HJ, Corn RM. Characterization and optimization of peptide arrays for the study of epitope-antibody interactions using surface plasmon resonance imaging. Anal Chem 2002;74:5161–5168. [PubMed: 12403566]
120. Natan, MJ.; Lyon, LA. Surface plasmon resonance biosensing with colloidal Au amplification. In: Feldheim, DL.; Foss, CA., editors. Metal Nanoparticles: Synthesis, Characterization, and Applications. Marcel Dekker; New York: 2002. p. 183-205.
121. Born, M.; Wolf, E. Principles of Optics. Electromagnetic theory of propagation, interference and diffraction of light. Pergamon Press; New York: 1980. p. 808
122. Johnson BP, Christy RW. Optical constants of the noble metals. Phys Rev B 1972;6(12):4370–4379.
123. Heavens, OS. Optical Properties of Thin Solid Films. Dover Publications; New York: 1955. p. 261
124. Raether, H. Surface Plasma Oscillations and Their Applications. In: Hass, G.; Francombe, MH.; Hoffman, RW., editors. Physics of Thin Films, Advances in Research and Development. Vol. 9. Academic Press; New York: 1977. p. 145-261.
125. Melikyan A, Minassain H. On surface plasmon damping in metallic nanoparticles. Appl Phys B 2004;78:453–455.
126. Ziegler T, Hendrich C, Hubenthal F, Vartanyan T, Trager F. Dephasing times of surface plasmon excitation in Au nanoparticles determined by persistent spectral hole burning. Chem Phys Lett 2004;386:319–324.
127. Miranda MHG, Facao-Filho EL, Rodrigues Cid JJ, de Araujo CB, Acioli LH. Ultrafast light-induced dichroism in silver nanopartcles. Phys Rev B 2004;70:161401.
128. Yih J, Chien F, Lin C, Yau H, Chen S. Angular interrogation attenuated total reflection metrology system for plasmonic structures. Appl Opt 2005;44:6155–6162. [PubMed: 16237928]
129. Skivesen N, Horvath R, Pederson HC. Optimization of metal-clad waveguide sensors. Sens Actuators, B 2005;106:668–676.
130. Benner RE, Dornhaus R, Chang RK. Angular emission profiles of dye molecules excited by surface plasmon waves at a metal surface. Opt Commun 1979;30(2):145–149.

131. Weber WH, Eagen CF. Energy transfer from an excited dye molecule to the surface plasmons of an adjacent metal. Opt Lett 1979;4(8):236–238.

132. Isfort G, Schierbaum K, Zerulla D. Causality of surface plasmon polariton emission processes. Phys Rev B 2006;73:033408.

133. Chowdhury MH, Malyn SN, Aslan K, Lakowicz JR, Geddes JR. Multicolor directional surface plasmon coupled chemiluminescence. J Phys Chem B 2006;110:22644–22651. [PubMed: 17092012]

134. Kostov Y, Smith DS, Tolosa L, Rao G, Gryczynski I, Gryczynski Z, Malicka J, Lakowicz JR. Directional surface plasmon-coupled emission from a 3 nm green fluorescent protein monolayer. Biotechnol Prog 2005;21:1731–1735. [PubMed: 16321058]

135. Neal TD, Okamoto K, Scherer A. Surface plasmon enhanced emission from dye doped polymer layers. Opt Express 2005;13(14):5522–5527. [PubMed: 19498548]

136. Ray K, Badugu R, Lakowicz JR. Sulforhodamine adsorbed Langmuir–Blodgett layers on silver island films: Effect of probe distance on the metal-enhanced fluorescence. J Phys Chem C 2007;111:7091–7097.

137. Ray K, Szmacinski H, Enderlein J, Lakowicz JR. Distance dependence of surface plasmon-coupled emission observed using Langmuir–Blodgett films. Appl Phys Lett 2007;90:251116.

138. Enderlein J, Ruckstuhl T. The efficiency of surface-plasmon coupled emission for sensitive fluorescence detection. Opt Express 2005;13(22):8855–8865. [PubMed: 19498918]

139. Ray K, Lakowicz JR. unpublished observations

140. Stefani FD, Vasilev K, Bocchio N, Stoyanova N, Kreiter M. Surface-plasmon-mediated single molecule fluorescence through a thin metallic film. Phys Rev Lett 2005;94:023005. [PubMed: 15698172]

141. Vasilev K, Knoll W, Kreiter M. Fluorescence intensities of chromophores in front of a thin metal film. J Chem Phys 2004;120(7):3439–3445. [PubMed: 15268501]

142. Matveeva EG, Gryczynski Z, Malicka J, Lukomska J, Makowiec S, Berndt KW, Lakowicz JR, Gryczynski I. Directional surface plasmon-coupled emission: Application for an immunoassay in whole blood. Anal Biochem 2005;344:161–167. [PubMed: 16091280]

143. Matveeva EG, Gryczynski I, Barnett A, Leonenko Z, Lakowicz JR, Gryczynski Z. Metal particle-enhanced fluorescent immunoassays on metal mirrors. Anal Biochem 2007;363:239–245. [PubMed: 17316540]

144. Gryczynski I, Malicka J, Nowaczky K, Gryczynski Z, Lakowicz JR. Waveguide-modulated surface plasmon-coupled emission of Nile blue in poly(vinyl alcohol) thin films. Thin Solid Films 2006;510:15–20.

145. Gryczynski I, Malicka J, Nowaczyk K, Gryczynski Z, Lakowicz JR. Effects of sample thickness on the optical properties of surface plasmon-coupled emission. J Phys Chem B 2004;108:12073–12083.

146. Yu F, Tian S, Yao D, Knoll W. Surface plasmon enhanced diffraction for label-free biosensing. Anal Chem 2004;76:3530–3535. [PubMed: 15228321]

147. Yu F, Knoll W. Immunosensor with self-referencing based on surface plasmon diffraction. Anal Chem 2004;76:1971–1975. [PubMed: 15053659]

148. Wang Y, Zhou Z. Strong enhancement of erbium ion emission by a metallic double grating. Appl Phys Lett 2006;89:25312.

149. Gifford DK, Hall DG. Emission through one of two metal electrodes of an organic light-emitting diode *via* surface-plasmon cross coupling. Appl Phys Lett 2002;81(23):4315–4317.

150. Feng J, Okamoto T, Kawata S. Highly directional emission *via* coupled surface-plasmon tunneling from electro-luminescence in organic light-emitting devices. Appl Phys Lett 2005;87:241109.

151. Matthews DR, Summers HD, Njoh K, Chappell S, Errington R, Smith P, Pope I, Barber P, Vojnovic B, Ameer-Beg S. A fluorescence biochip with a plasmon active surface. Proc SPIE–Int Soc Opt Eng 2007;6450:645006.

152. Hung YJ, Smolyaninov II, Davis CC. Fluorescence enhancement by surface gratings. Opt Express 2006;14(2):10825–10830. 157. [PubMed: 19529494]

153. Ebbesen TW, Lezec HJ, Ghaemi HF, Thio T, Wolf PA. Extraordinary optical transmission through sub-wavelength hole arrays. Nature 1998;391:667–669.

154. Xia Y, Whitesides GM. Soft lithography. Annu Rev Mater Sci 1998;28:153–184.

155. Milan M, Whitesides GM. Patterning self-assembled monolayers using microcontact printing: a new technology for biosensors? Trends Biotechnol 1995;13:228–231.

156. Tetz KA, Pang L, Fainman Y. High-resolution surface plasmon resonance sensor based on linewidth-optimized nanohole array transmittance. Opt Lett 2006;31(10):1528–1530. [PubMed: 16642161]

157. Kim JH, Moyer PJ. Transmission characteristics of metallic equilateral triangular nanohole arrays. Appl Phys Lett 2006;89:121106.

158. Chen Y, Wang Y, Zhang Y, Liu S. Numerical investigation of the transmission enhancement through subwavelength hole arrays. Opt Commun 2007;274:236–240.

159. DiMaio JR, Ballato J. Polarization-dependent transmission through subwave-length anisotropic aperture arrays. Opt Express 2006;14(6):2380–2384. [PubMed: 19503576]

160. van der Molen KL, Koerkamp KJ, Enoch S, Segerink FB, van Hulst NF, Kuipers L. Role of shape and localized resonances in extraordinary transmission through periodic arrays of subwavelength holes: experiment and theory. Phys Rev B 2005;72:045421.

161. Elliott J, Smolyaninov II, Zheludev NI, Zayats AV. Polarization control of optical transmission of a periodic array of elliptical nanoholes in metal film. Opt Lett 2004;29(12):1414–1416. [PubMed: 15233453]

162. Liu Y, Bishop J, Williams L, Blair S, Hebron J. Biosensing based upon molecular confinement in metallic nanocavity arrays. Nanotechnology 2004;15:1368–1374.

163. Dandliker, Wb; de Saussure, VA. Fluorescence polarization in immunochemistry. Immunochemistry 1970;7:799–828. [PubMed: 4099599]

164. Lee TW, Gray SK. Regenerated surface plasmon polaritons. Appl Phys Lett 2005;86:141105.

165. Lopez-Tejeira F, Rodrigo SG, Martin-Moreno L, Garcia-Vidal FJ, Devaux E, Ebbesen TW, Krenn JR, Radko IP, Bozhevolnyi SI, Gonzalez MU, Weeber JC, Dereux A. Efficient unidirectional nanoslit couplers for surface plasmons. Nat Phys 2007;3:324–328.

166. Lee TW, Gray SK. Subwavelength light bending by metal slit structures. Opt Express 2005;13(24): 9652–9659. [PubMed: 19503170]

167. Ditlbacher H, Krenn JR, Schider G, Leitner A, Aussenegg FR. Two-dimensional optics with surface plasmon polaritons. Appl Phys Lett 2002;81(10):1762.

168. Krasavin AV, Zayats AV. Passive photonic elements based on dielectric-loaded surface plasmon plariton waveguides. Appl Phys Lett 2007;90:211101–1.

169. Drezet A, Koller D, Hohenau A, Leitner A, Aussenegg FR, Krenn JR. Plasmonic crystal demultiplexer and multiports. Nano Lett 2007;7(6):1697–1700. [PubMed: 17500579]

170. Wang B, Wang GP. Directional beaming of light from a nanoslit surrounded by metallic heterostructures. Appl Phys Lett 2006;88:013114.

171. Li ZB, Tian JG, Zhou WY, Zhang WP, Zhang C. Periodic dielectric bars assisted enhanced transmission and directional light emission from a single subwavelength slit. Opt Express 2006;14 (18):8037–8042. [PubMed: 19529174]

172. Martin-Moreno L, Garcia-Vidal FJ, Lezec HJ, Degiron A, Ebbesen TW. Theory of highly directional emission from a single subwavelength aperture surrounded by surface corrugations. Phys Rev Lett 2003;90(16):167401. [PubMed: 12732005]

173. Caglayan H, Bulu I, Ozbay E. Beaming of electromagnetic waves emitted through a subwavelength annular aperture. J Opt Soc Am B 2006;23(3):419–422.

174. Lin DZ, Chang CK, Chen YC, Yang DL, Lin MW, Yeh JT, Liu JM, Kuan CH, Yeh CS, Lee CK. Beaming light from a subwavelength metal slit surrounded by dielectric surface gratings. Opt Express 2006;14(8):3503–3511. [PubMed: 19516497]

175. Lezec HJ, Degiron A, Devaux E, Linke RA, Martin-Moreno L, Garcia-Vidal FJ, Ebbesen TW. Beaming light from a subwavelength aperture. Science 2002;297:820–822. [PubMed: 12077423]

176. Chowdhury M, Lakowicz JR. unpublished observations

177. Ditlbacher H, Aussenegg FR, Krenn JR, Lamprecht B, Jakopic G, Leising G. Organic diodes as monolithically integrated surface plasmon polariton detectors. Appl Phys Lett 2006;89:161101.

178. Jin EX, Xu X. Enhanced optical near field from a bowtie aperture. Appl Phys Lett 2006;88:153110.
179. Wang L, Uppuluri SM, Jin EX, Xu X. Nanolithography using high transmission nanoscale bowtie apertures. Nano Lett 2006;6(3):361–364. [PubMed: 16522023]
180. Chowdhury MC, Lakowicz JR. unpublished observations
181. Yin L, Vlasko-Vlasov VK, Rydh A, Pearson J, Welp U, Chang SH, Gray SK, Schatz GC, Brown DB, Kimball CW. Surface plasmons at single nanoholes in Au films. Appl Phys Lett 2004;85(3): 467–469.
182. Popov E, Neviere M, Wenger J, Lenne PF, Rigneault H, Chaumet P. Field enhancement in single subwave-length apertures. J Opt Soc Am A 2006;23(9):2342–2348.
183. Kim JH, Moyer PJ. Laser-induced fluorescence within subwavelength metallic arrays of nanoholes indicating minimal dependence on hole periodicity. Appl Phys Lett 2007;90:131111.
184. Wenger J, Lenne PF, Popov E, Rigneault H. Single molecule fluorescence in rectangular nano-apertures. Opt Express 2005;13(18):7035–7044. [PubMed: 19498725]
185. Rigneault H, Capoulade J, Dintinger J, Wenger J, Bonod N, Popov E, Ebbesen TW, Lenne PF. Enhancement of single-molecule fluorescence detection in subwavelength apertures. Phys Rev Lett 2005;95:117401. [PubMed: 16197045]
186. Liu Y, Mahdavi F, Blair S. Enhanced fluorescence transduction properties of metallic nanocavity arrays. IEEE J Sel Top Quantum Electron 2005;11(4):778–784.
187. Samiee KT, Moran-Mirabal JM, Cheung YK, Craighead HG. Zero mode waveguides for single-molecule spectroscopy on lipid membranes. Biophys J 2006;90:3288–3299. [PubMed: 16461393]
188. Levene MJ, Korlach J, Turner SW, Foquet M, Craighead HG, Webb WW. Zero-model waveguides for single-molecule analysis at high concentrations. Science 2003;299:682–686. [PubMed: 12560545]
189. Gryczynski Z, Borejdo J, Calander N, Matveeva EG, Gryczynski I. Minization of detection volume by surface plasmon-coupled emission. Anal Biochem 2006;356:125–131. [PubMed: 16764813]
190. Gryczynski I, Malicka J, Lakowicz JR, Goldys EM, Calander N, Gryczynski Z. Directional two-photon induced surface plasmon-coupled emission. Thin Solid Films 2005;491:173–176.
191. Issa NA, Guckenberger R. Optical nanofocusing on tapered metallic waveguides. Plasmonics 2007;2:31–37.
192. Garini Y, Kutchoukov VG, Bossche A, Alkemade PFA, Docter M, Verbeek PW, van Vliet LJ, Young IT. Toward the development of a three-dimensional mid-field microscope. Proc SPIE–Int Soc Opt Eng 2004;5327:115–122.
193. Docter MW, Young IT, Kutchoukov VG, Bossche A, Alke-made PFA, Garini Y. A novel concept for a mid-field microscope. Proc SPIE–Int Soc Opt Eng 2005;5703:118–126.
194. Smolyaninov II, Elliott J, Zayats AV, Davis CC. Far-field optical microscopy with a nanometer-scale resolution based on the in-plane image magnification by surface plasmon polaritons. Phys Rev Lett 2005;94:057401. [PubMed: 15783692]
195. Zayats AV, Elliott J, Smolyaninov II, Davis CC. Imaging with short-wavelength surface plasmon polaritons. Appl Phys Lett 2005;86:151114.
196. Chang SH, Gray SK, Schatz GC. Surface plasmon generation and light transmission by isolated nanoholes and arrays of nanoholes in thin metal films. Opt Express 2005;13(8):3150–2165. [PubMed: 19495214]
197. Guo X, Du J, Guo Y. Large-area surface-plasmon polariton interference lithography. Opt Lett 2006;31(17):2613–2165. [PubMed: 16902636]
198. Amarie D, Rawlinson ND, Schaich WL, Dragnea B, Jacobson SC. Three-dimensional mapping of the light intensity transmitted through nanoapertures. Nano Lett 2005;5(7):1227–1230. [PubMed: 16178215]
199. Zayats AV, Smolyaninov II. High-optical throughput individual nanoscale aperture in a multilayered metallic films. Opt Lett 2006;31(3):398–400. [PubMed: 16480221]
200. Luo X, Ishihara T. Subwave-length photolithography based on surface-plasmon polariton resonance. Opt Express 2004;12(14):3055–3065. [PubMed: 19483824]
201. Liu ZW, Wei QH, Zhang X. Surface plasmon interference nanolithography. Nano Lett 2005;5(5): 957–961. [PubMed: 15884902]

202. Pendry JB. Negative refraction makes a perfect lens. Phys Rev Lett 2000;85(18):3966–3969. [PubMed: 11041972]

203. Fang N, Lee H, Sun C, Zhang X. Sub-diffraction limited optical imaging with a silver superlens. Science 2005;308:534–537. [PubMed: 15845849]

204. Podolskiy VA, Narimanov EE. Near-sighted superlens. Opt Lett 2005;30(1):75–77. [PubMed: 15648643]

205. Chowdhury MH, Catchmark JM, Lakowicz JR. Imaging three-dimensional light propagation through periodic nanohole arrays using scanning aperture microscopy. Appl Phys Lett 2007;91:103118.

206. Feng S, Halterman K, Overfelt PL. Subwavelength fractional Talbot effect in layered heterostructures of composite metamaterials. Phys Rev E 2006;74:036612.

207. Huang FM, Zheludev N, Chen Y, de Abajo FJG. Focusing of light by a nanohole array. Appl Phys Lett 2007;90:091119.

208. Fu Z, Zhou W, Lim LEN, Du CL, Luo XG. Plasmonic microzone plate: Superfocusing at visible regime. Appl Phys Lett 2007;91:061124.

209. Dennis MR, Zheludev NI, de Abajo FJG. The plasmon Talbot effect. Opt Express 2007;15(15): 9692–9700. [PubMed: 19547318]

210. Noponen E, Turunen J. Electromagnetic theory of Talbot imaging. Opt Commun 1993;98:132–140.

211. Arrizon V, Rojo-Velazquez G, Ibarra JG. Fractional Talbot effect: Compact description. Opt Rev 2000;7(2):129–131.

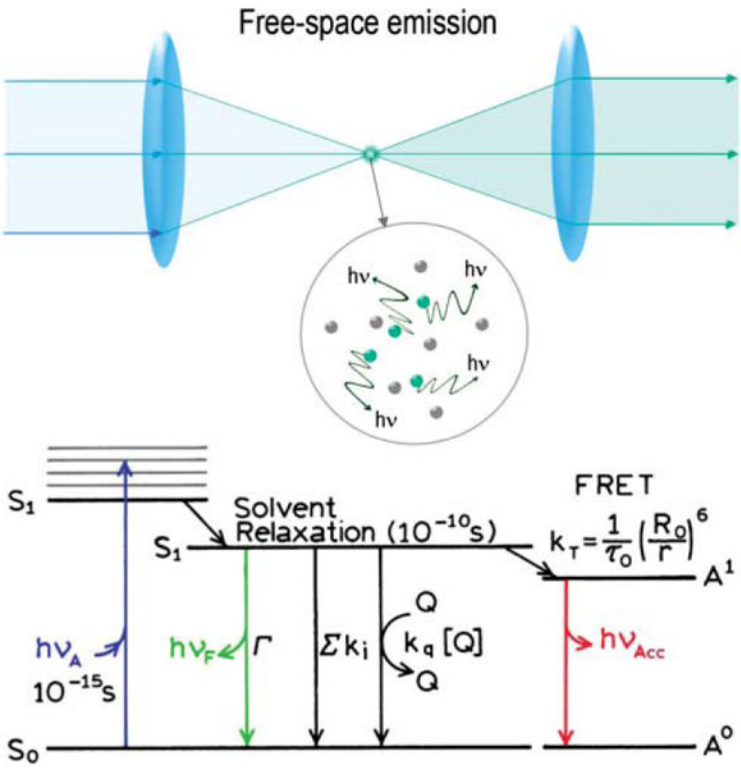

Fig. 1.
Free-space emission and Jablonski diagram.

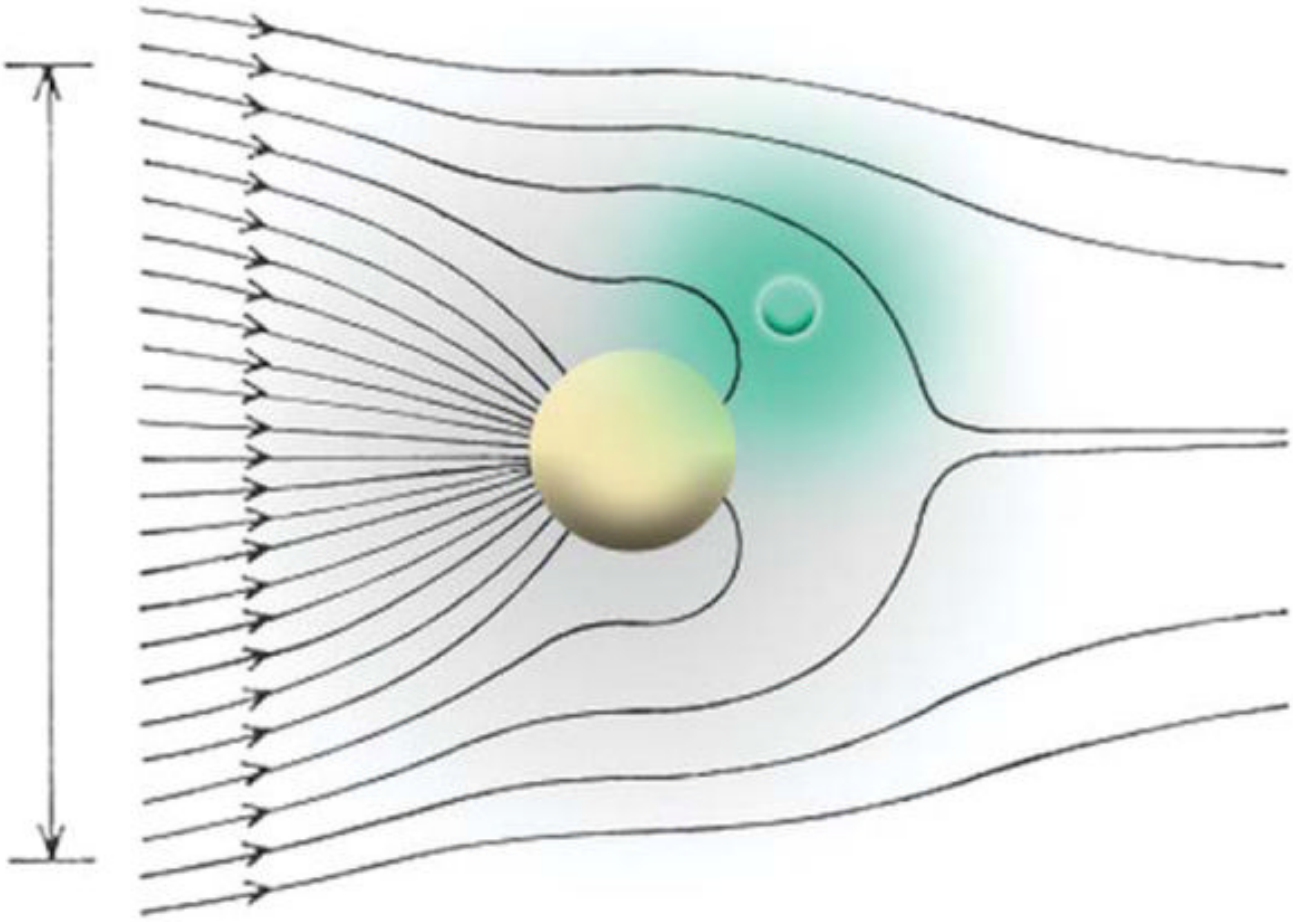

Fig. 2.
Interaction of a metal colloid with incident light. The lines show the direction of light propagation. Also shown is a fluorophore in the near-field around the colloid.

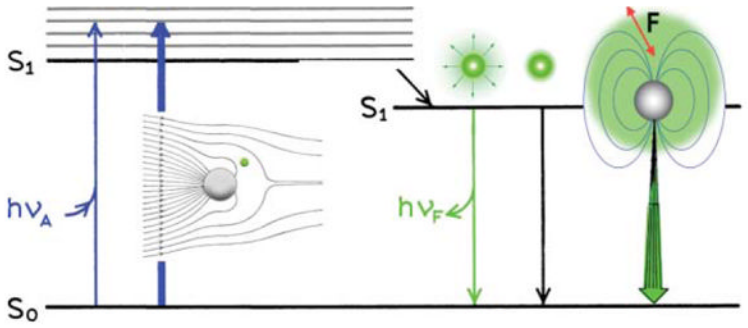

Fig. 3.
Modified Jablonski diagram which includes metal–fluorophore interactions. The thicker arrows represent increased rates of excitation and emission.

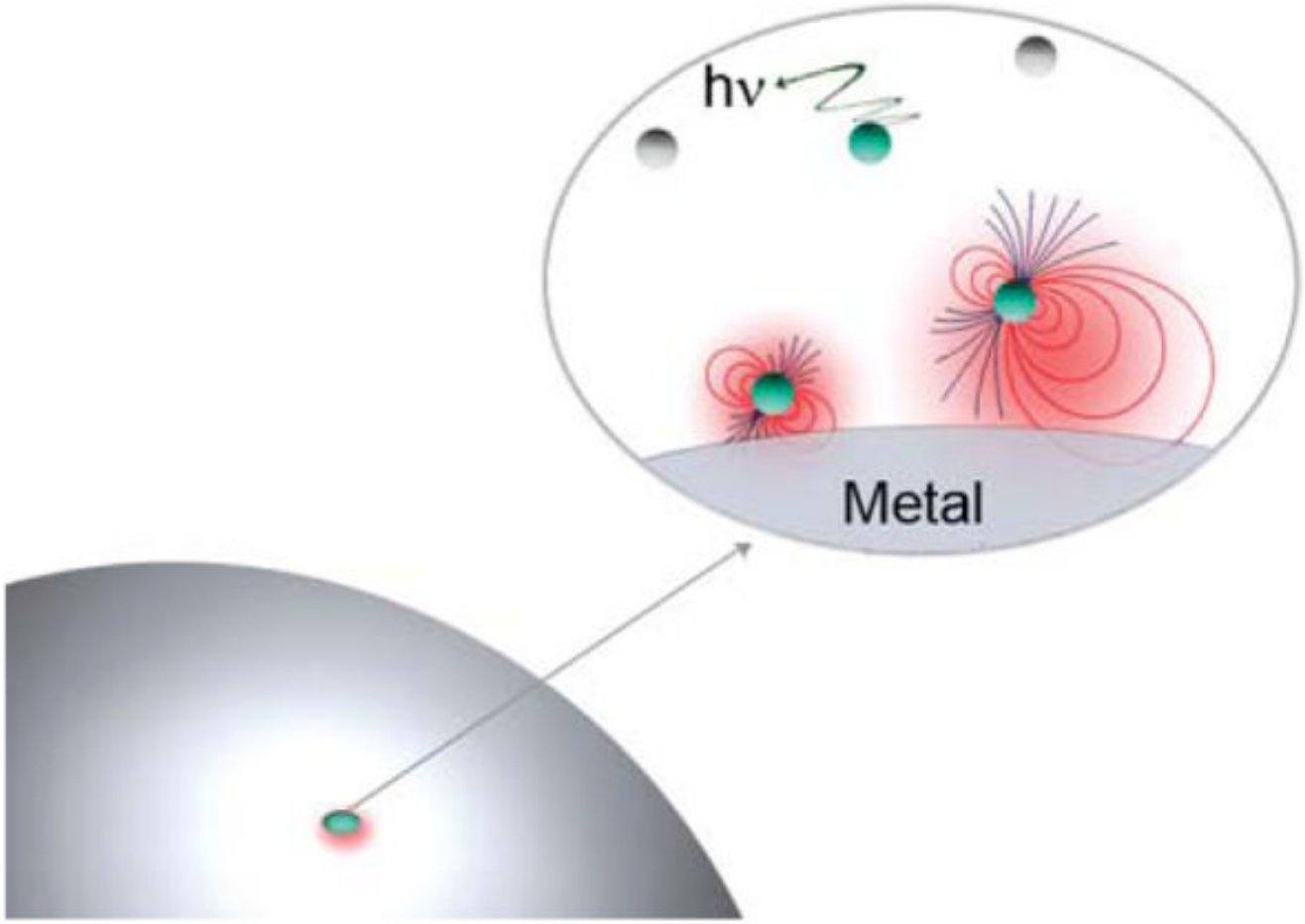

Fig. 4.
Fluorophore near a metallic surface.

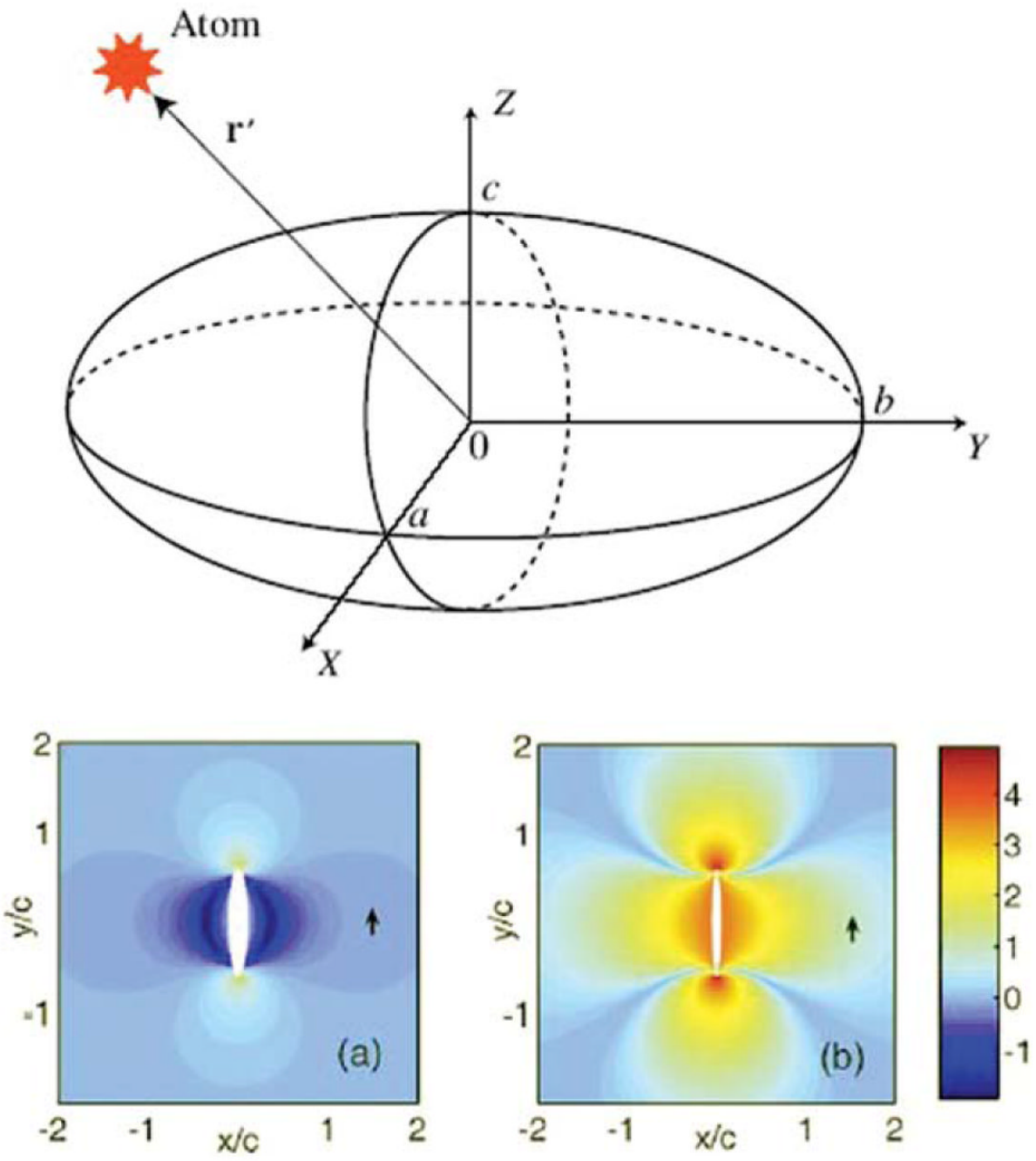

Fig. 5.

Radiative decay rates for a fluorophore near a metal colloid. Top: geometry of the colloid. Bottom: relative radiative decay rate of an atomic dipole with orientation of the moment along the *y*-axis and placed near a silver nanoellipsoid [$\varepsilon = -15{,}37 + i0{,}231$ ($\lambda = 632.8$ nm)] as a function of the atom's position in the $x = 0$ plane: (a) $b/c = 0.6$, $a/c = 0.105$; (b) $b/c = 0.6$, $a/c = 0.046$. The arrow indicates the orientation of the dipole momentum. Bar is in the logarithmic scale. (Reprinted with permission from ref. [22]. Copyright 2005, Elsevier.)

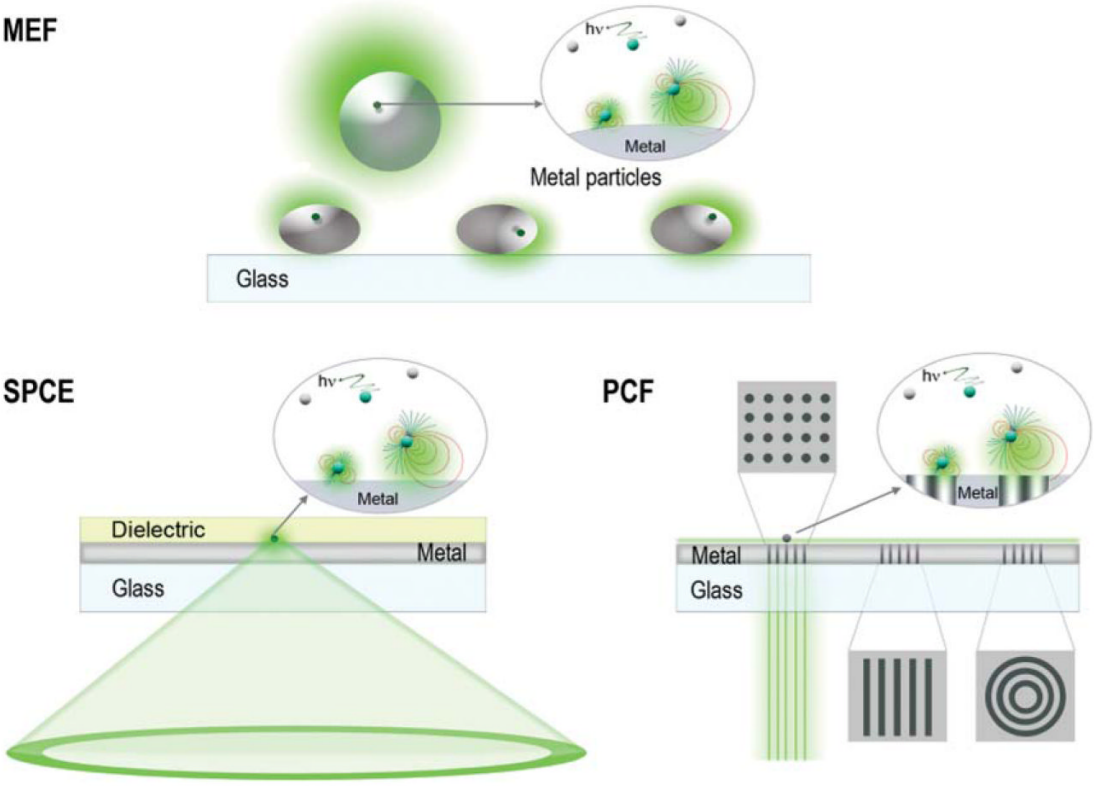

Fig. 6.
Schematic of MEF, SPCE, and PCF.

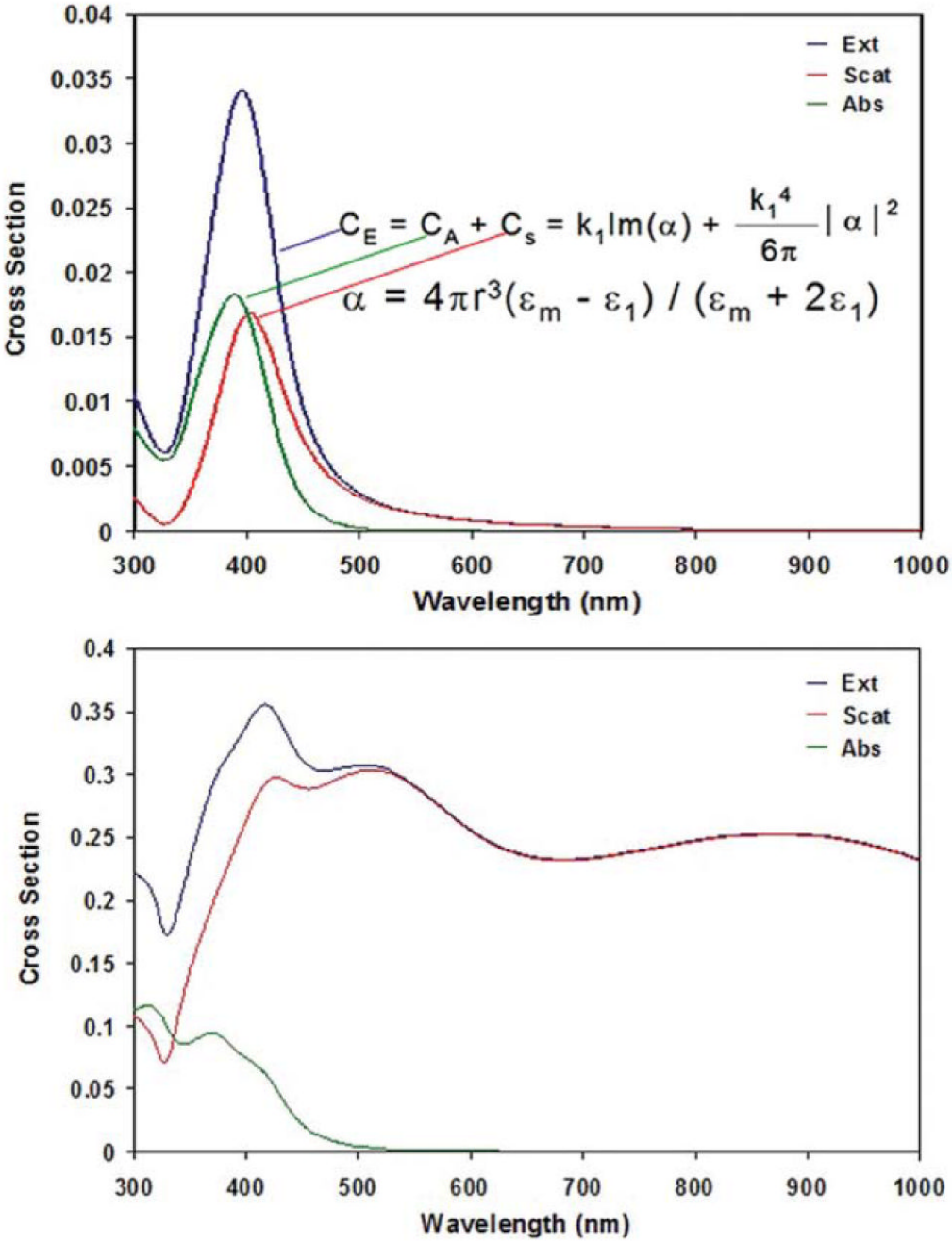

Fig. 7.

Extinction, scattering and absorption cross-section of 80 nm Ag colloid (top) and 320 nm Ag colloid (bottom) calculated using Mie theory.

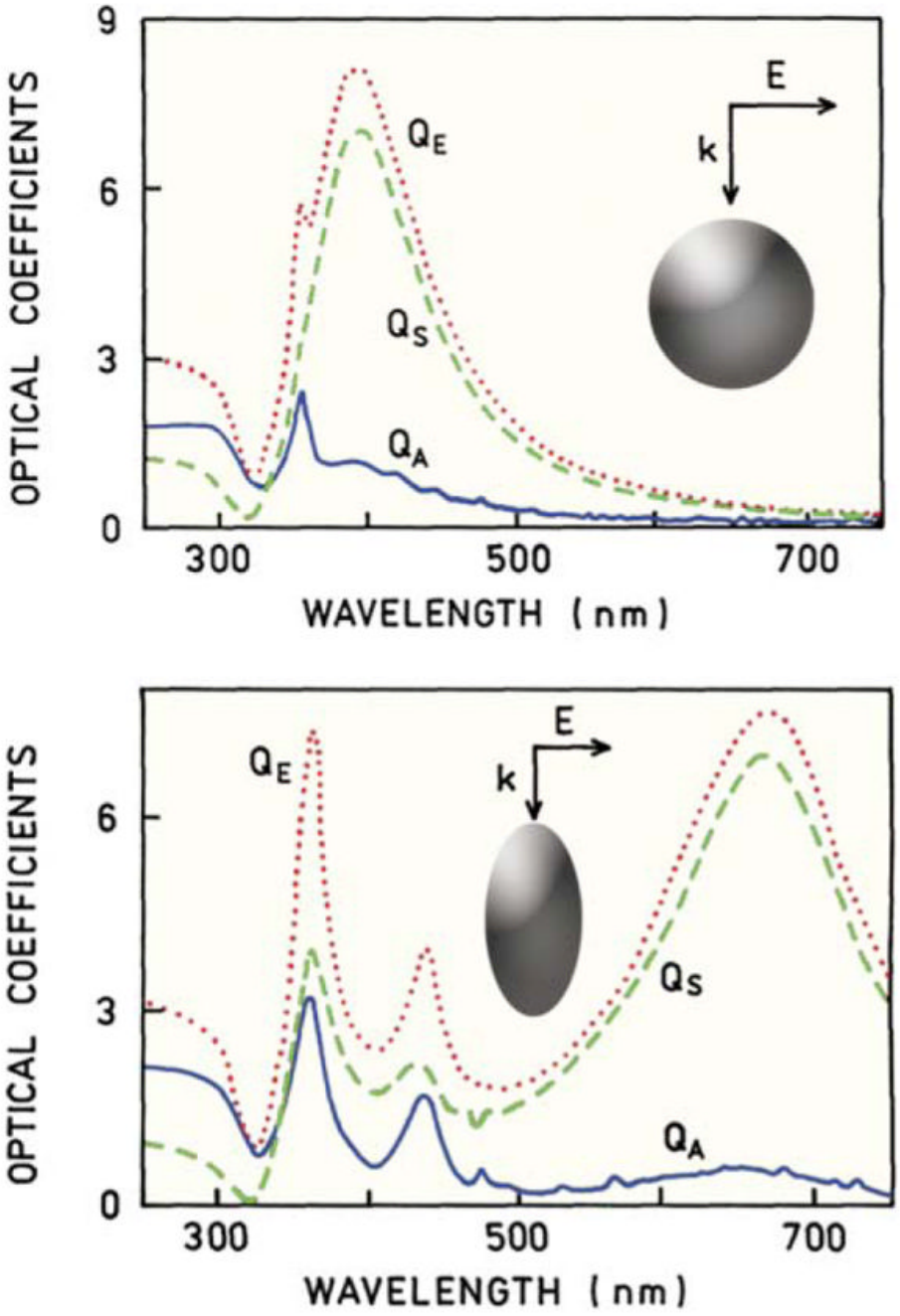

Fig. 8.

Optical spectra of silver particles calculated using the DDA. For the sphere the radius is 50 nm. The ellipse area was the same as the sphere. The axial ratio was 3 to 1. (Reprinted with permission from ref. [36]. Copyright 2003, American Chemical Society.)

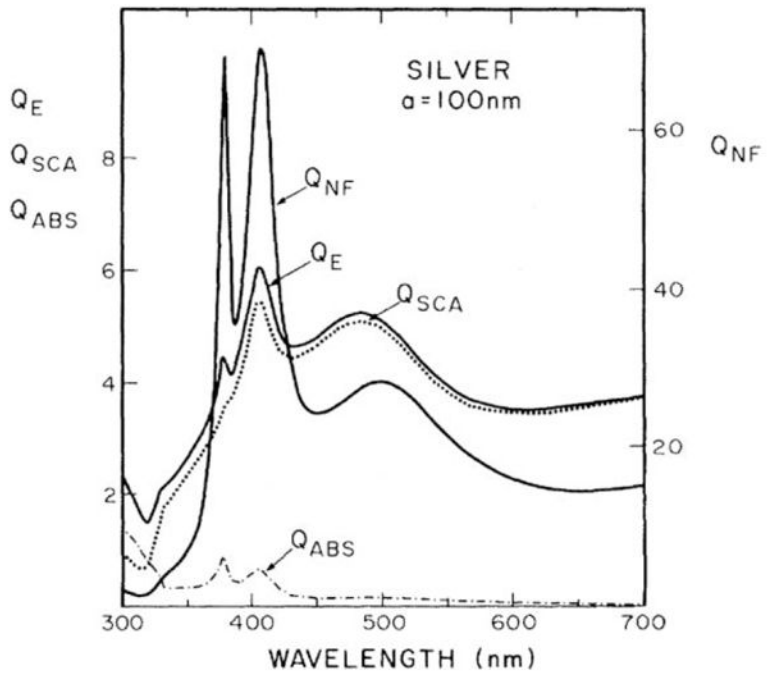

Fig. 9.

Extinction, far-field scattering, and absorption efficiency (scale on the left side) compared with the near-field scattering efficiency (scale on the right side) for spheres with a = 100 nm immersed in water. (Reprinted with permission from ref. [41]. Copyright 1981, American Physical Society.)

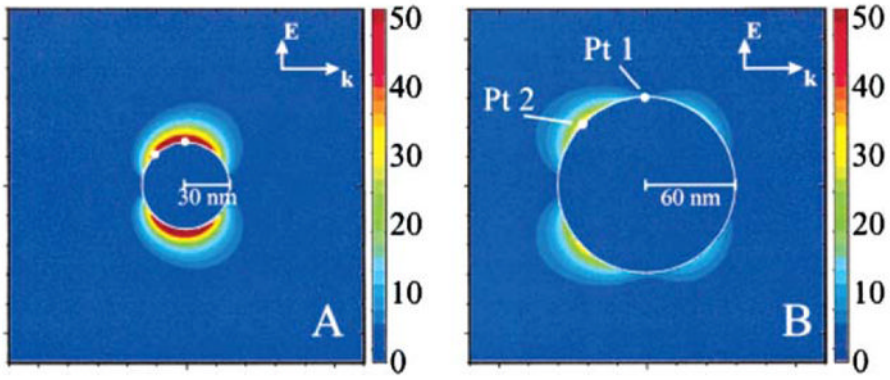

Fig. 10.

Total electric field intensity near 60 nm (left) and 120 nm (right) diameter colloids calculated by the DDA method.[35] The light is propagating from left to right. (Reprinted with permission from ref. [35]. Copyright 2003, American Chemical Society.)

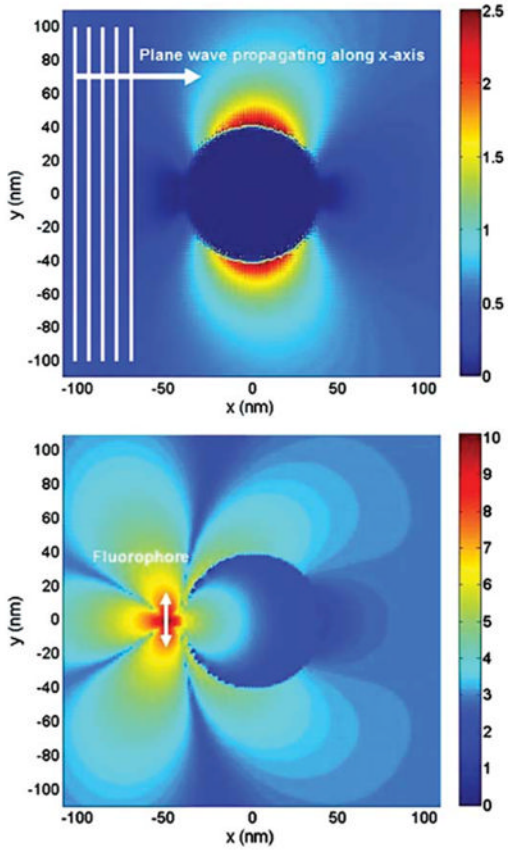

Fig. 11.

Interaction of incident light with a colloid. Our FDTD calculations of the electric field around a 80 nm diameter silver colloid with 580 nm plane-wave illumination (top). Interaction of a 620 nm dipole fluorophore with a 80 nm colloid (bottom).

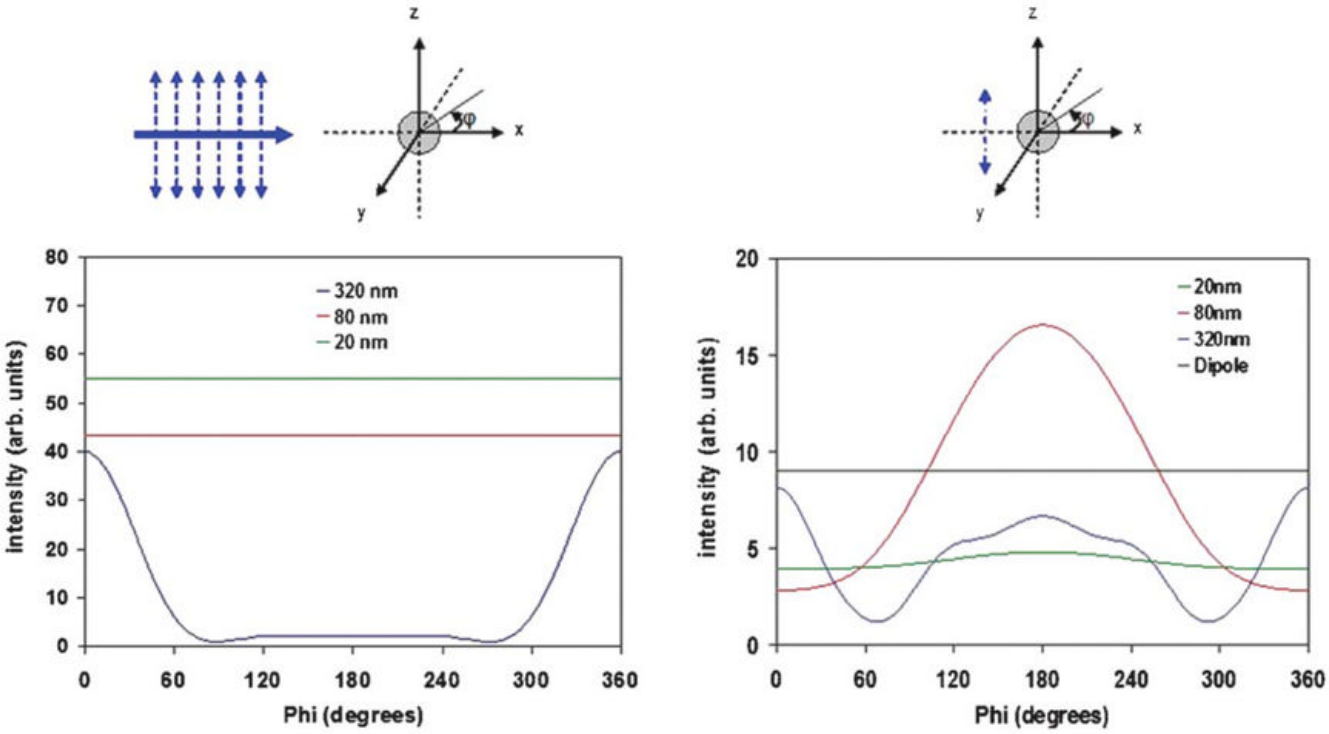

Fig. 12.

FDTD calculations of the *x–y* plane spatial distribution of light from silver nanoparticles with vertically polarized plane-wave illumination (left) and for a vertically oriented oscillating dipole near silver nanoparticles (right). The incident and dipole wavelengths are both 420 nm. (Reprinted with permission from ref. [9]. Copyright 2007, Optical Society of America.)

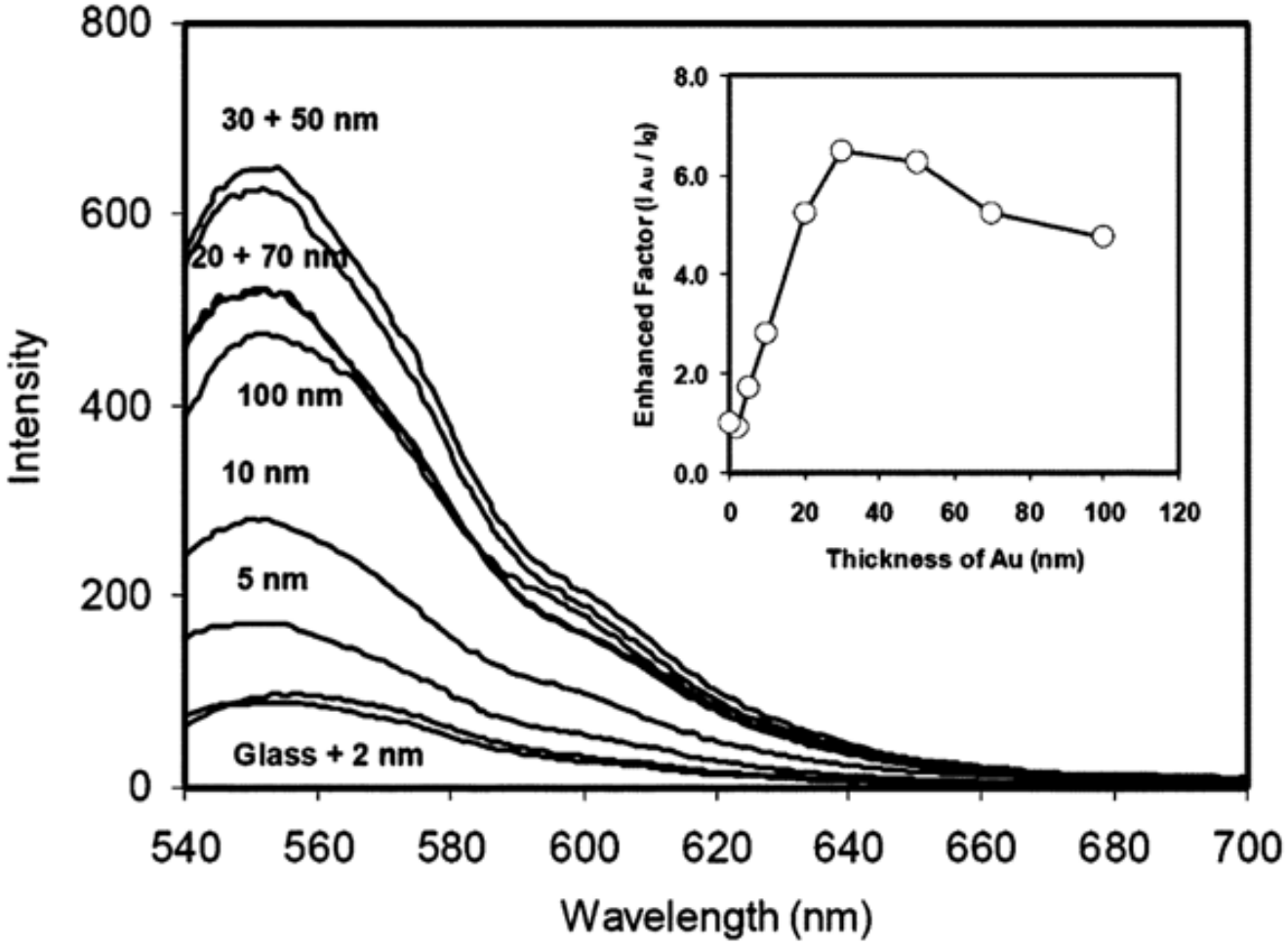

Fig. 13.

Emission spectra of Alexa Fluor 555®-labeled anti-rabbit IgG on varying thickness gold films upon excitation at 514 nm. The inset represents the dependence of the enhancement factor on the thickness of the gold film. The intensities and spectra are similar for 20 and 70 nm thick gold and for 30 and 50 nm thick gold. All gold films were coated by 5 nm silica. (Reprinted with permission from ref. [70]. Copyright 2007, Optical Society of America.)

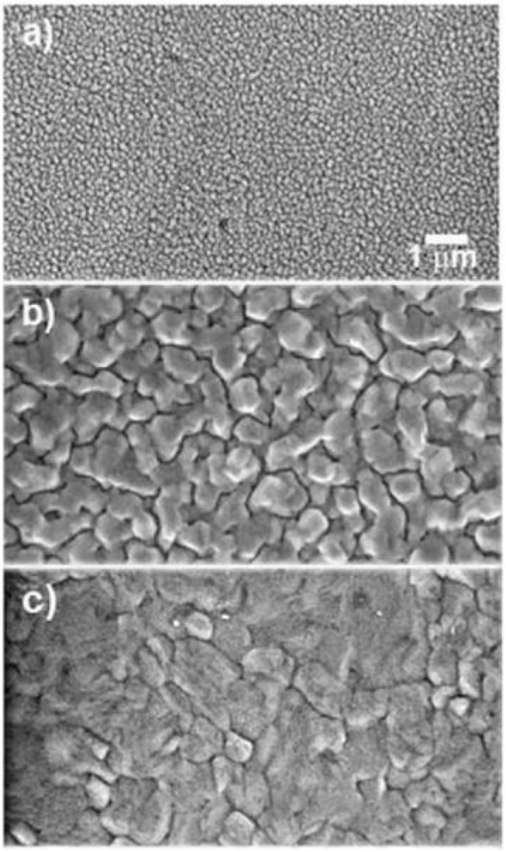

Fig. 14.
SEM images of evaporated Al films: (a) 2 nm, (b) 10 nm, and (c) 80 nm. (Reprinted with permission from ref. [72]. Copyright 2007, American Chemical Society.)

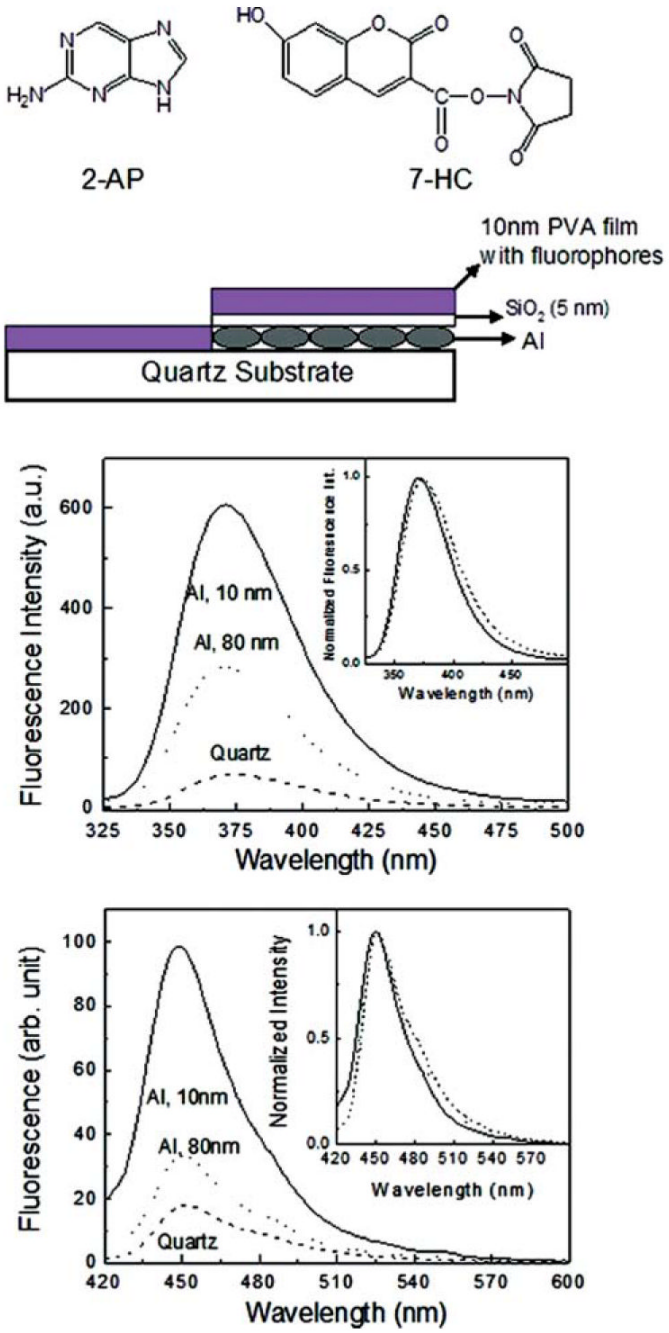

Fig. 15.

Emission spectra of 2-AP and 7-HC on slides coated with aluminium particles. (Reprinted with permission from ref. [72]. Copyright 2007, American Chemical Society.)

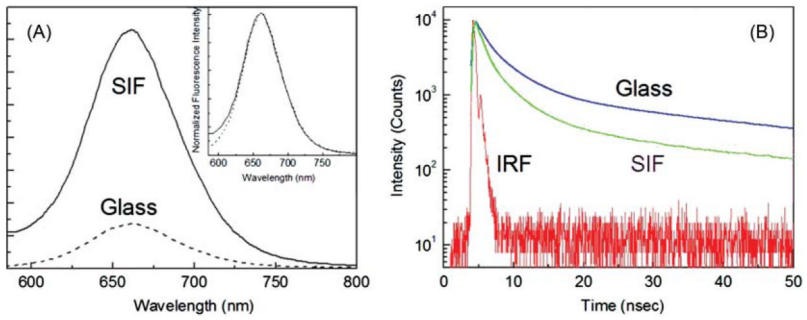

Fig. 16.

(A) Fluorescence spectra of CdTe on glass and SIF. Inset shows the normalized emission spectra. (B) Intensity time decay of CdTe on glass and SIF. The instrument response function (IRF) is also included. (Reprinted with permission from ref. [75]. Copyright 2006, American Chemical Society.)

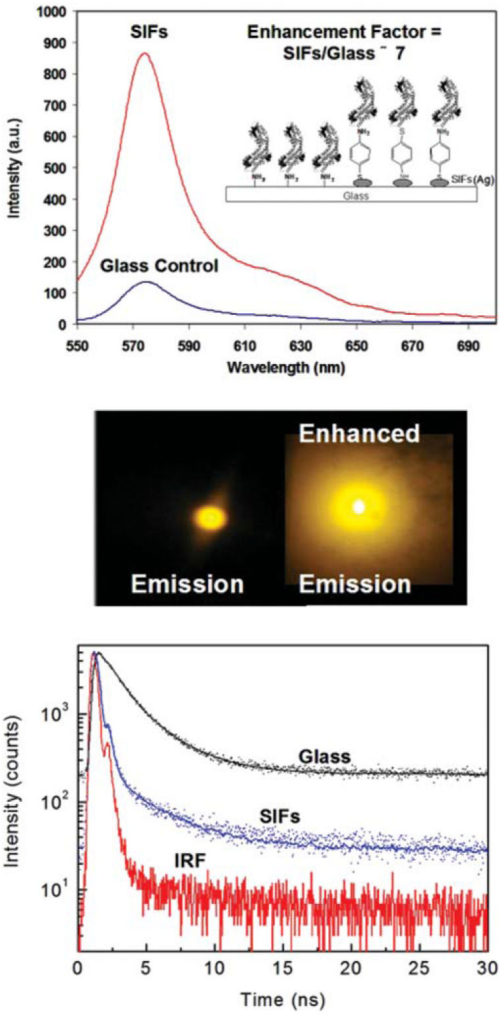

Fig. 17.

Emission spectra (top), lifetimes (bottom) and photograph of phycoerythrin (middle), on glass and silver island films. The instrument response function (IRF) is also included (bottom). (Reprinted with permission from ref. [78]. Copyright 2007, American Chemical Society.)

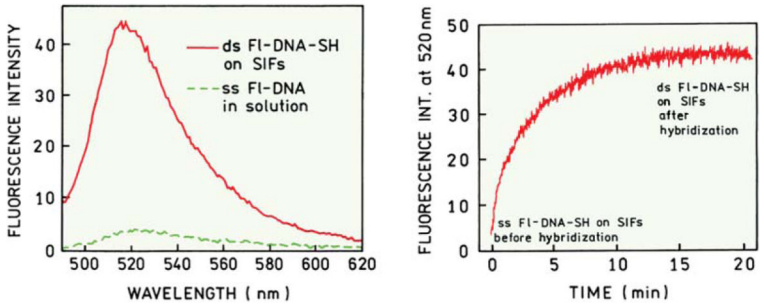

Fig. 18.

Emission spectra and time-dependent intensity of a fluorescein-labeled oligomer upon binding to a complementary oligomer bound exclusively to an SIF. (Reprinted from ref. [85]. Copyright 2003, with permission from Elsevier.)

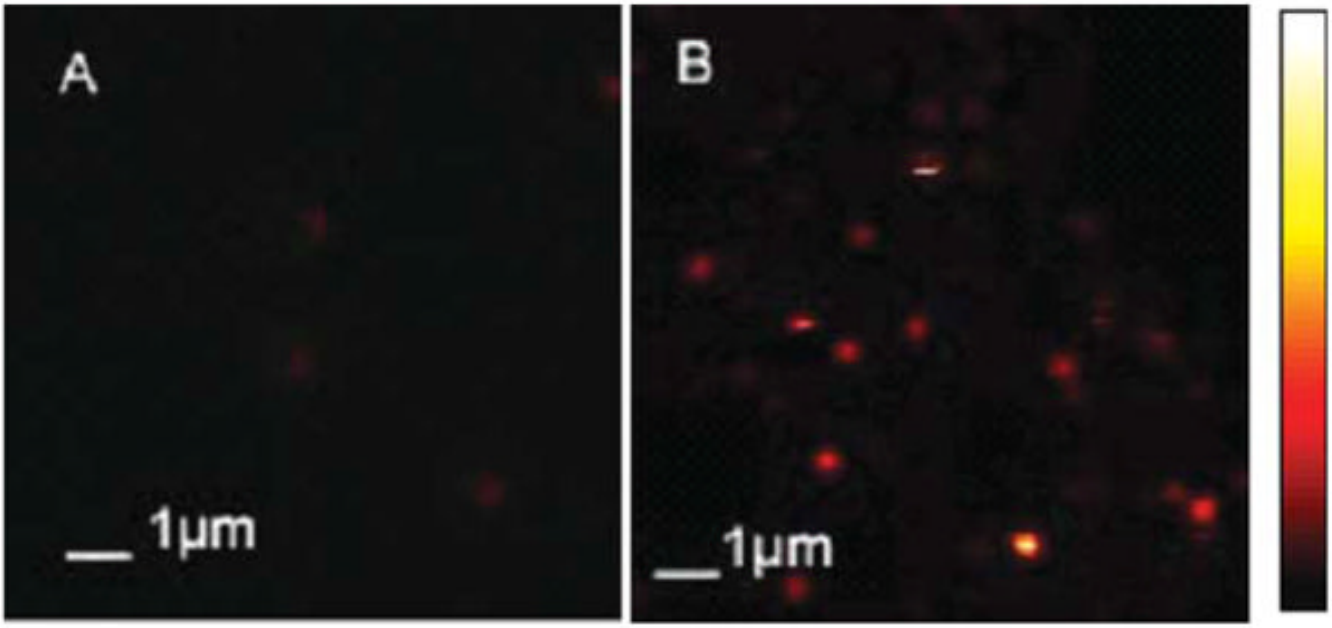

Fig. 19.

Single molecule fluorescence images of Cy5-DNA on glass (left) and on a SIF (right). On SIF the Cy5-DNA is separated from the silver surface by a layer of BSA-biotin/avidin. The laser intensities on the left (*ca.* 700 nW) and right (*ca.* 30 nW), the incident intensity is 23-fold less for the SIF. (Reprinted with permission from ref. [88]. Copyright 2006, American Chemical Society.)

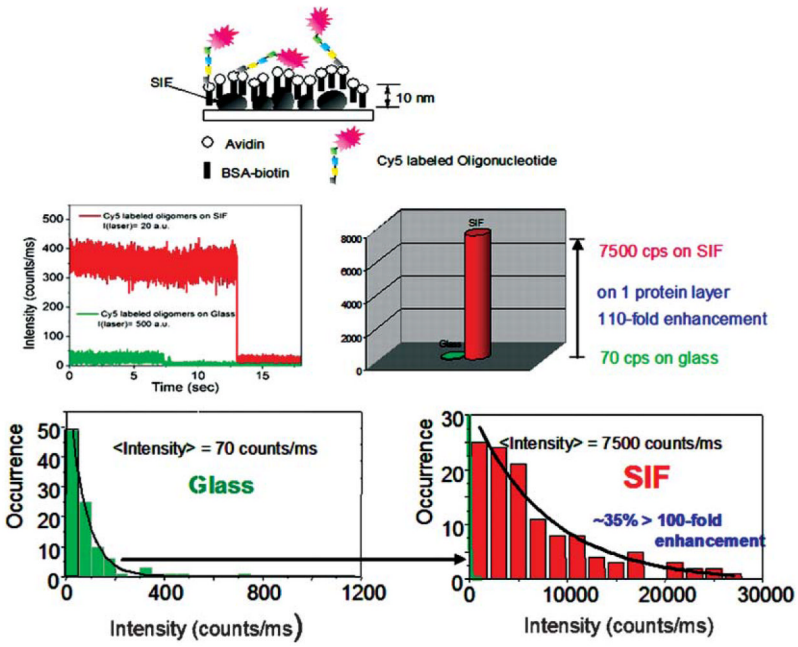

Fig. 20.

Top: single molecule Cy5-DNA fluorescence separated from the metal by 10 nm. Note the incident intensity is 25-fold less for the silver particles. Bottom: intensity histograms for over 100 Cy5-DNA molecules. (Reprinted with permission from ref. [88]. Copyright 2006, American Chemical Society.)

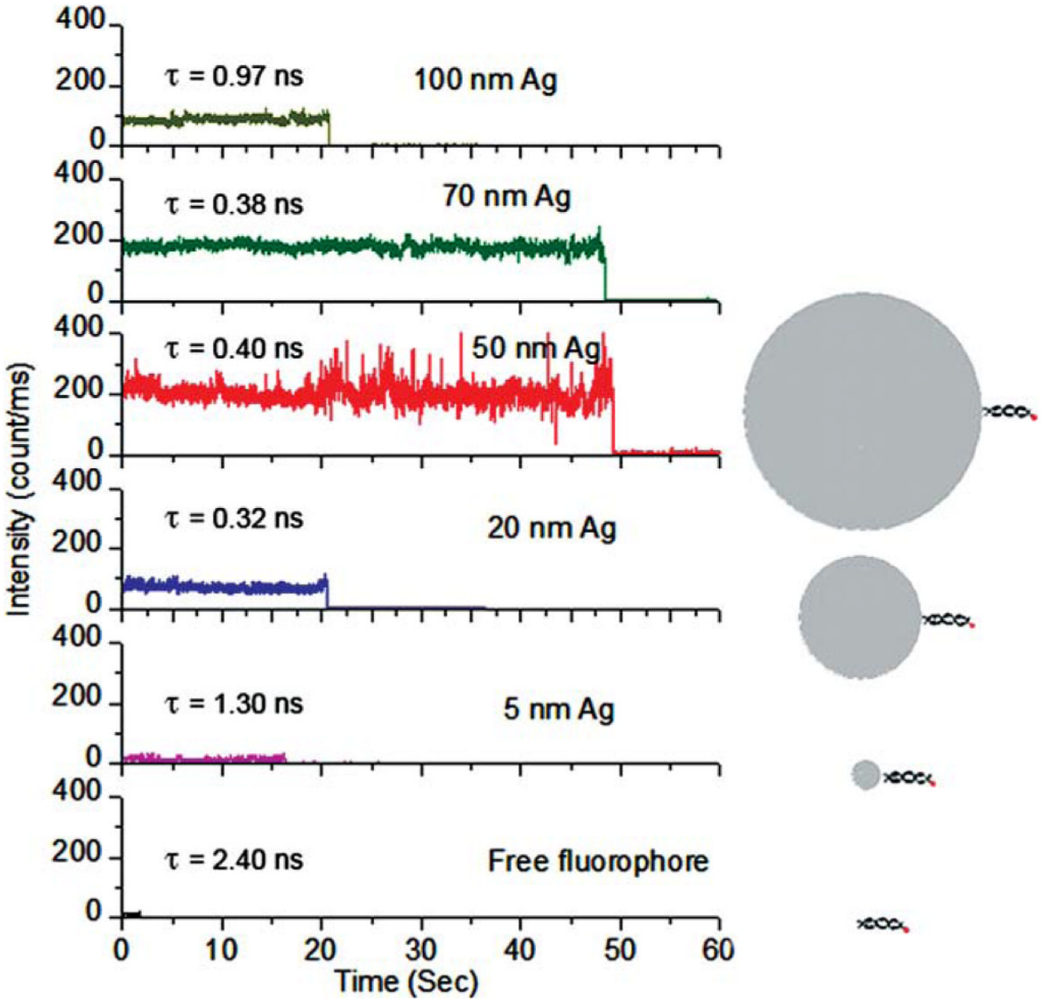

Fig. 21.

Effects of silver particle size on single molecules of Cy5-DNA. Thiolated DNA was used to bind to the colloids. (Reprinted with permission from ref. [89]. Copyright 2008, American Chemical Society.)

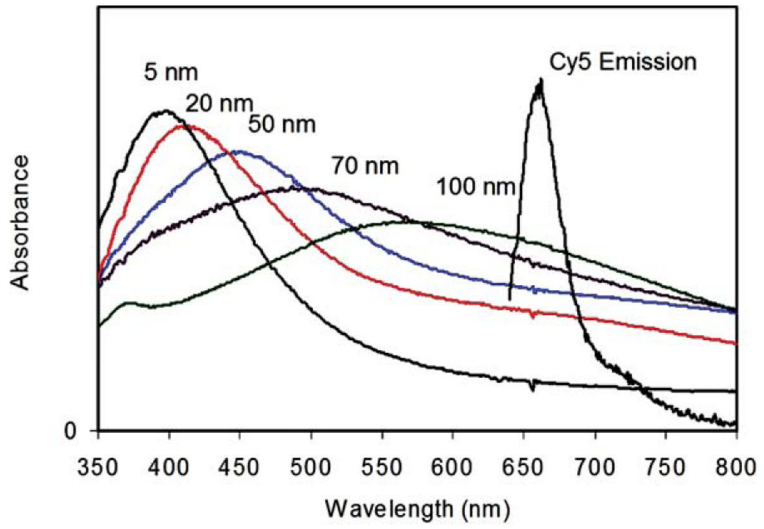

Fig. 22.

Emission spectra of Cy5 and extinction spectra of various size silver colloids. (Reprinted with permission from ref. [89]. Copyright 2008, American Chemical Society.)

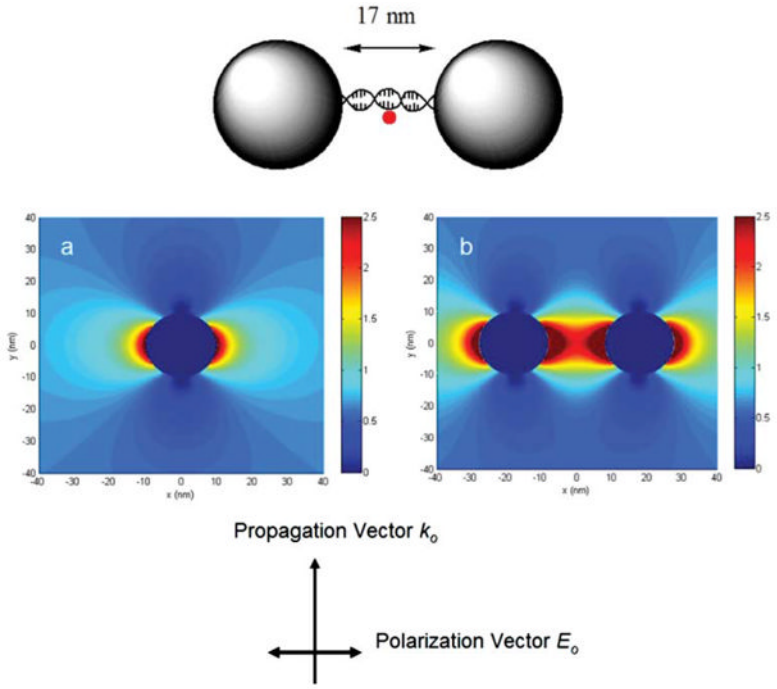

Fig. 23.

Schematic of Cy5-DNA localized between two silver colloids and the local fields induced by incident light from FDTD calculations. (Reprinted with permission from ref. [92]. Copyright 2007, American Chemical Society.)

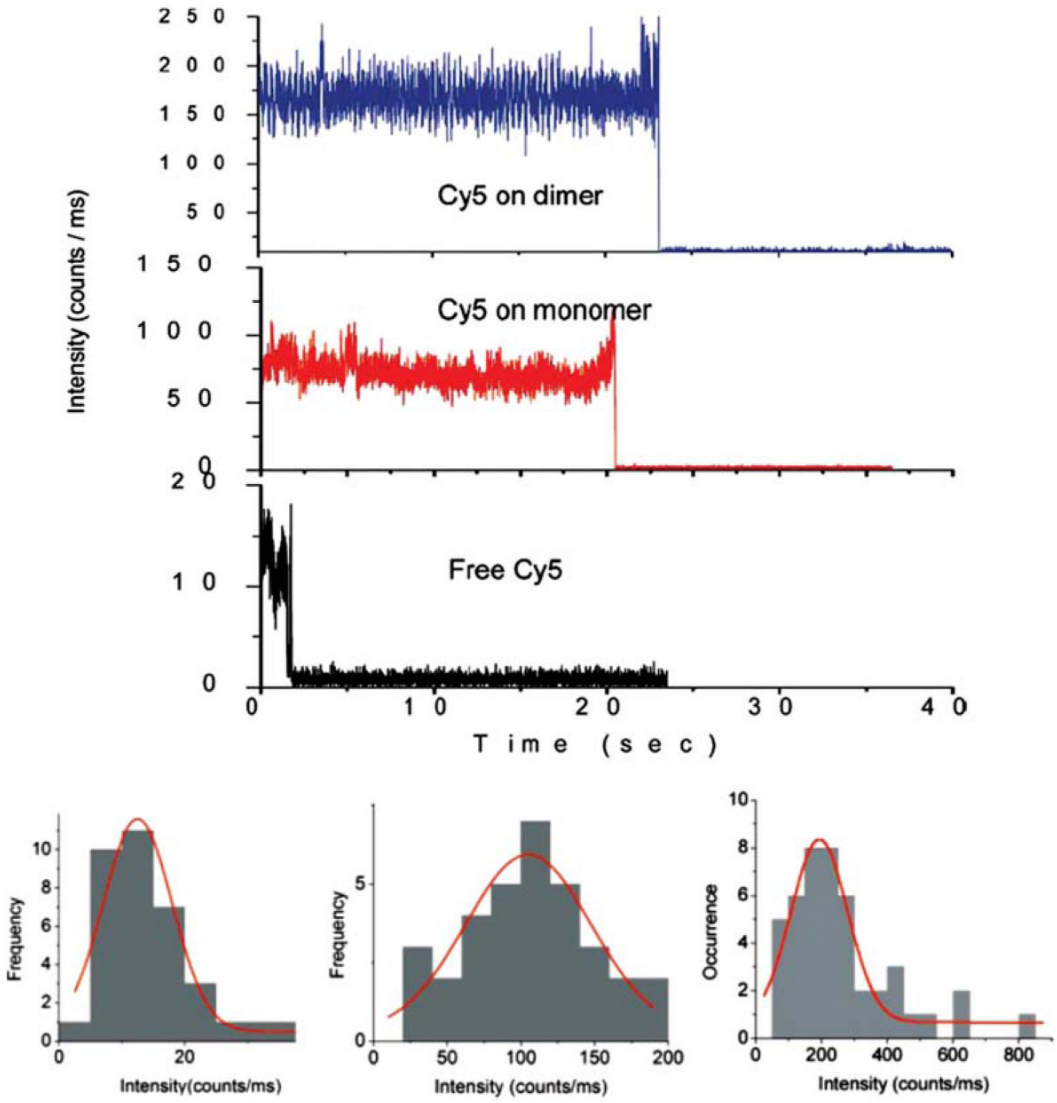

Fig. 24.

Intensity traces and histograms for Cy5-DNA on a silver colloid dimer, bound to a single silver particle and without a silver particle. The lower panels show intensity histograms from a large number of individual Cy5 molecules. (Reprinted with permission from ref. [92]. Copyright 2007, American Chemical Society.)

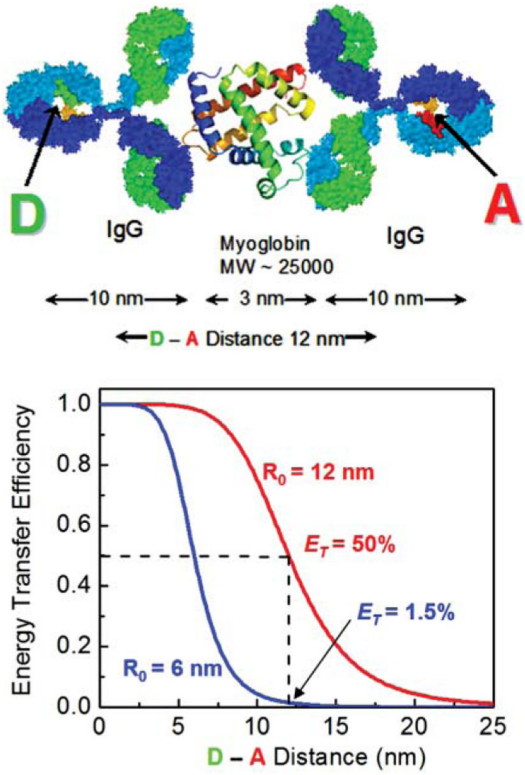

Fig. 25.

Schematic of energy transfer in a sandwich assay with a change in R_0. For this D–A pair the transfer efficiency is near 50% for the metal-enhanced R_0 = 12 nm and only 1.5% for R_0 = 6 nm without a metal particle.

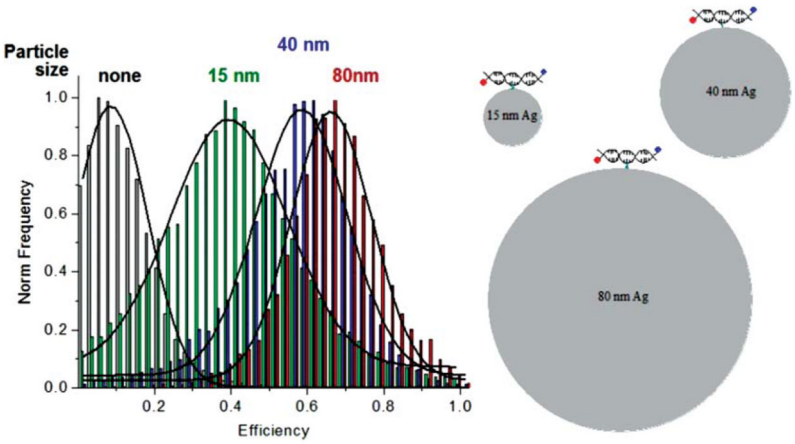

Fig. 26.
Effects of silver particle size on FRET. (Reprinted with permission from ref. [102]. Copyright 2007, American Chemical Society.)

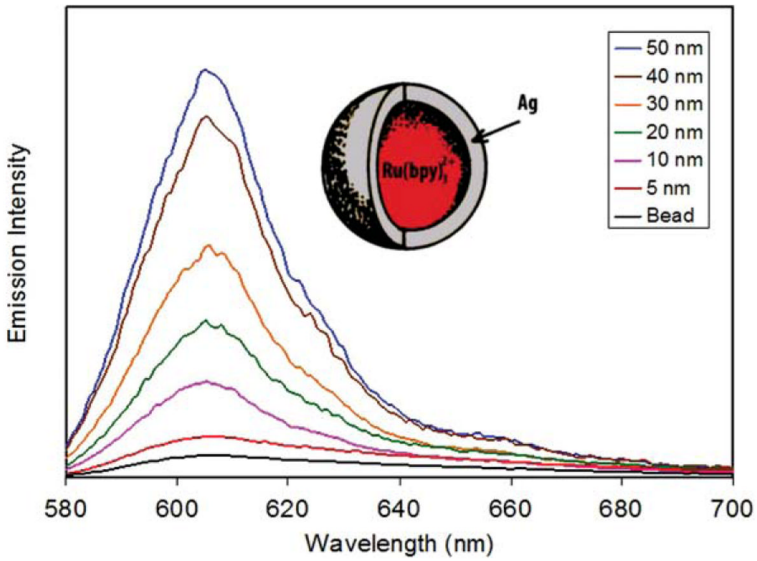

Fig. 27.

Emission spectra of a silica bead containing $Ru(bpy)_3^{2+}$ alone and coated with an increasing thickness of a silver shell. (Reprinted with permission from ref. [105]. Copyright 2006, American Chemical Society.)

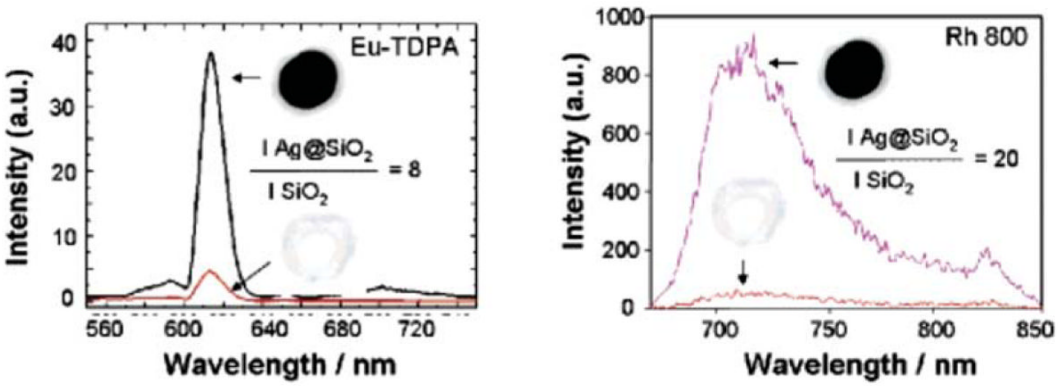

Fig. 28.

Fluorescence emission intensity of Eu-TDPA-doped $Ag@SiO_2$ and Rh880-doped $Ag@SiO_2$, and from the corresponding fluorescent nanobubbles with silver removed (control samples), Eu-TDPA-doped SiO_2 and Rh800-doped SiO_2. The diameter of the Ag is 130 ± 10 nm and the thickness of the shell is 11 ± 1 nm. (Reprinted with permission from ref. [107]. Copyright 2007, American Chemical Society.)

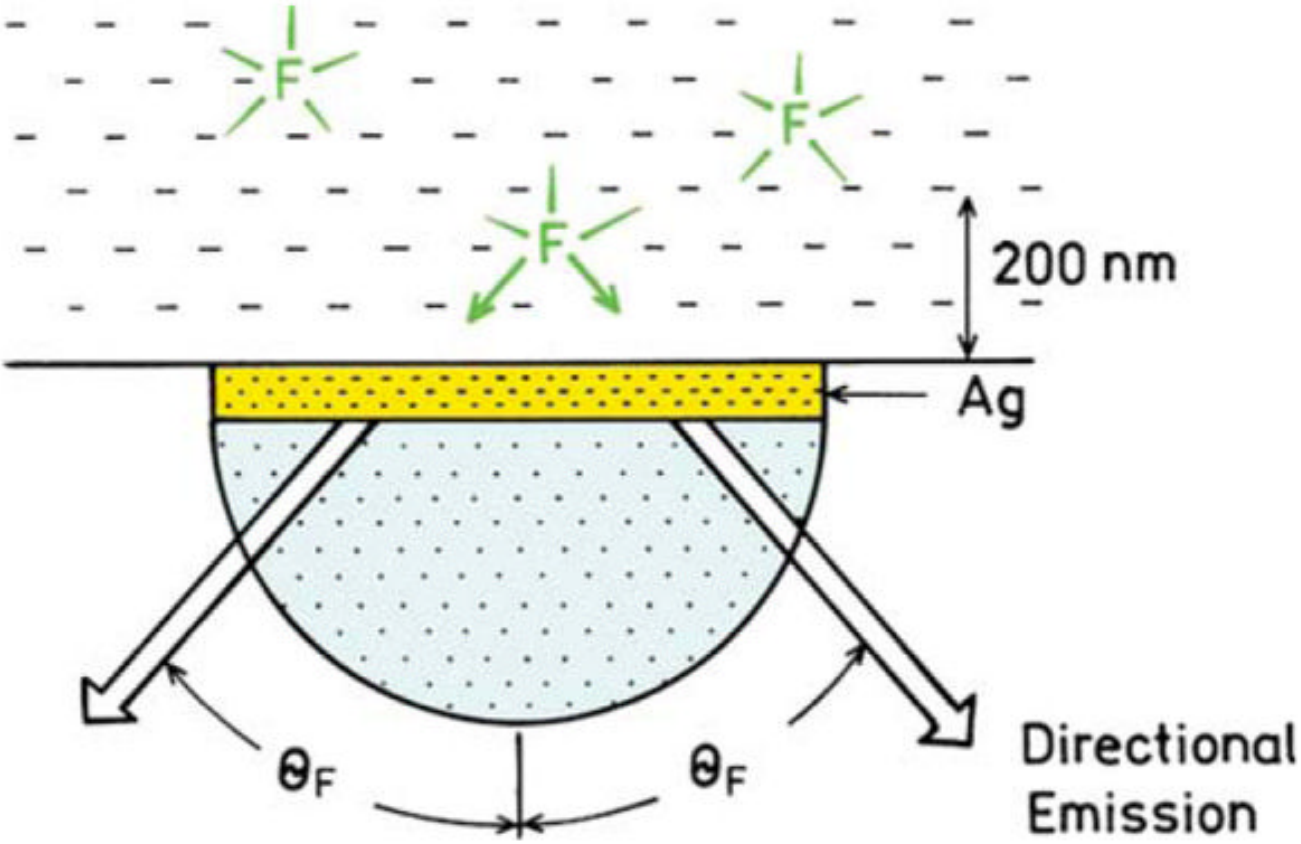

Fig. 29.
Surface plasmon-coupled emission. F is a fluorophore. (Reprinted with permission from ref. [111]. Copyright 2004, Elsevier.)

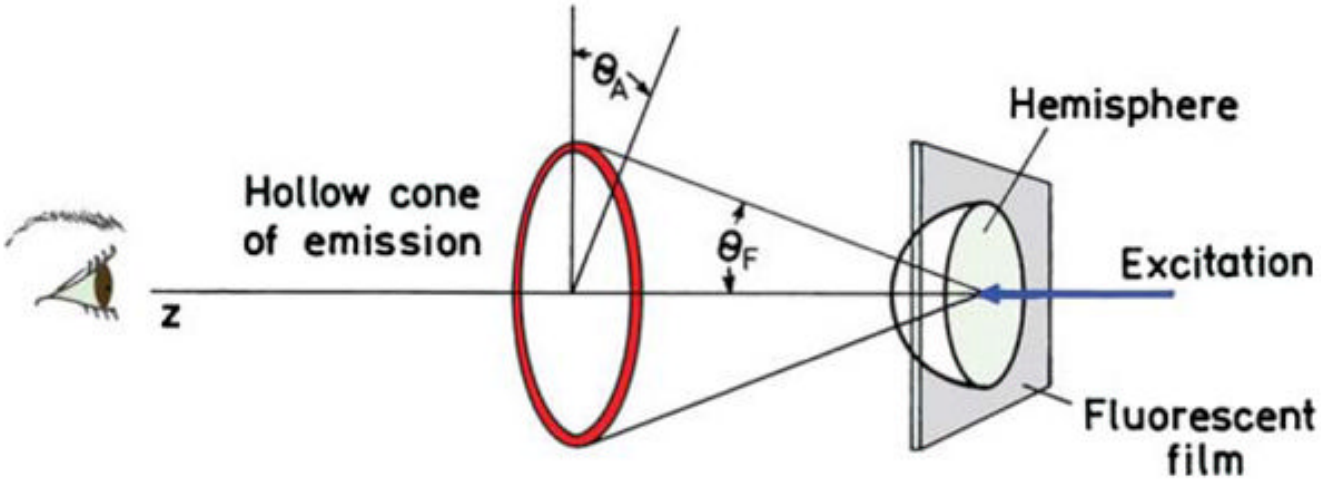

Fig. 30.
Surface plasmon-coupled cone of emission for fluorophores near a metallic film. (Reprinted with permission from ref. [111]. Copyright 2004, Elsevier.)

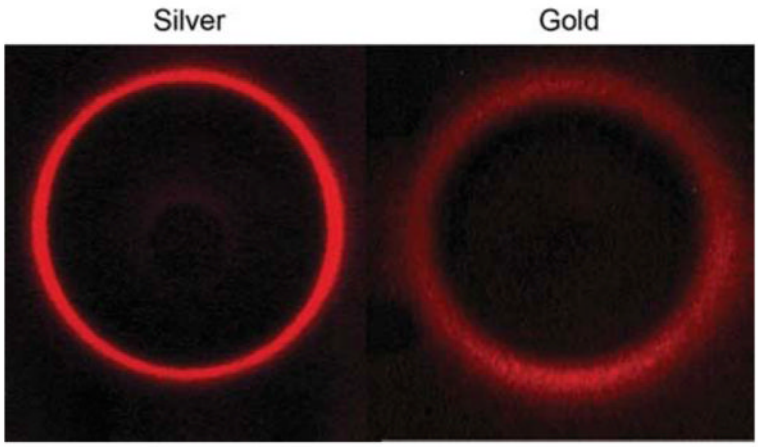

Fig. 31.
Cone of emission for S101 in PVA on silver and gold films.

Available online at www.sciencedirect.com
SCIENCE DIRECT®
Biochemical and Biophysical Research Communications 307 (2003) 435–439
BBRC
www.elsevier.com/locate/ybbrc

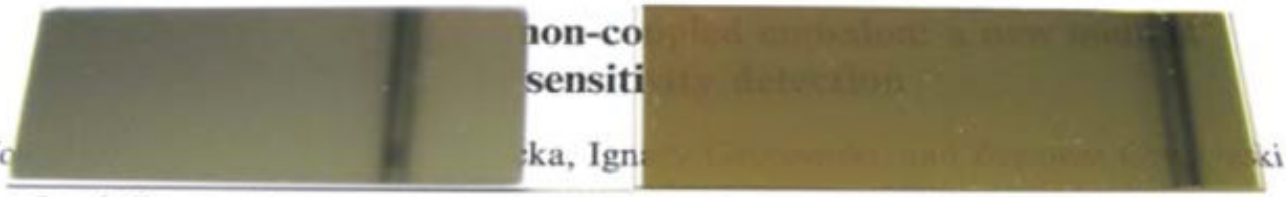

Center for Fluorescence Spectroscopy, University of Maryland at Baltimore, Department of Biochemistry and Molecular Biology, 725 West Lombard Street, Baltimore, MD 21201, USA

Received 29 May 2003

Fig. 32.
Photograph of silver (left) and gold films (right) used for SPCE.

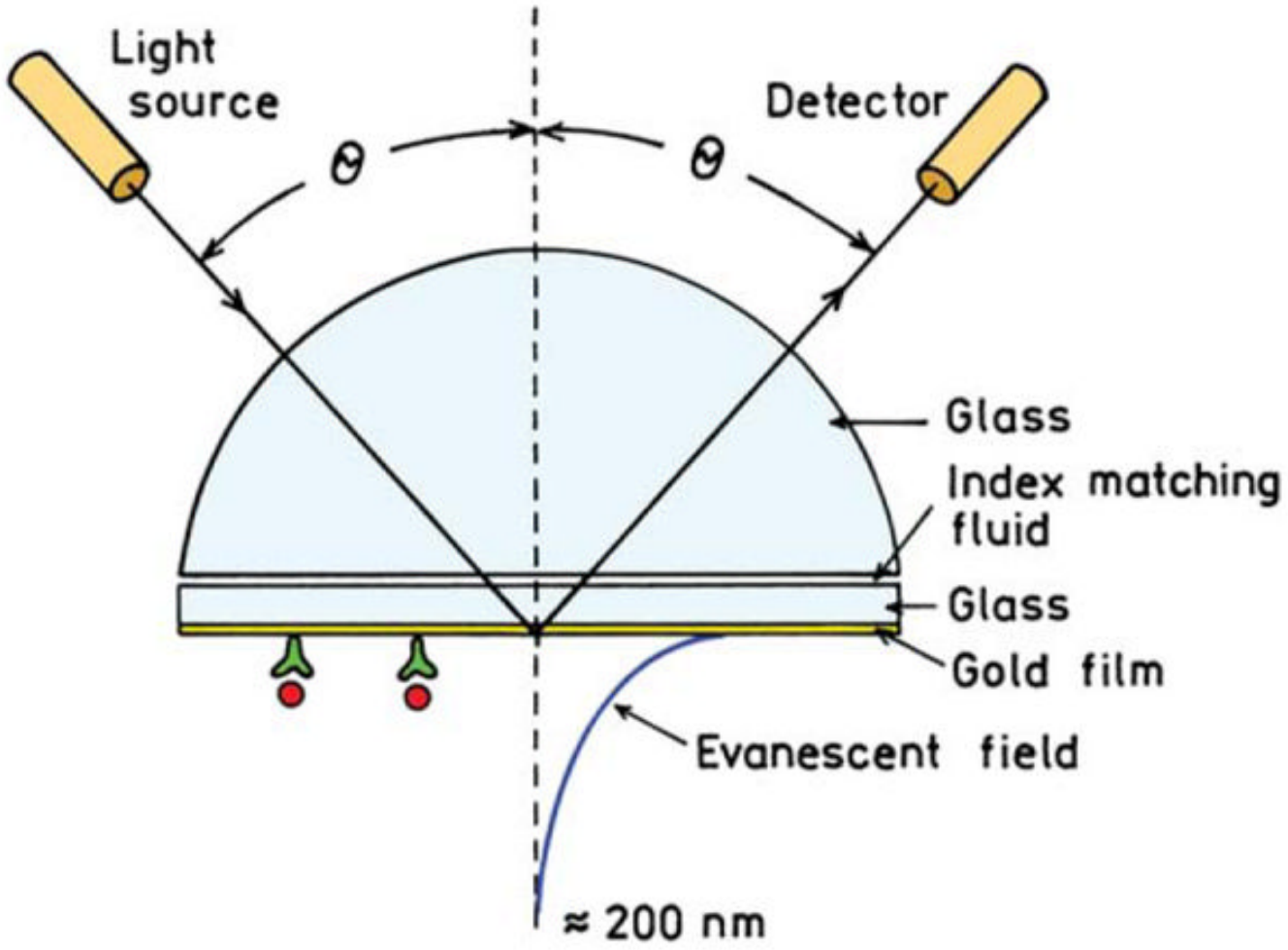

Fig. 33.
Typical configuration for surface plasmon resonance analysis. The incident beam is p-polarized.

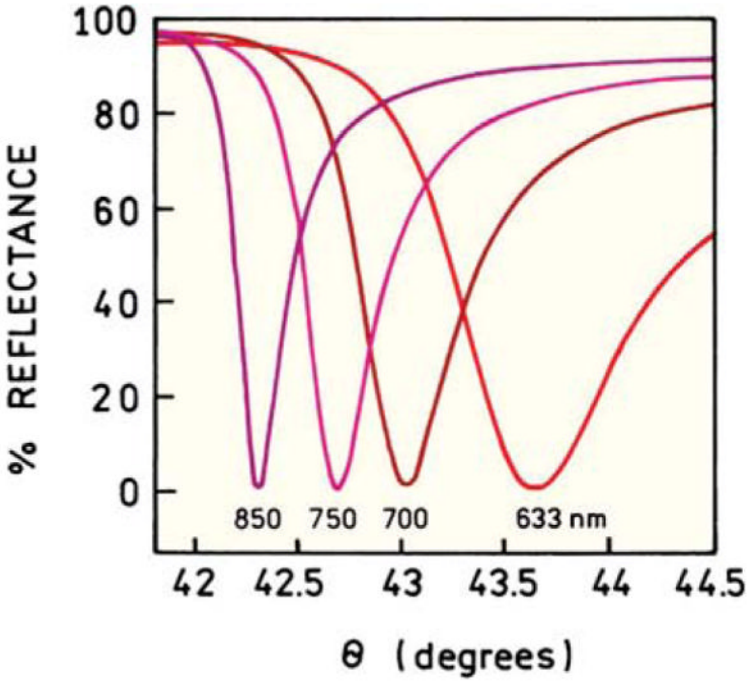

Fig. 34.
Calculated wavelength-dependent reflectivity for a 47 nm-thick gold film. (Reprinted with permission from ref. [111]. Copyright 2004, Elsevier.)

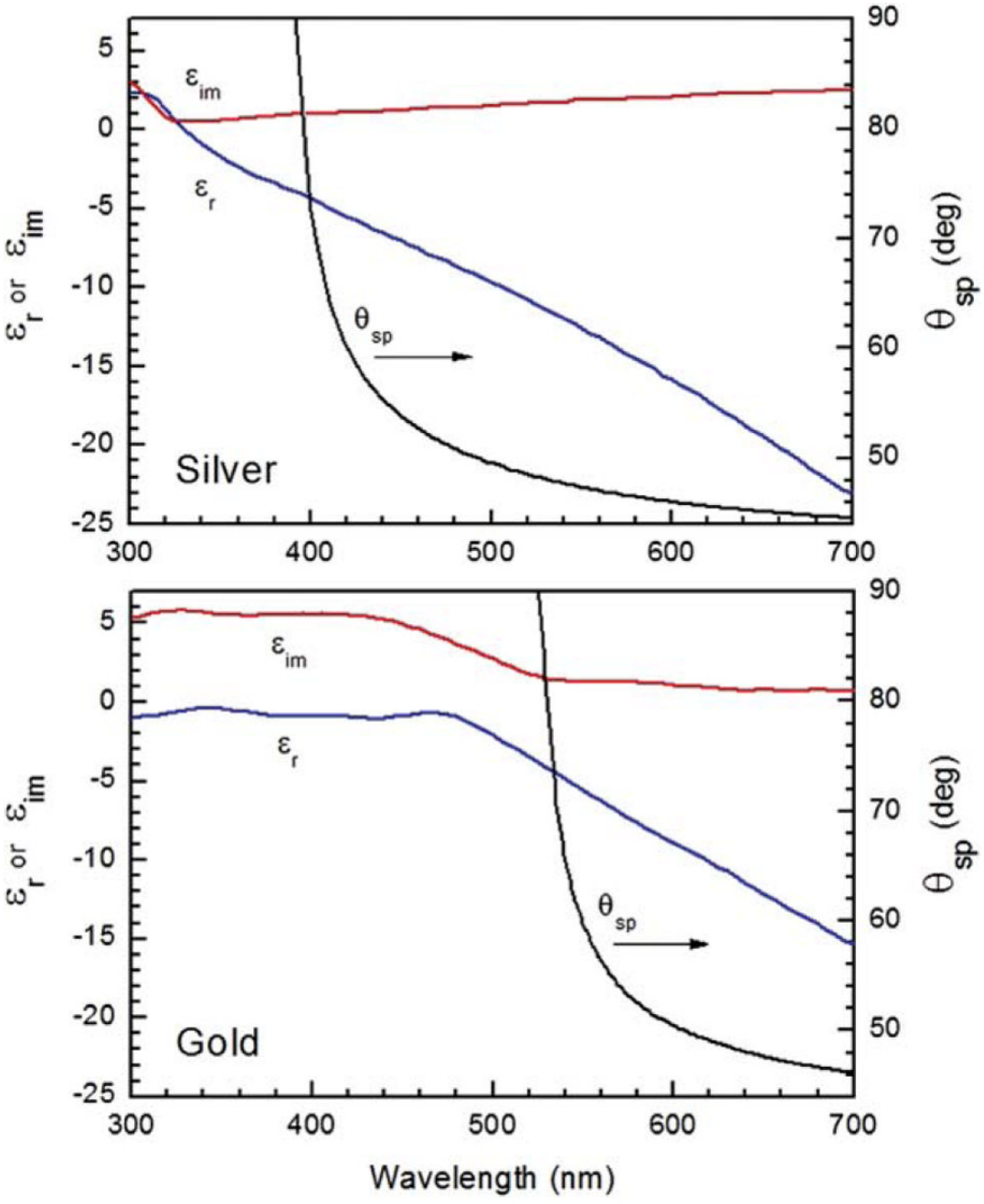

Fig. 35.
Complex dielectric constants for silver (top) and gold (bottom): ε_{im} (—), ε_r (—), θ_{SP} (—). (Reprinted with permission from ref. [111]. Copyright 2004, Elsevier.)

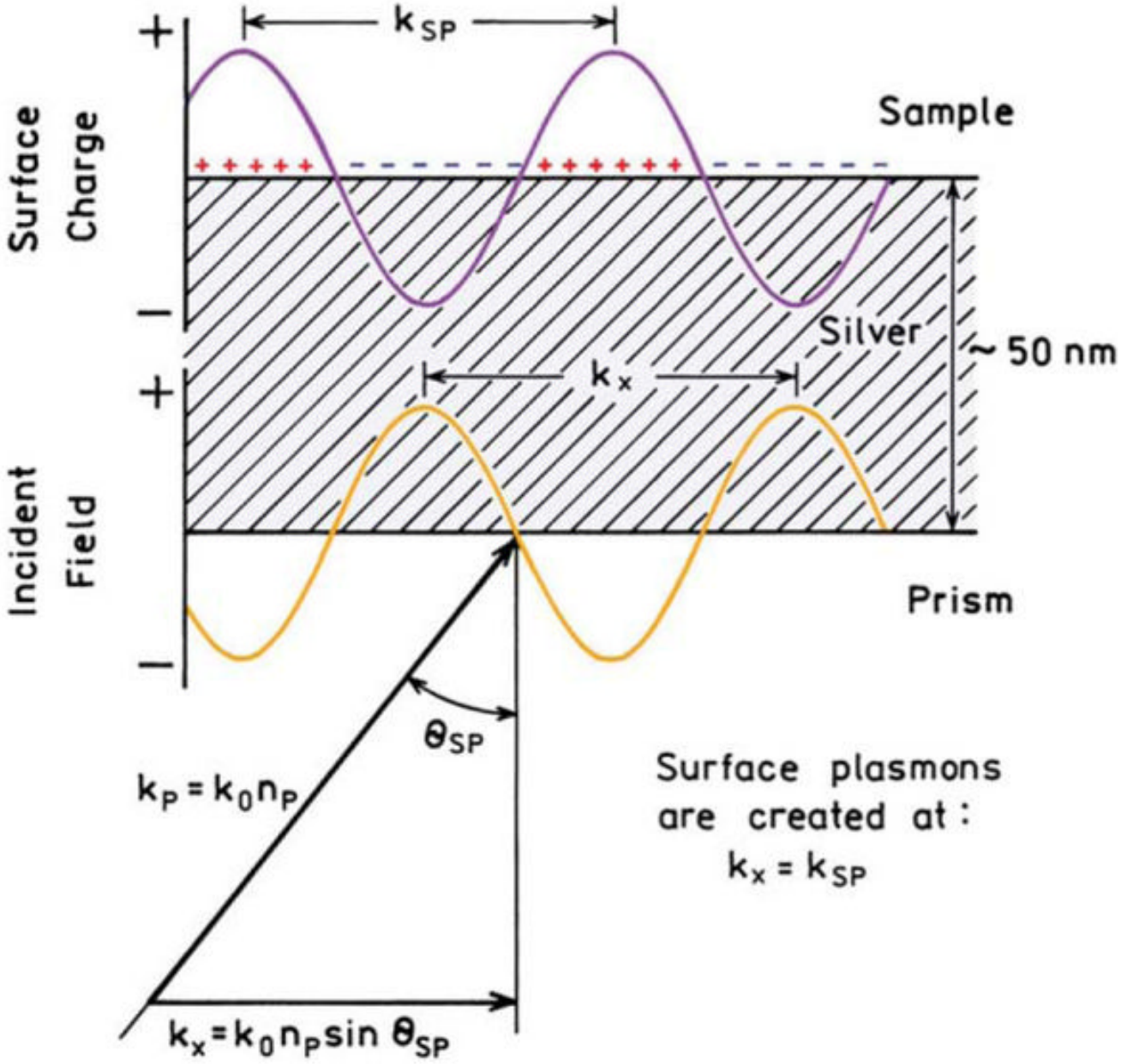

Fig. 36.
Schematic showing propagation constants in a prism and a thin silver film. (Reprinted with permission from ref. [111]. Copyright 2004, Elsevier.)

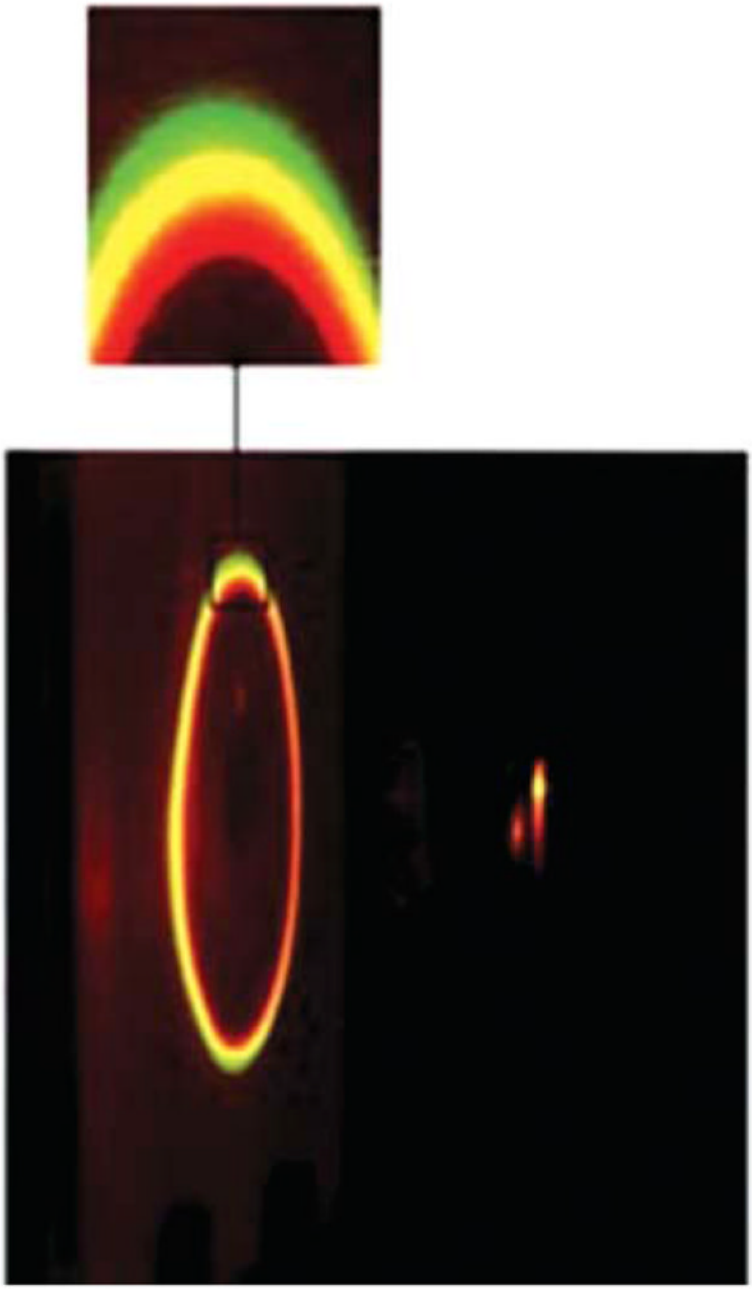

Fig. 37.
Photograph of SPCE from the mixture of fluorophores using RK excitation and a hemispherical prism, 532 nm excitation. (Reprinted with permission from ref. [112]. Copyright 2004, Elsevier.)

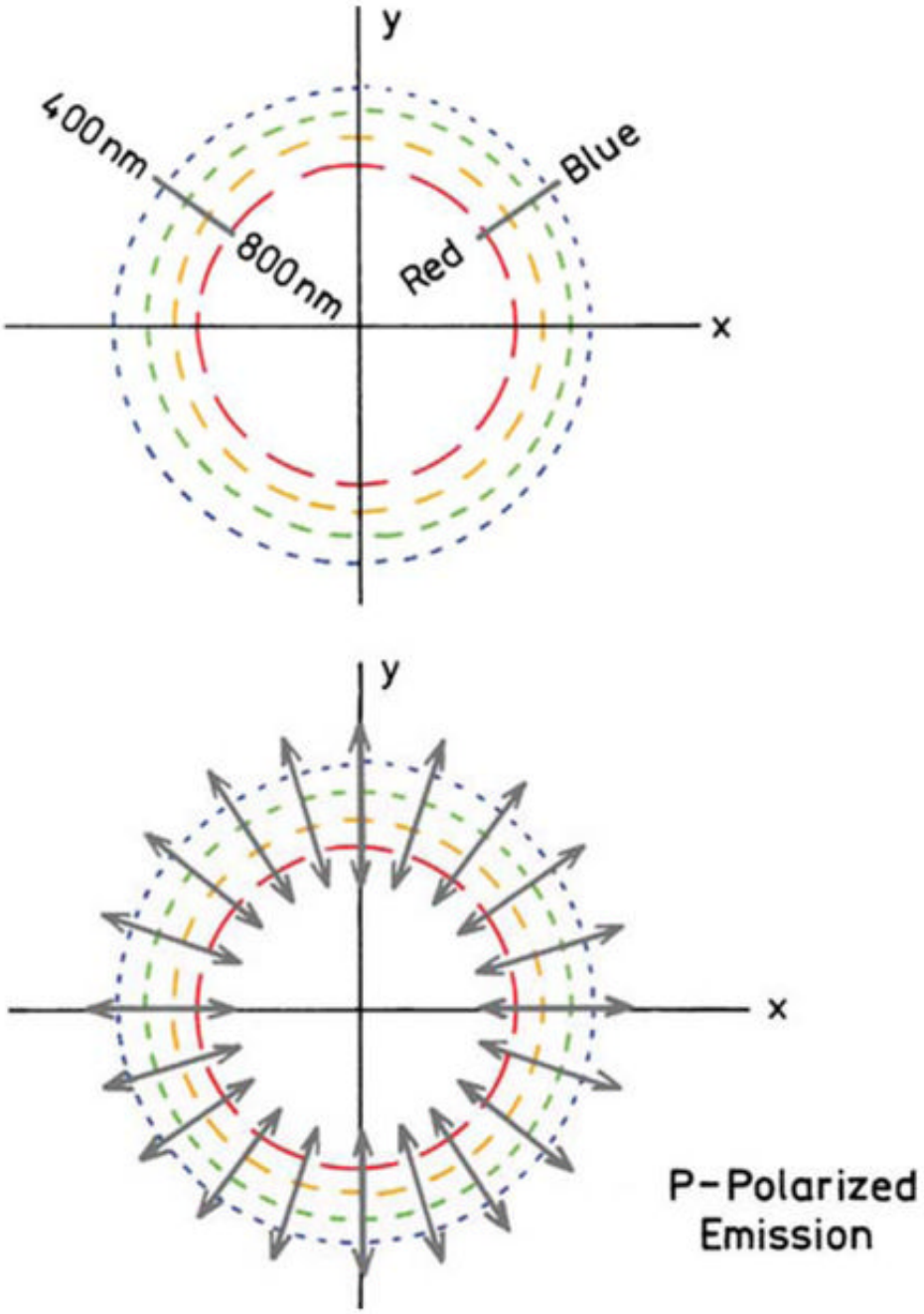

Fig. 38.
Color distribution and polarization expected for SPCE. (Reprinted with permission from ref. [111]. Copyright 2004, Elsevier.) metal film.

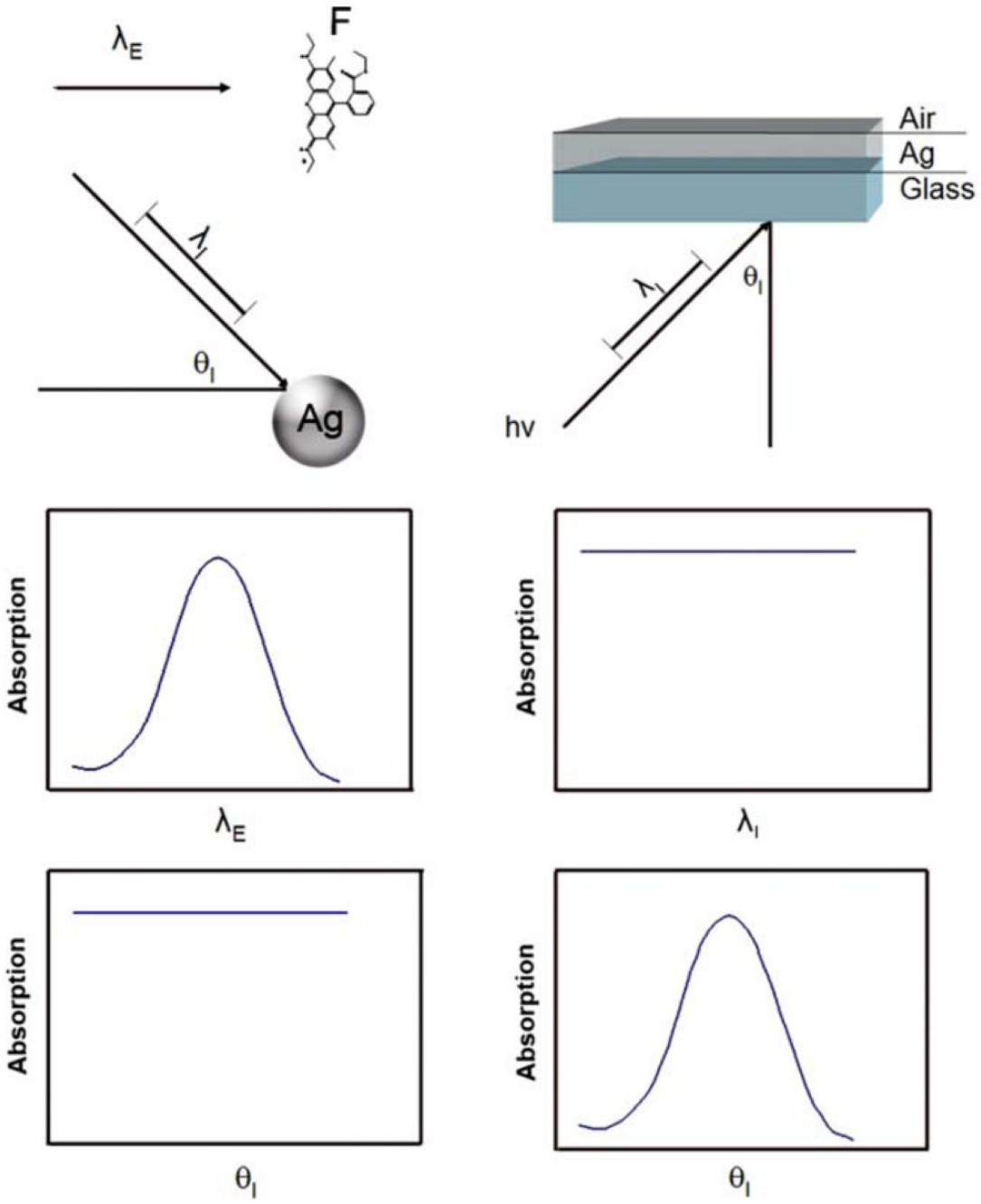

Fig. 39.
Comparison of the absorption properties of fluorophores, metal colloids and a thin metal film.

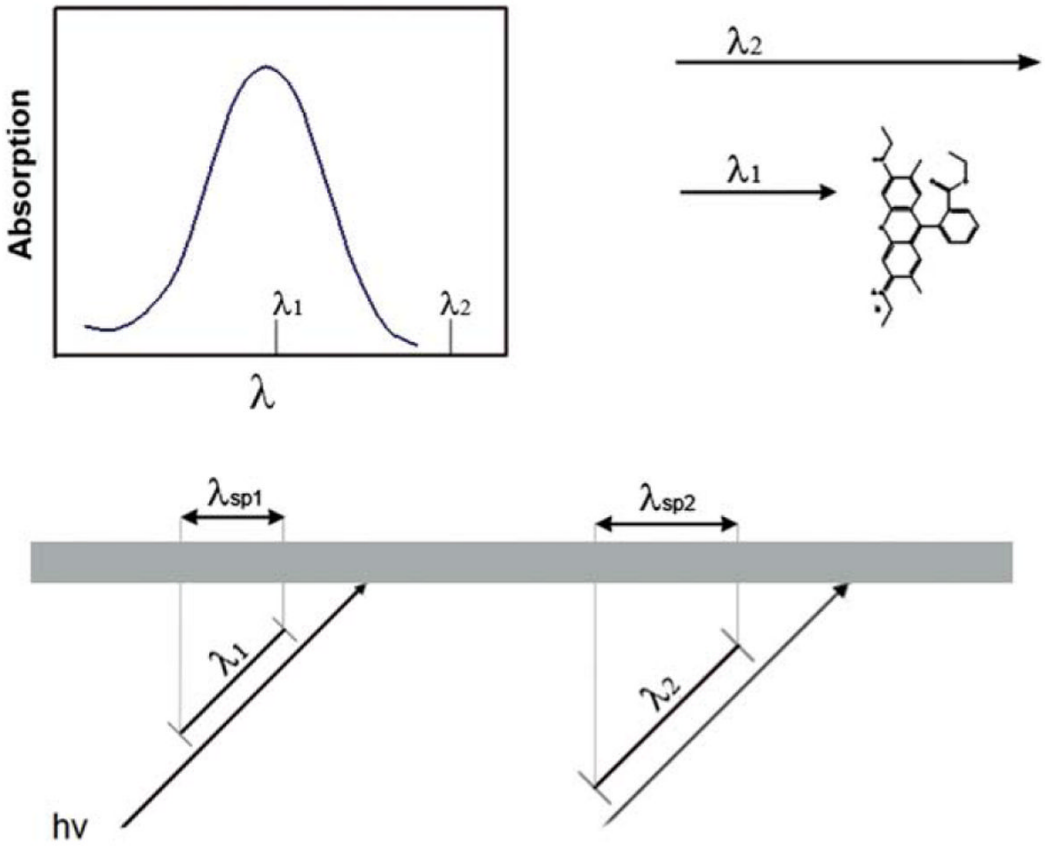

Fig. 40.
Effects of changing wavelengths on the absorption by fluorophores and metal films.

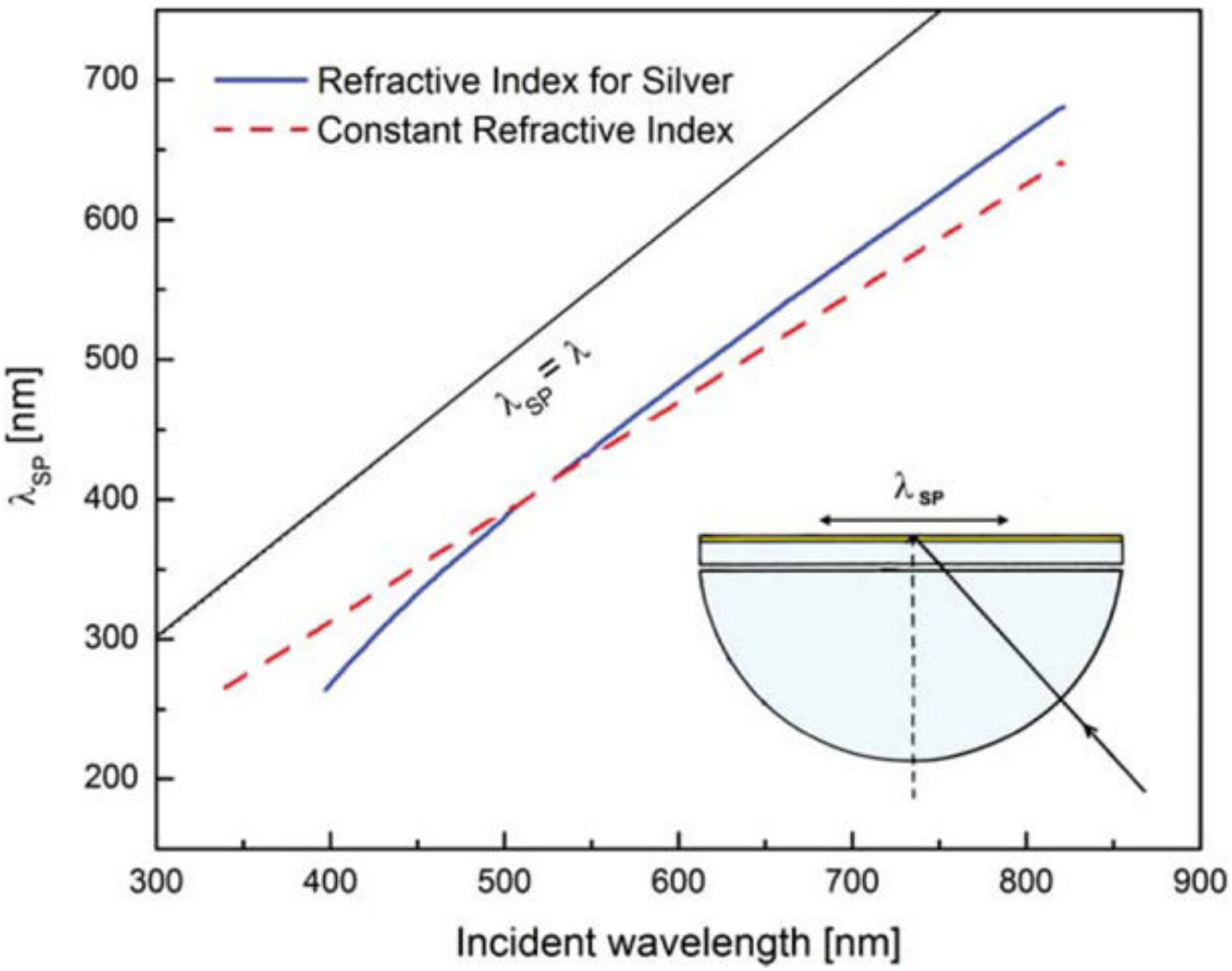

Fig. 41.

Dependence of the surface plasmon wavelength for the known optical constants of silver. Also shown are the wavelengths in a prism and in a vacuum. The dielectric constants of the sample and prism were $\varepsilon_s = 1.76$ and $\varepsilon_p = 2.95$. The dashed line is the light line in a vacuum.

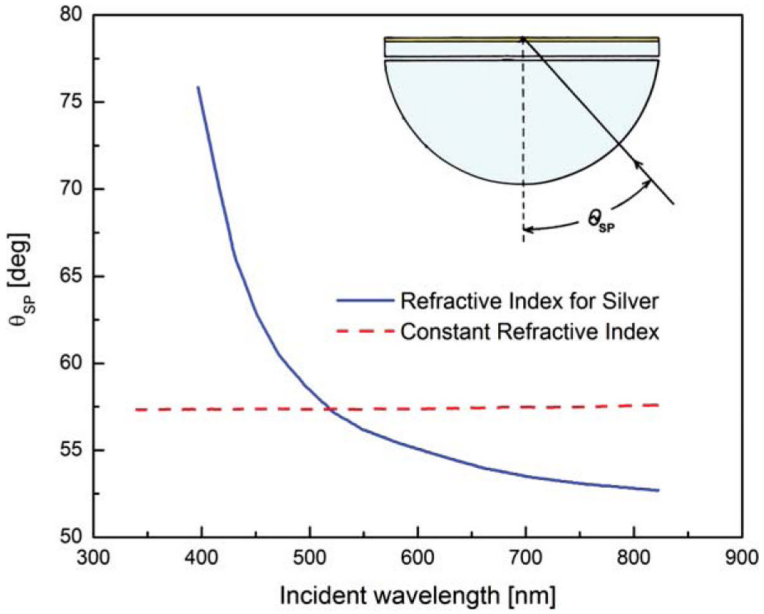

Fig. 42.

Dependence of the surface plasmon angle θ_{SP} on the incident wavelength for a real metal silver and for a material with a constant refractive index.

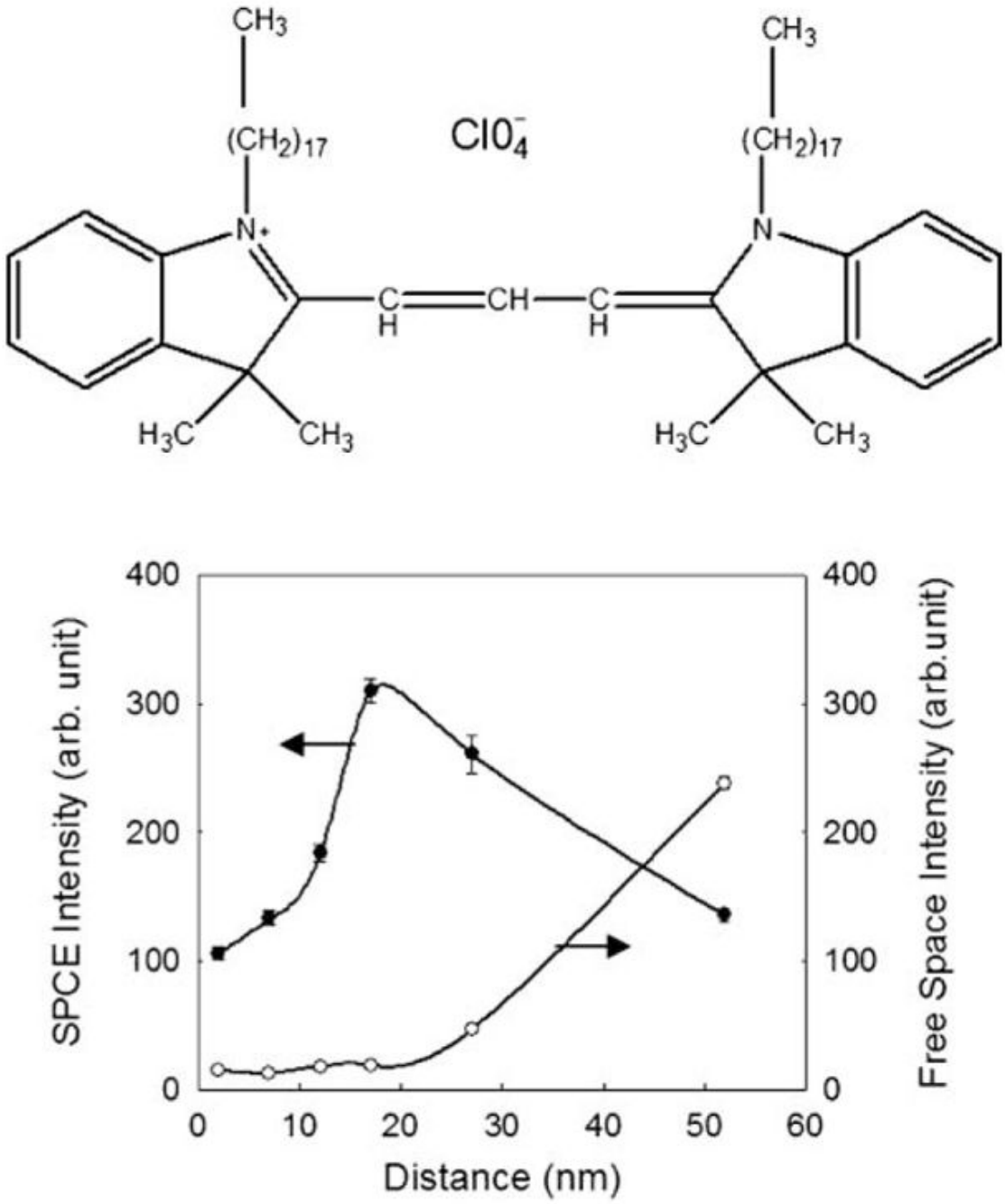

Fig. 43.

SPCE and free-space intensities of DiI at various distances from a silver film. (Reprinted with permission from ref. [137]. Copyright 2007, American Institute of Physics.)

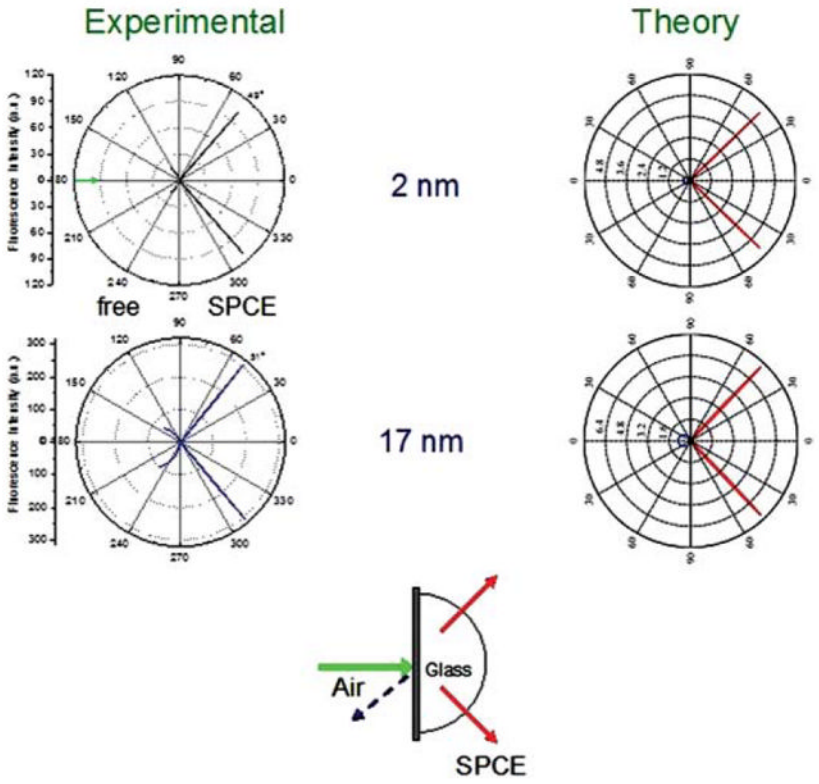

Fig. 44.
Angle-dependent SPCE intensities. (Reprinted with permission from ref. [137]. Copyright 2007, American Institute of Physics.)

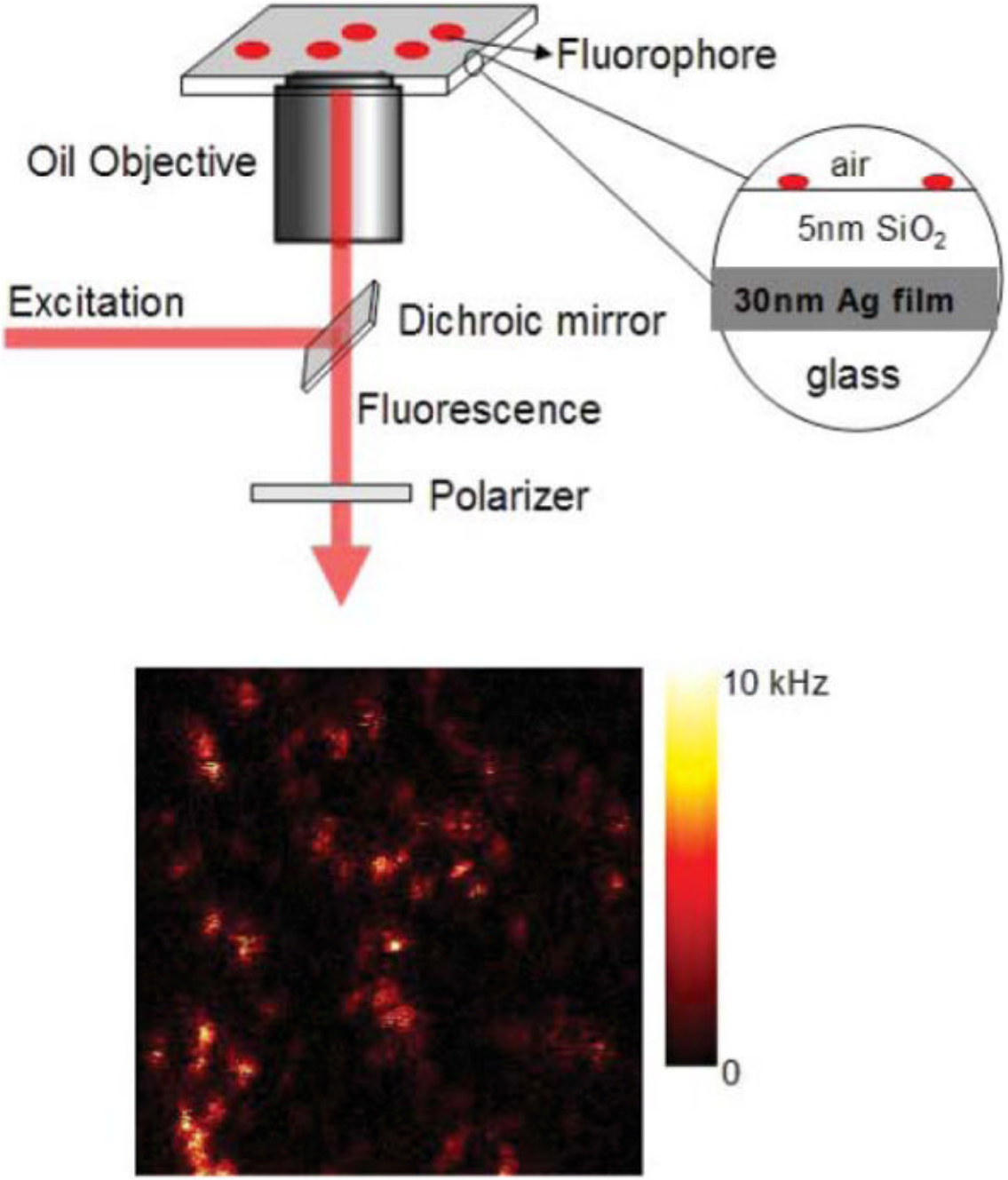

Fig. 45.
Single molecule imaging of Cy5 through a silver film.[139]

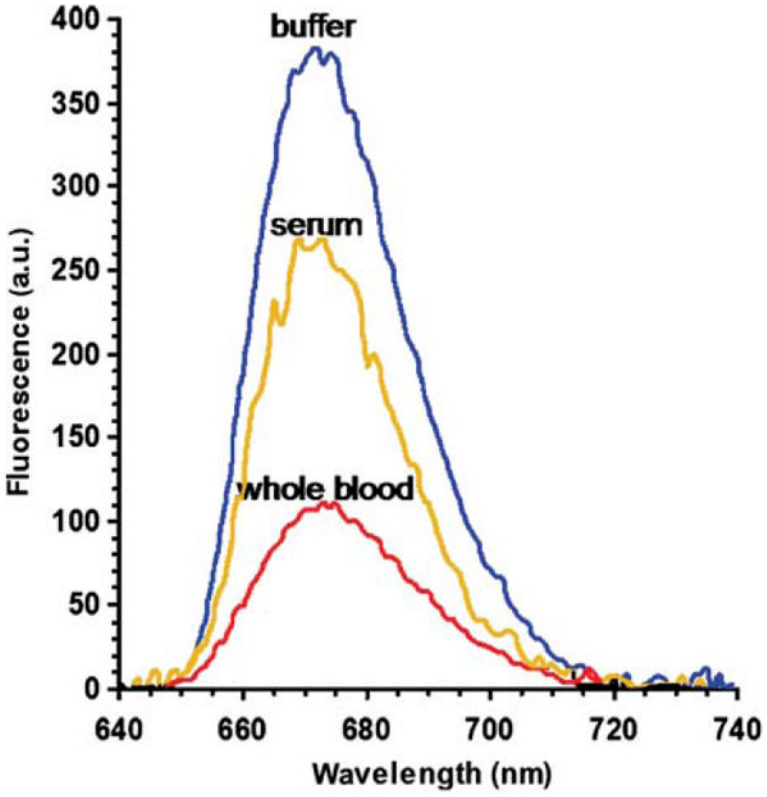

Fig. 46.

Fluorescence spectra (SPCE) of the Alexa Fluor 647® -labeled anti-rabbit antibodies bound to the rabbit IgG immobilized on a 50 nm silver mirror surface observed in buffer, human serum, and human whole blood (KR configuration), a.u. = arbitrary units. (Reprinted with permission from ref. [142]. Copyright 2005, Elsevier.)

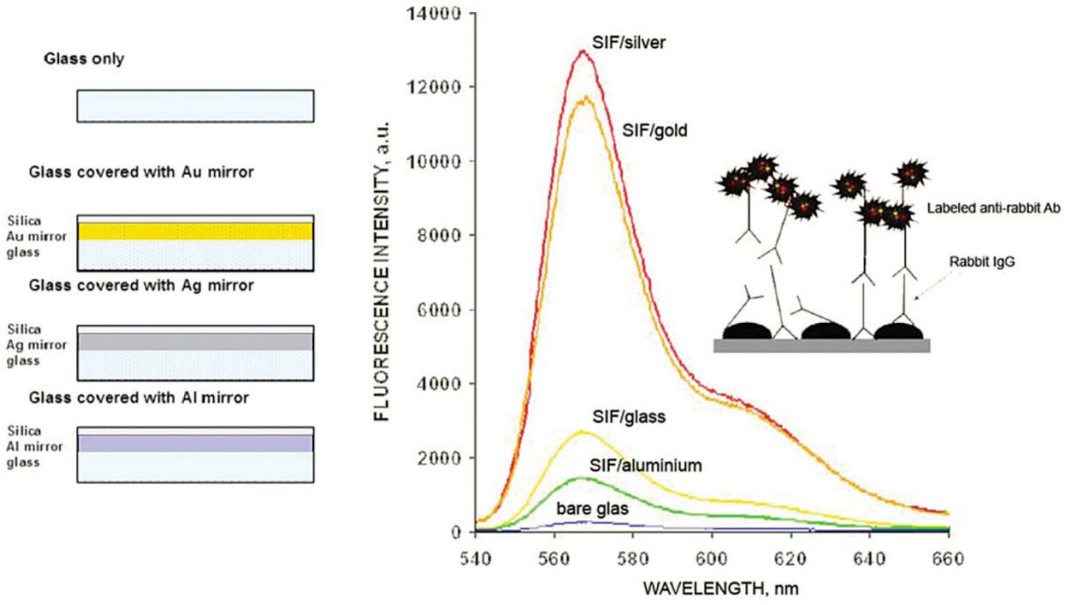

Fig. 47.

Left: schematic of substrates with silver particles above a smooth metal film. Each substrate has silver particles on the silica. Right: emission spectra of Alexa Fluor 555® -labeled IgG on the substrates. (Reprinted with permission from ref. [143]. Copyright 2007, Elsevier.)

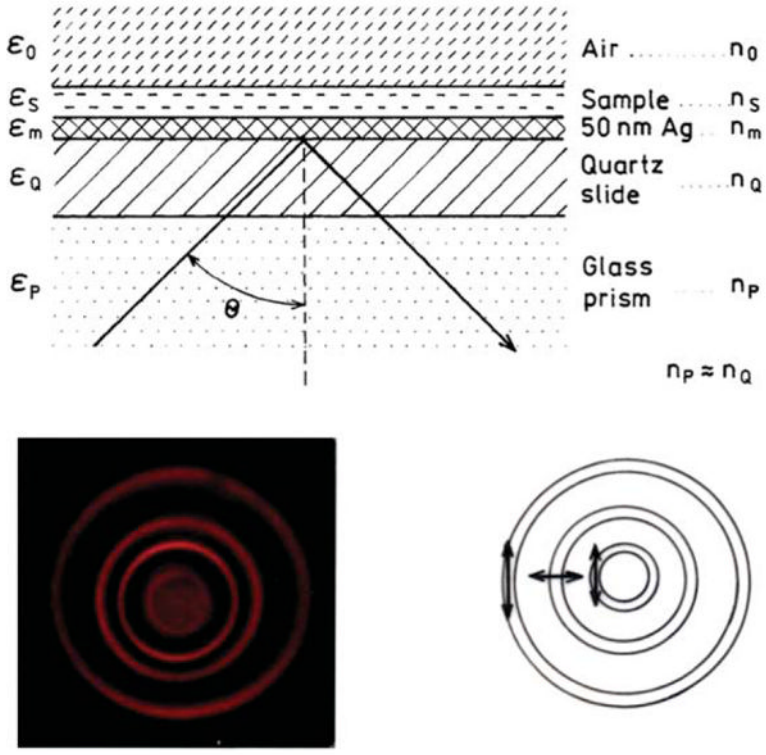

Fig. 48.
Waveguide SPCE. (Reprinted with permission from ref. [145]. Copyright 2004, American Chemical Society.)

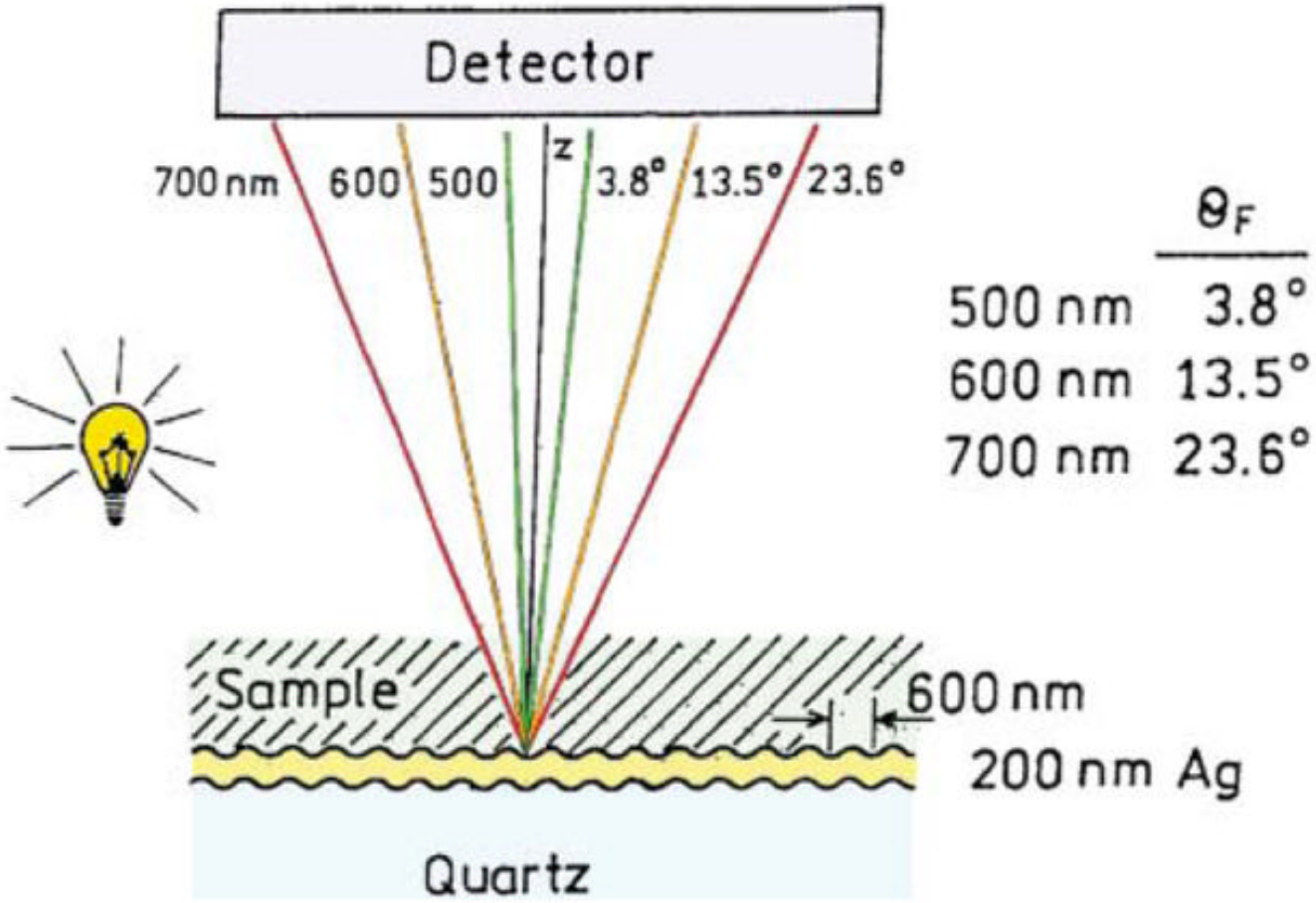

Fig. 49.
Wavelength separation using grating-coupled excitation and emission.

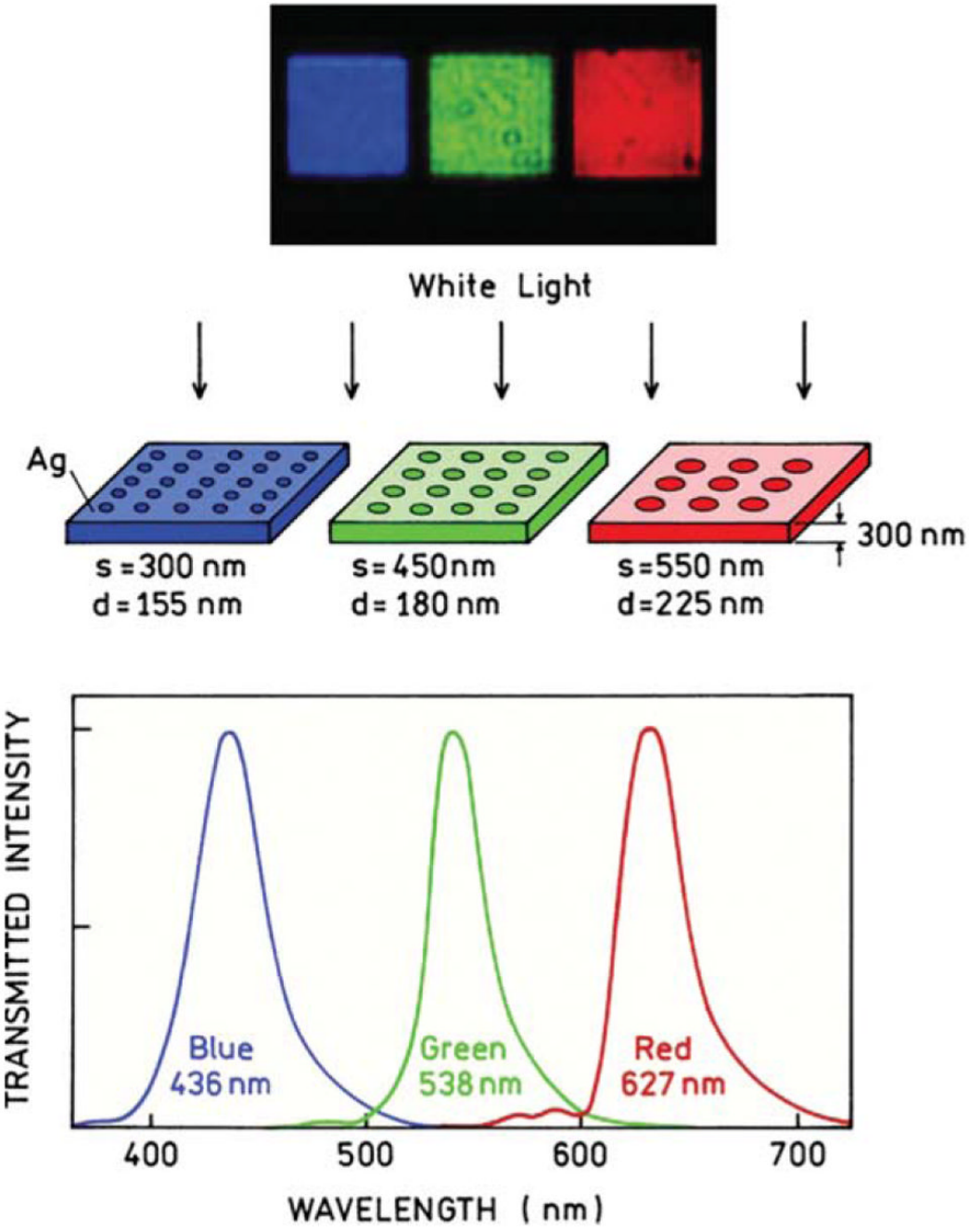

Fig. 50.

Plasmon transmission of light through otherwise opaque 300 nm-thick silver films containing an array of nano-holes. The top panel is a photograph of the films back-illuminated with white light. (Reprinted with permission from ref. [153]. Copyright 1998, Macmillan Publishers Ltd.)

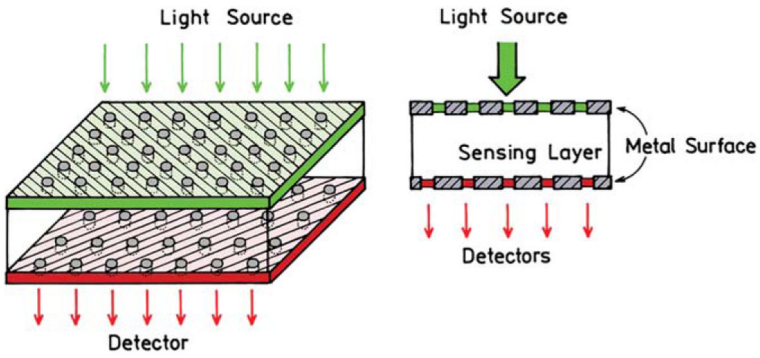

Fig. 51.
Possible configuration for a sensor based on nano-hole arrays.

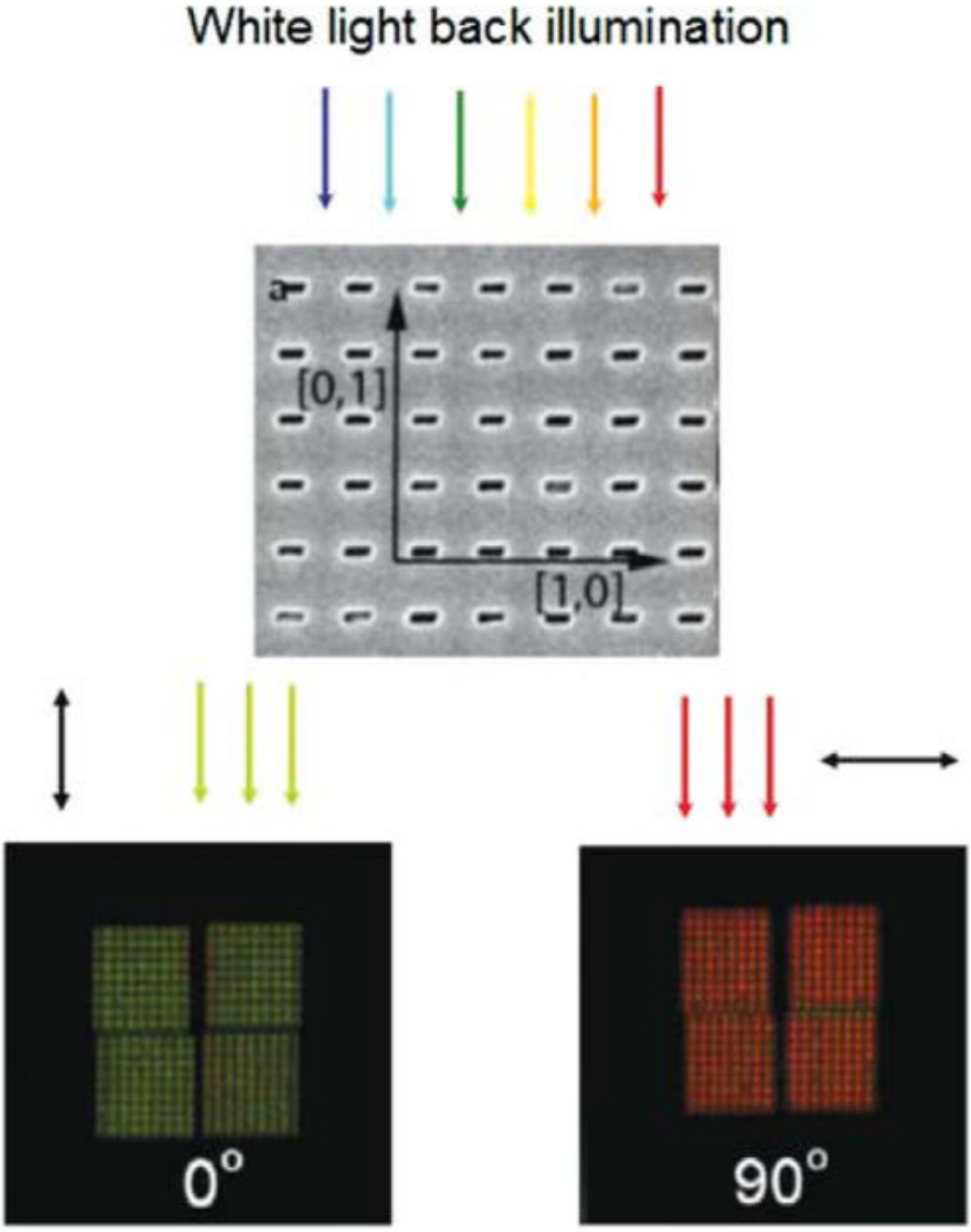

Fig. 52.
SEM image of a nano-hole array and real color photographs of the arrays through polarizers with white light back-illumination. (Reprinted with permission from ref. [159]. Copyright 2006, Optical Society of America.)

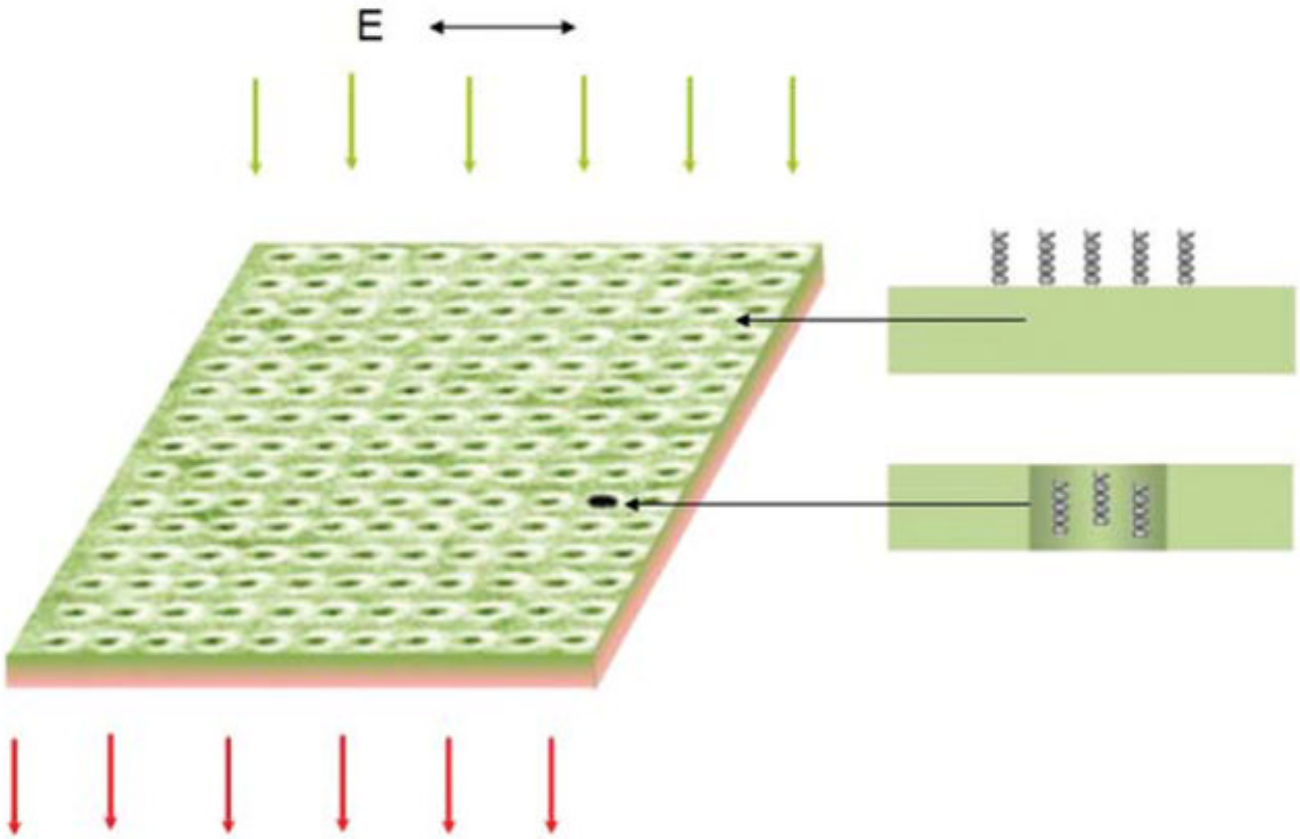

Fig. 53.
Schematic for a 200 nm thick fluorometer based on a nano-hole array.

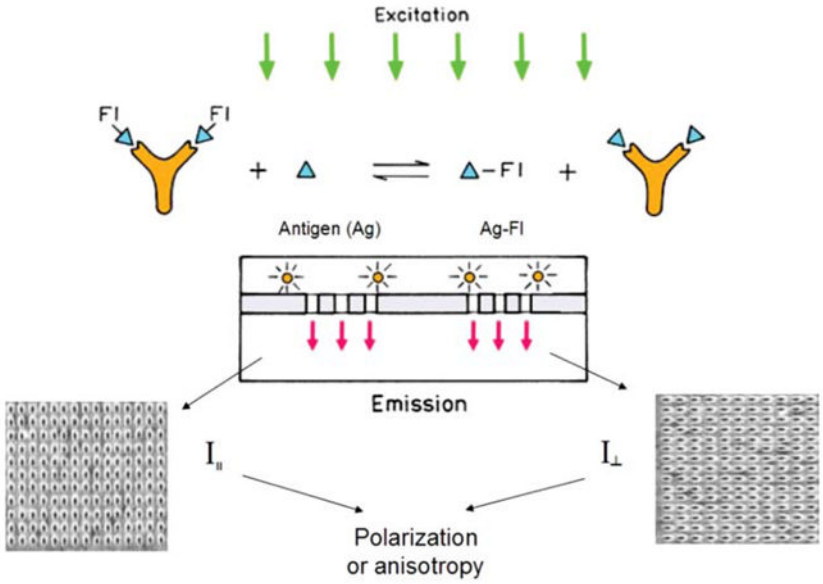

Fig. 54.
Schematic for thin-film fluorescence polarization assays.

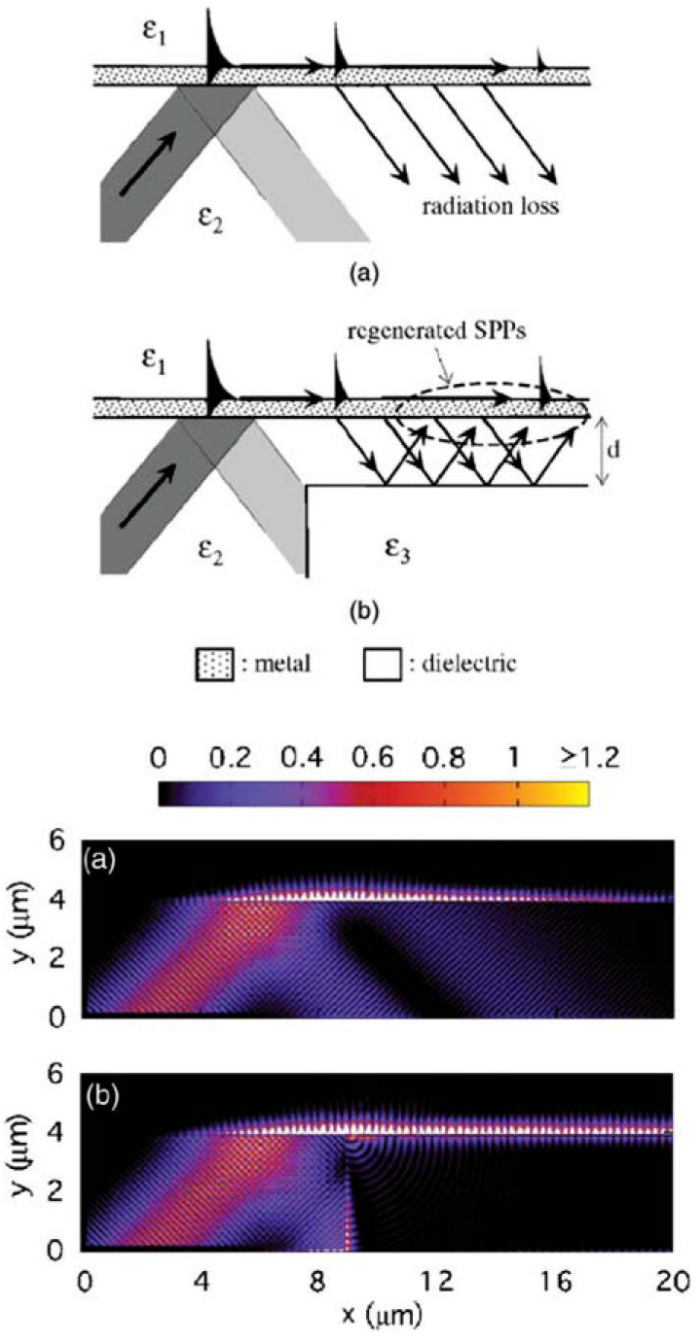

Fig. 55.
FDTD calculations of plasmon transport of a metal–air interface. (Reprinted with permission from ref. [164]. Copyright 2005, American Institute of Physics.)

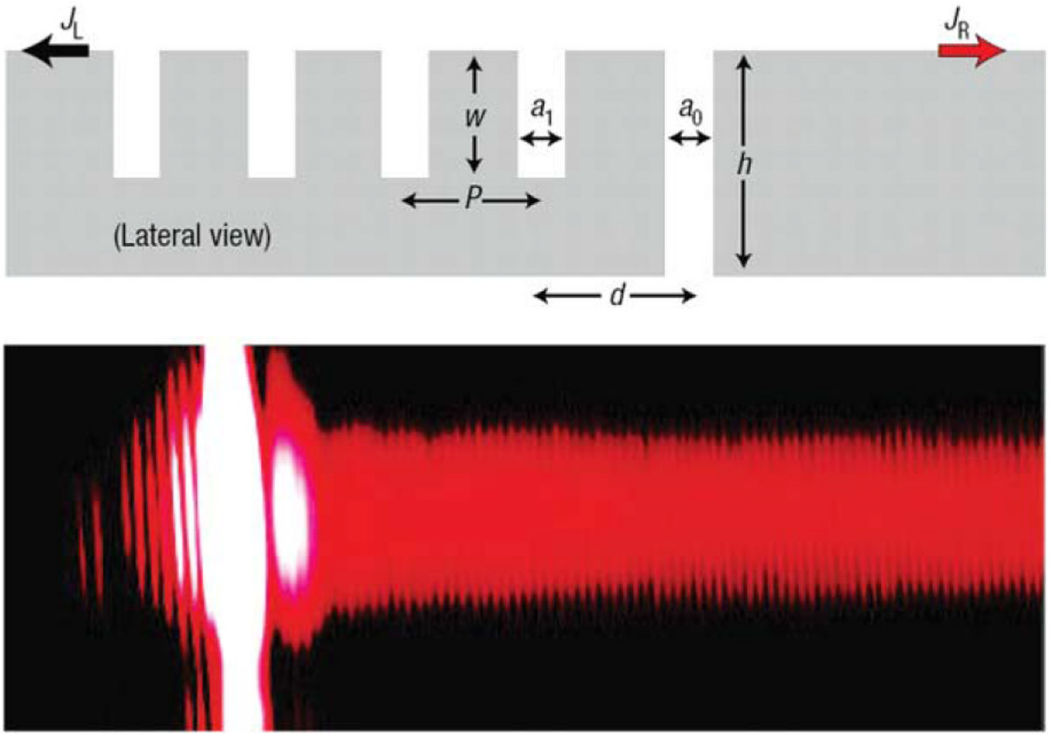

Fig. 56.
Metallic structure used for directional launching of plasmons (top) and near-field imaging of the plasmons (bottom). The wavelength is 1520 nm. (Reprinted with permission from ref. [165]. Copyright 2007, Macmillan Publishers Ltd.)

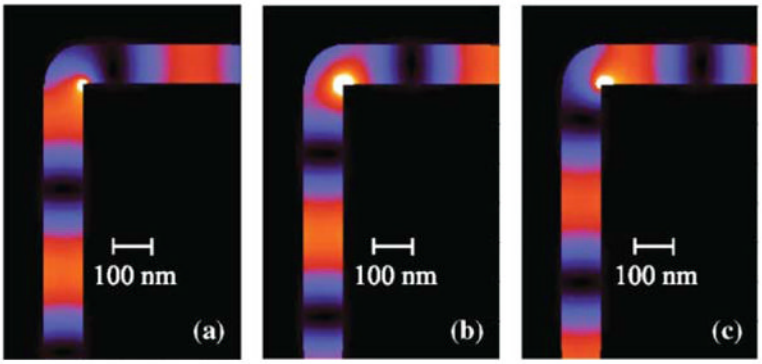

Fig. 57.

FDTD simulations of plasmon transport in a slit in a metal film. The panels show the fields at t, $t + 0.4 \times 10^{-15}$ s, and $t + 0.8 \times 10^{-15}$ s. (Reprinted with permission from ref. [166]. Copyright 2005, Optical Society of America.)

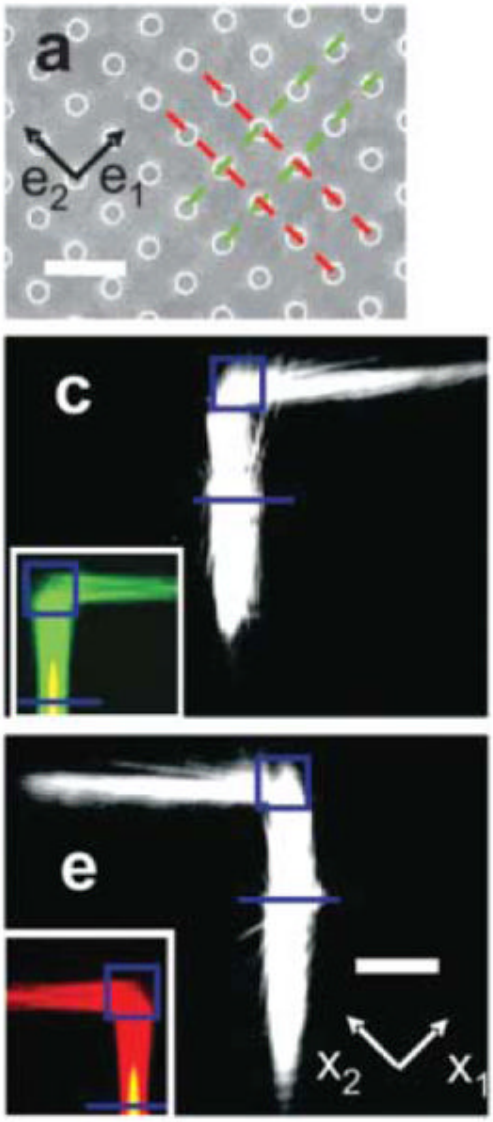

Fig. 58.

Surface plasmon demultiplexer. Top: image of structure. The middle and bottom panels show the optical energy for plasmons created with 750 and 800 nm illumination, respectively. The inserts are numerical simulations. (Reprinted with permission from ref. [169]. Copyright 2007, American Chemical Society.)

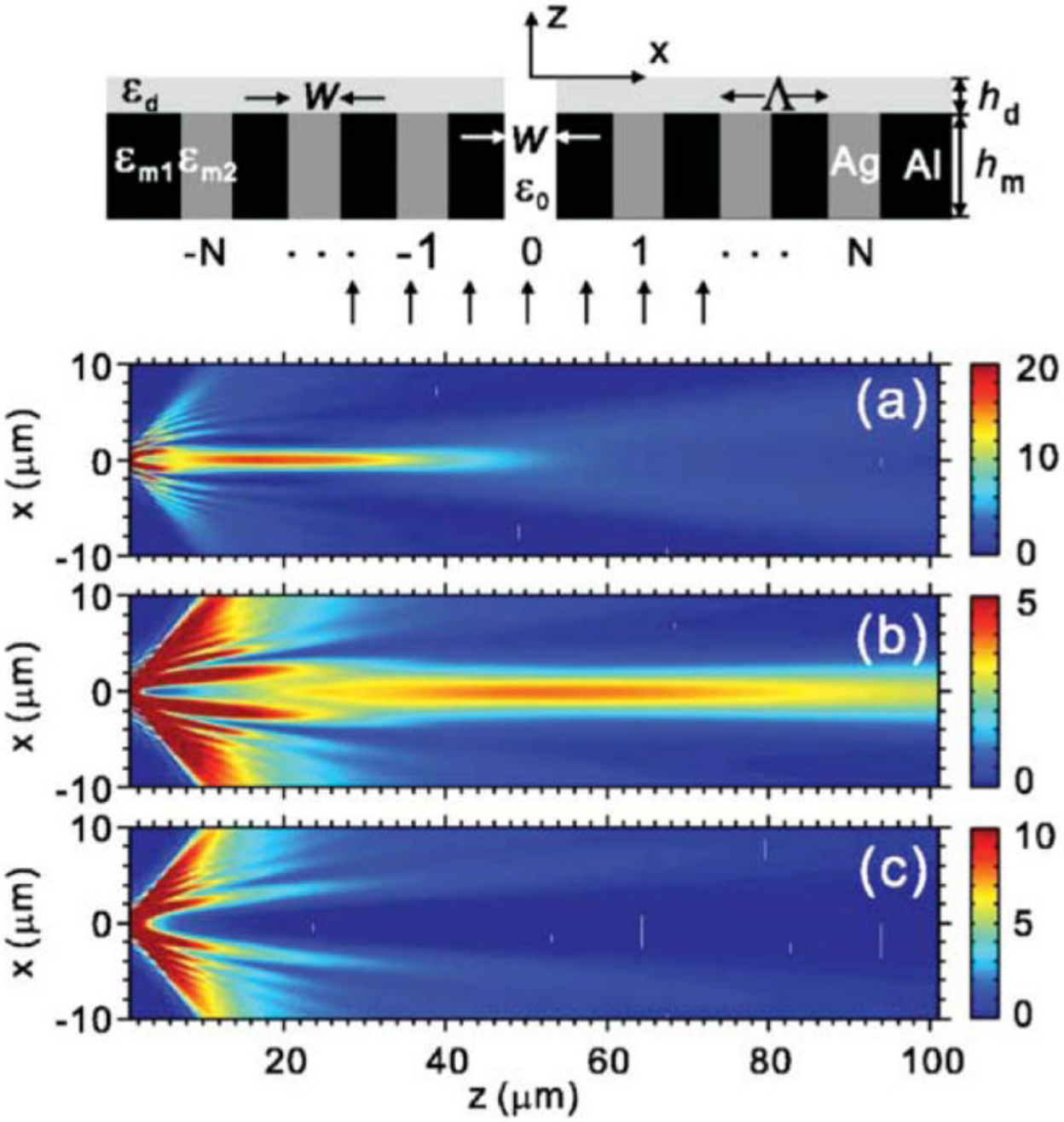

Fig. 59.

Calculations of light transmission through a nano-hole surrounded by concentric rings of Al and Ag. For these calculations the incident wavelength is 539 nm, h_m = 360 nm and Λ = 380 nm. The thickness of the dielectric over the metal is h_d = 80 (a), 100 (b) and 120 (c) nm. (Reprinted with permission from ref. [170]. Copyright 2006, American Institute of Physics.)

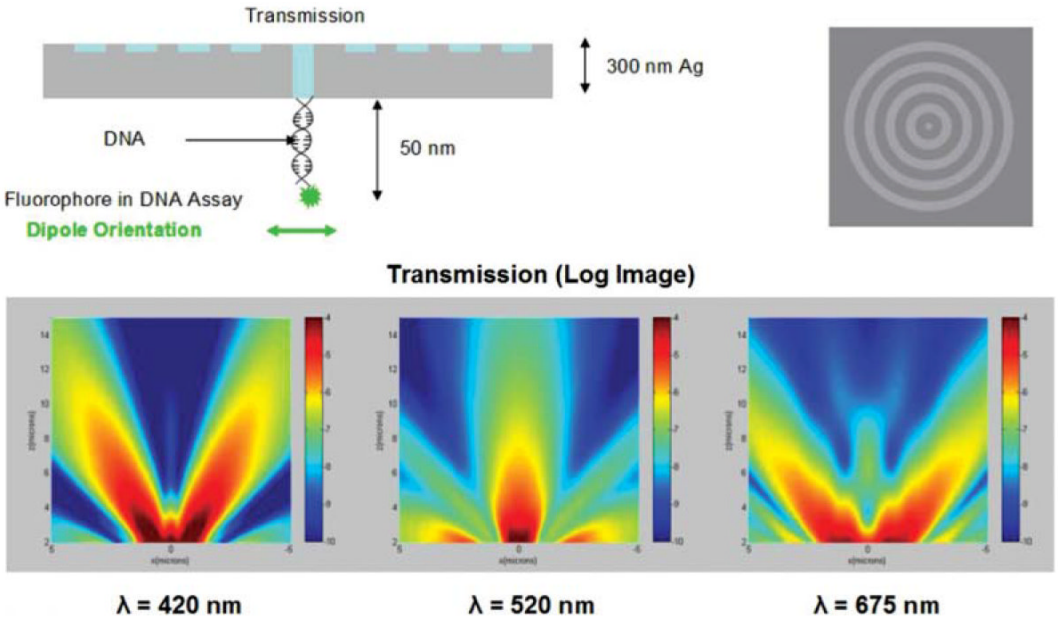

Fig. 60.

Top right: concentric nano-rings fabricated using FIB. Top left: schematic of a fluorophore on concentric nano-rings. Bottom: FDTD calculations of the plasmon emission induced by the fluorophores at the end of the detection antibody. The emissive patterns depend on wavelengths but not on the fluorophore–metal distance.[176]

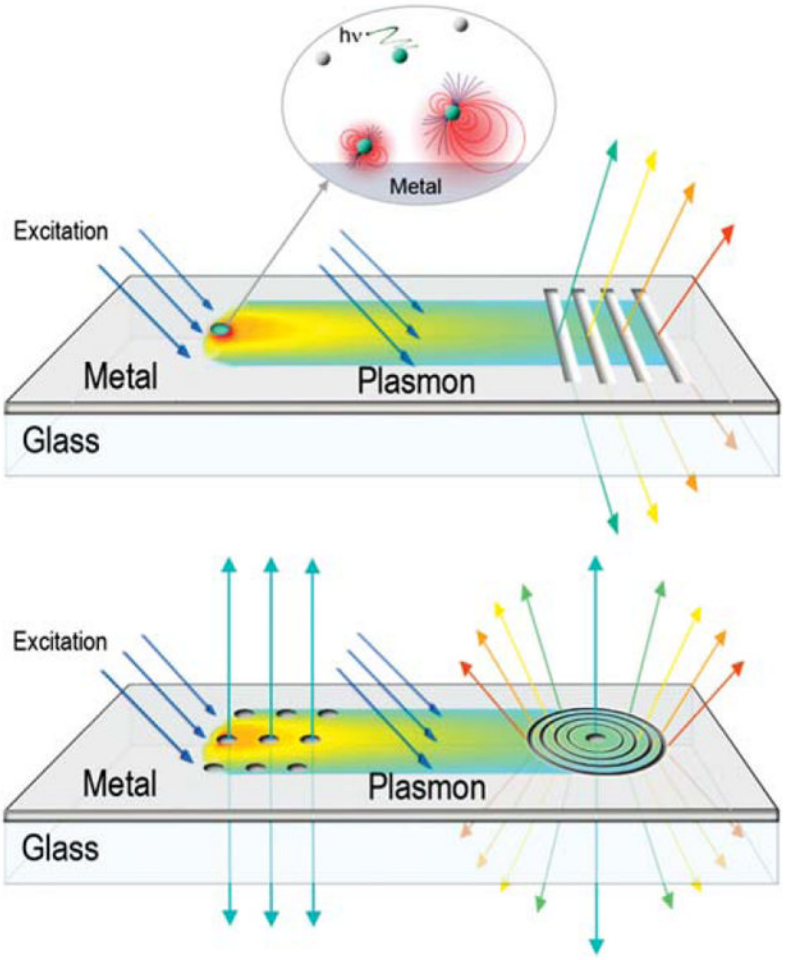

Fig. 61.

Top: potential clinical sensors based on directional plasmons and outcoupling with nanogrooves. Bottom: potential devices with wavelength-selective nano-holes or nano-rings for directionality.

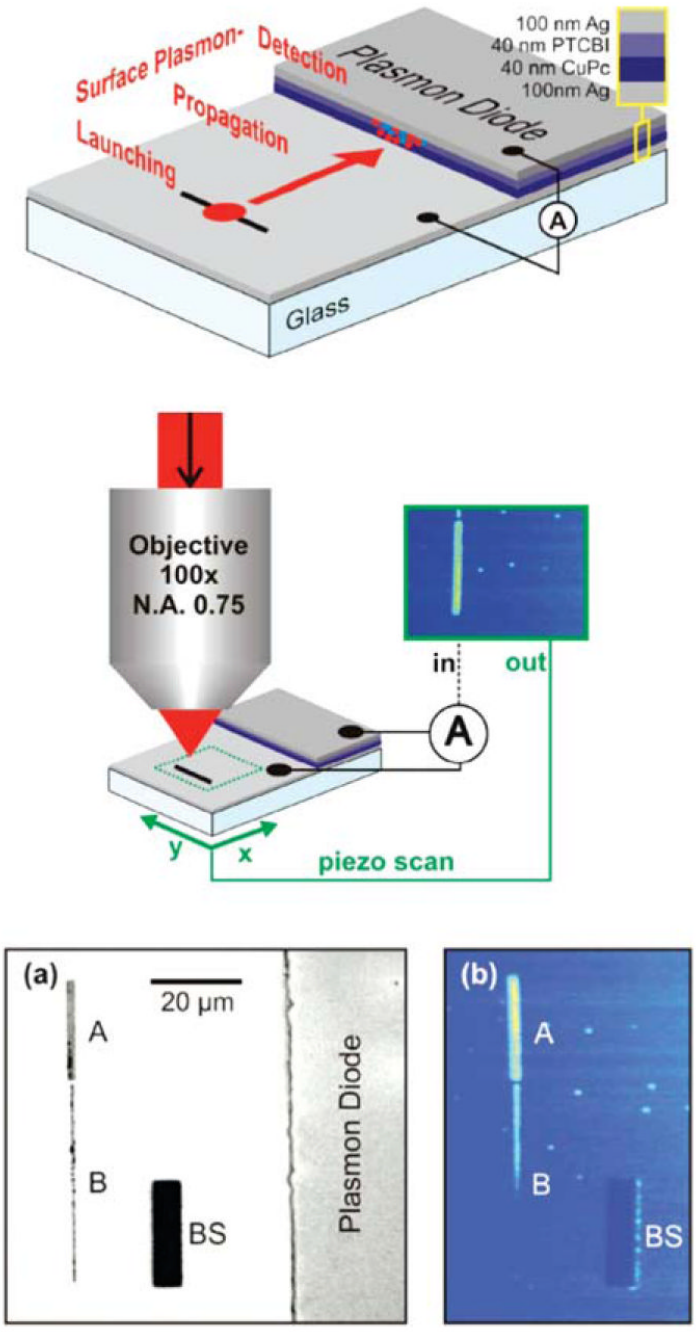

Fig. 62.

Schematic of a surface plasmon detector (top), illumination scheme (middle), optical image (lower left) and electrical current image (lower right). (Reprinted with permission from ref. [177]. Copyright 2006, American Institute of Physics.)

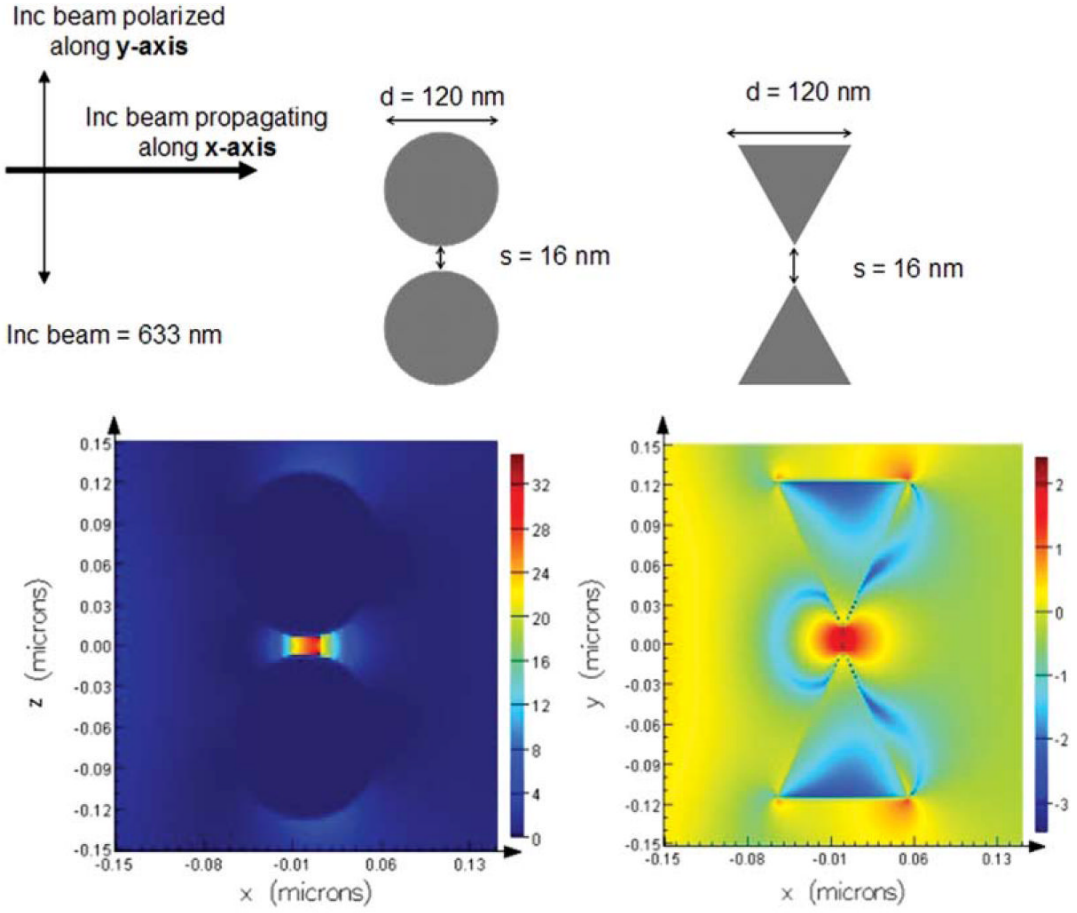

Fig. 63.

Schematic of silver particle dimers and FDTD calculations of the electric fields due to plane-wave illumination. Note the log scale on the right panel.[180]

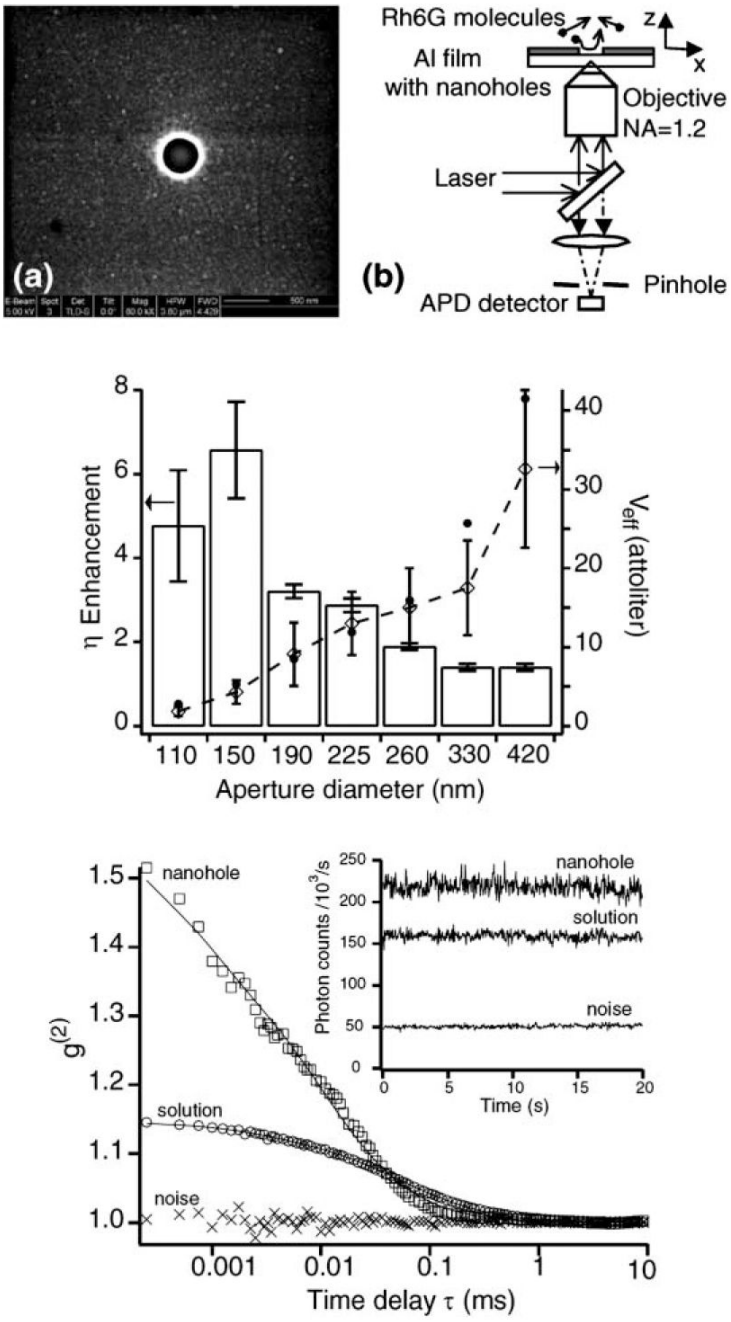

Fig. 64.

Fluorophores in nano-holes in 300 nm thick Al film. Top: image of nano-hole and schematic; middle: single molecule enhancement and effective volumes; bottom: FCS of 20 nM Rh6G in solution and 600 nm Rh6G in the nano-hole. (Reprinted with permission from ref. [185]. Copyright 2005, American Physical Society.)

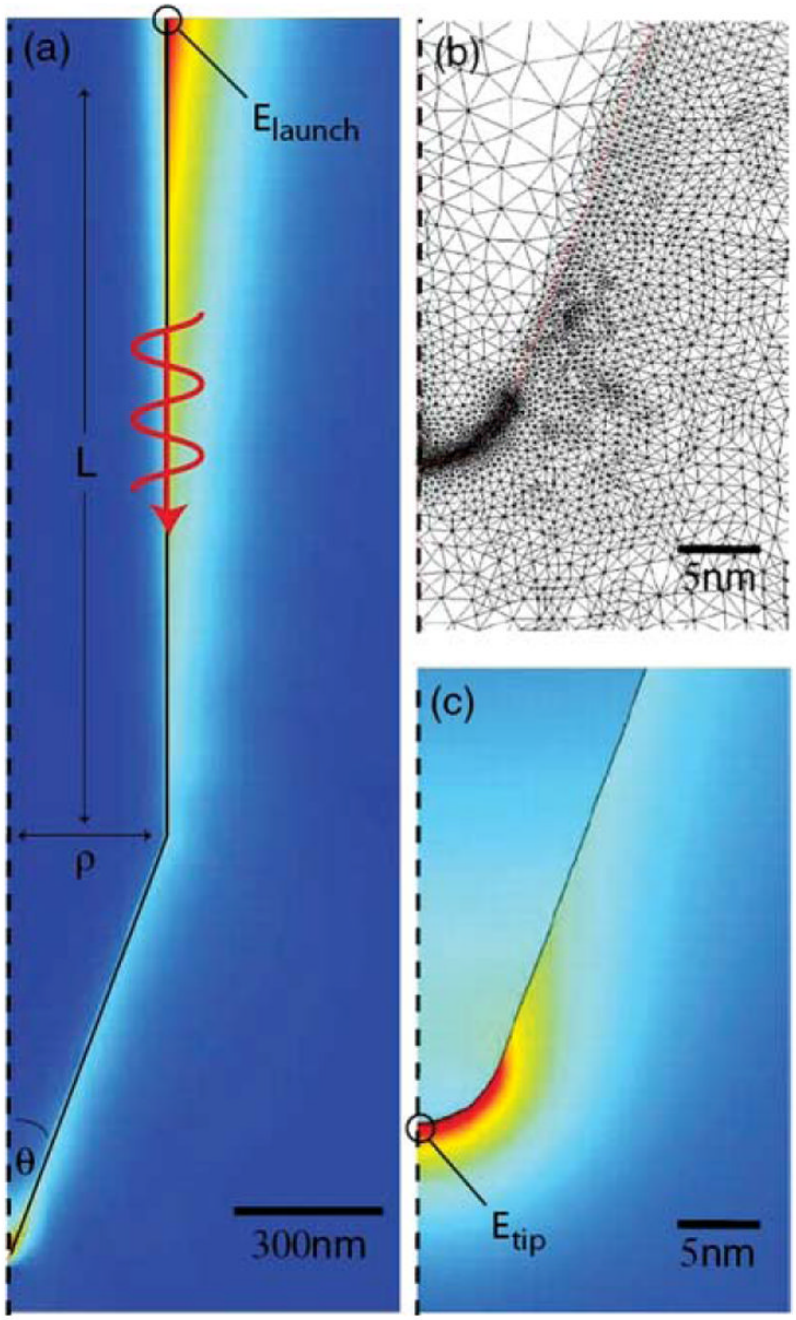

Fig. 65.
Calculation of plasmon migration in a tapered 300 nm diameter gold wave. The free-space wavelength is 532 nm. [Reprinted with kind permission from ref. [191] (Fig. 2). Copyright 2007, Springer Science + Business Media.]

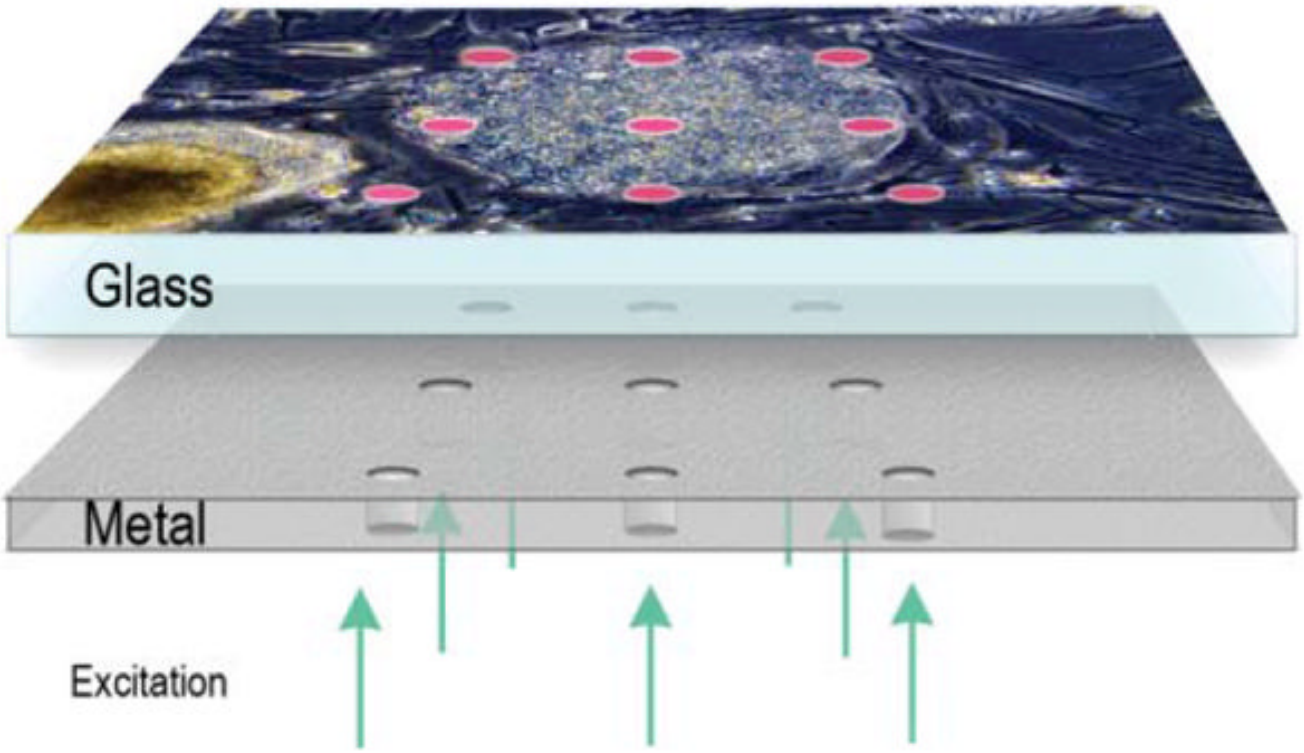

Fig. 66.
Schematic for a plasmon-based microscope with sub-wavelength resolution.

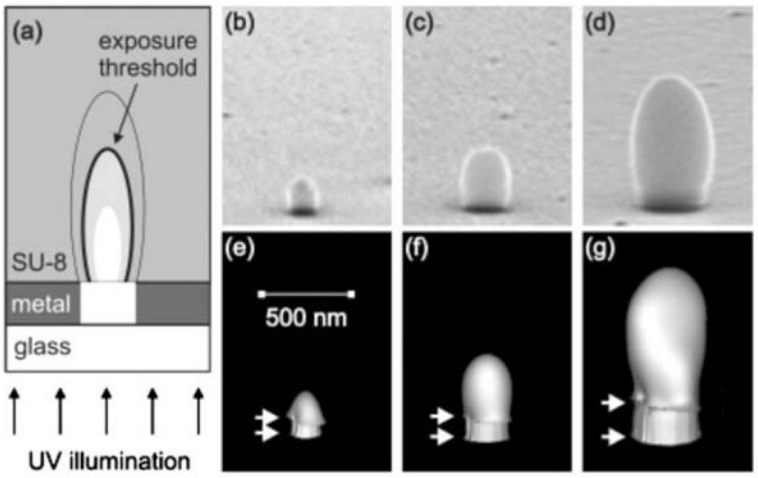

Fig. 67.

Photolithographic mapping of light intensity transmission through an aluminium film. Panels (b)–(d) show the pattern in the SV-8 photoresist for hole diameters of 110, 200 and 360 nm. Panels (e)–(g) show the intensities calculated by the FDTD method. (Reprinted with permission from ref. [198]. Copyright 2005, American Chemical Society.)

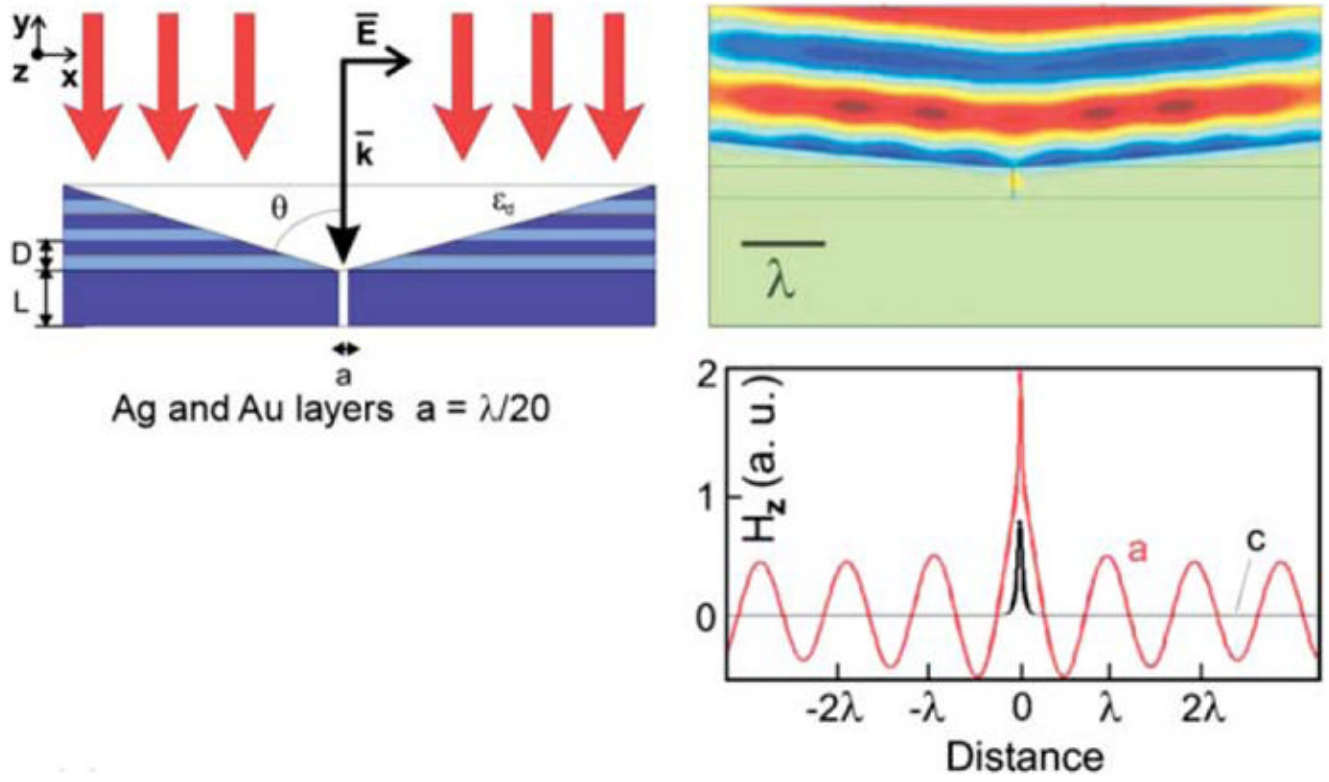

Fig. 68.

Sub-wavelength excitation volumes using nano-apertures in layered metal films. (Reprinted with permission from ref. [199]. Copyright 2006, Optical Society of America.)

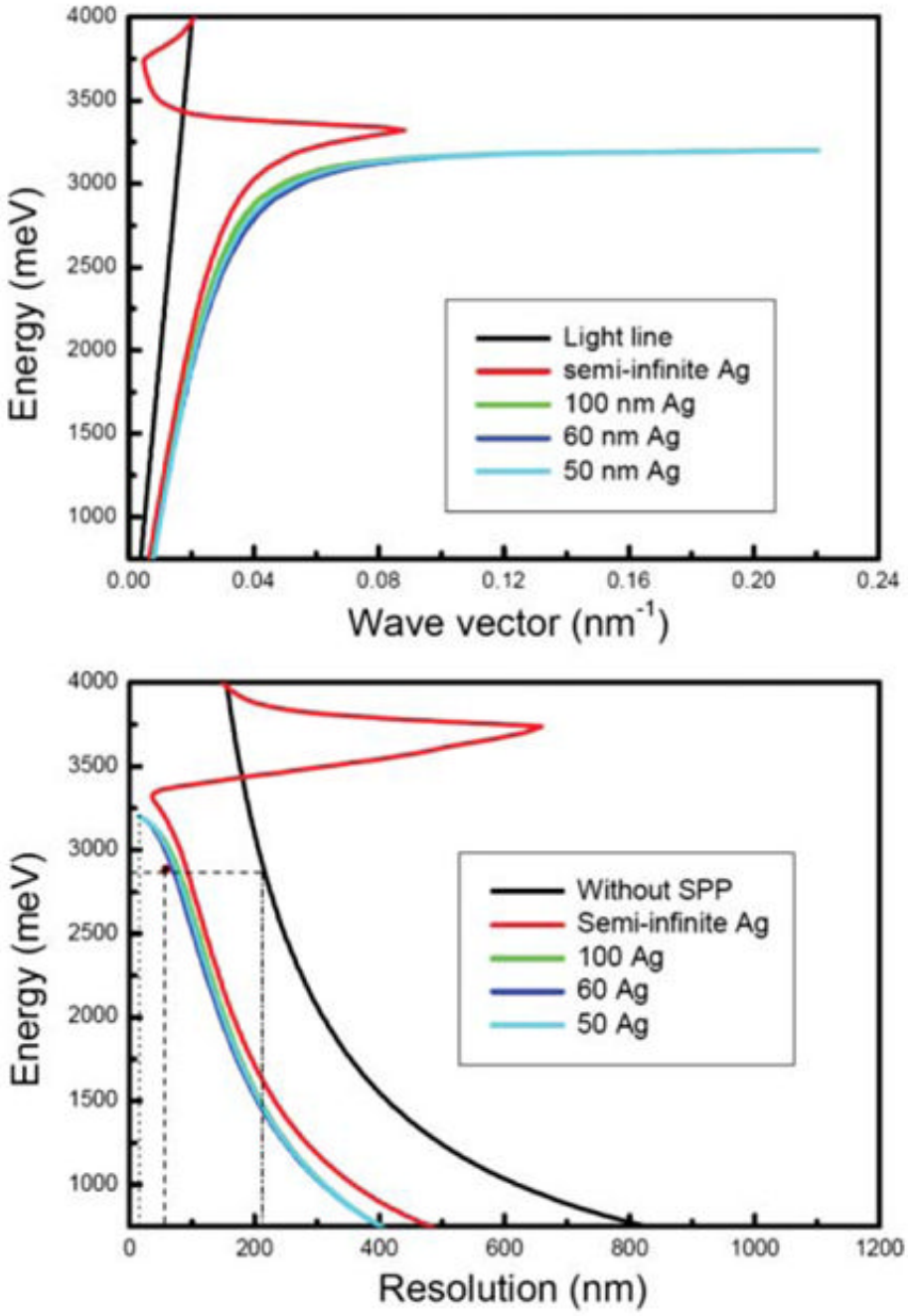

Fig. 69.

Dispersion (top) and spatial resolution (bottom) of thin silver films. (Reprinted with permission from ref. [200]. Copyright 2004, Optical Society of America.)

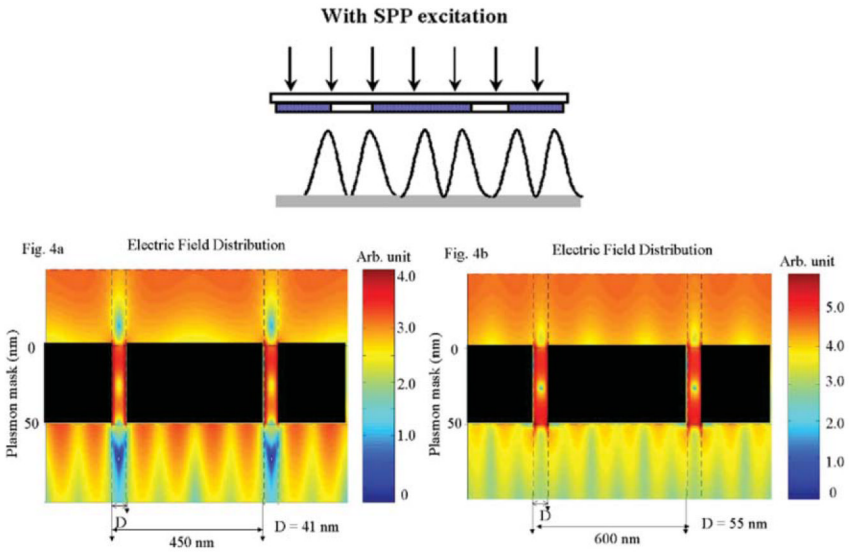

Fig. 70.

Electric fields due to interference between surface plasmons. (Reprinted with permission from ref. [200]. Copyright 2004, Optical Society of America.)

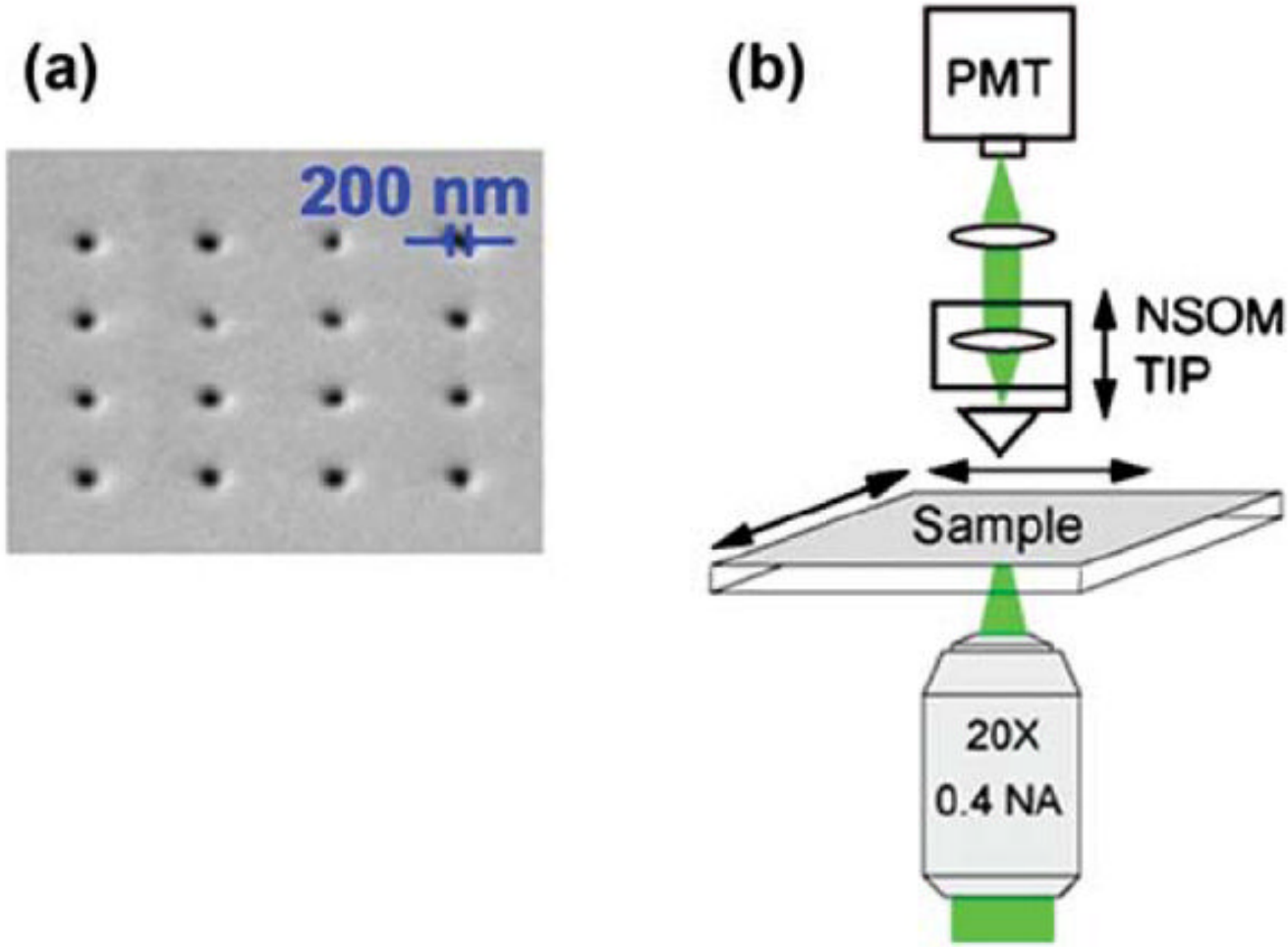

Fig. 71.
(a) SEM of a 4 × 4 nano-hole array in a 200 nm-thick silver film. (b) Schematic of the NSOM configuration used to measure the far-fields. (Reprinted with permission from ref. [205]. Copyright 2007, American Institute of Physics.)

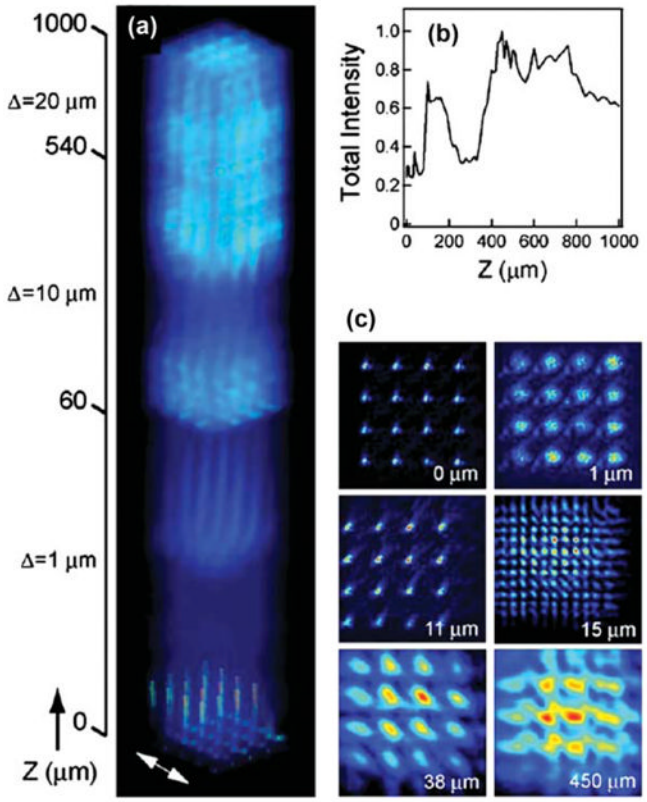

Fig. 72.

(a) Intensity of the light transmitted through the 4 × 4 nano-hole array. (b) Total intensity above the array. (c) *xy*-Plane images above the array. (Reprinted with permission from ref. [205]. Copyright 2007, American Institute of Physics.)